5-2018

Reactivity and Characterization of Intermetallic Alloy Catalysts for Alkane Dehydrogenation

Evan C. Wegener
Purdue University

REACTIVITY AND CHARACTERIZATION OF INTERMETALLIC ALLOY CATALYSTS FOR ALKANE DEHYDROGENATION

by

Evan C Wegener

A Dissertation

Submitted to the Faculty of Purdue University

In Partial Fulfillment of the Requirements for the degree of

Doctor of Philosophy

Davidson School of Chemical Engineering

West Lafayette, Indiana

May 2018

THE PURDUE UNIVERSITY GRADUATE SCHOOL
STATEMENT OF COMMITTEE APPROVAL

Dr. Jeffrey T. Miller, Chair
Davidson School of Chemical Engineering

Dr. Jeffrey Greeley
Davidson School of Chemical Engineering

Dr. Phillip C. Wankat
Davidson School of Chemical Engineering

Dr. Christopher Uyeda
Department of Chemistry

Approved by:

Dr. Sangtae Kim
Head of the Graduate Program

For my Family

ACKNOWLEDGMENTS

I would like to begin by thanking my advisor, Professor Jeffrey Miller, for his continued guidance and support throughout the process of completing my degree. I will be forever grateful for the opportunity he gave me to become one of his first students at Purdue. Jeff has always found a way to keep me focused and my research moving forward while also helping me plan for life after grad school. He has been a wonderful mentor and has my utmost respect as both a researcher and a person.

Next, I would like to acknowledge those I have worked closely with during my time at Purdue and contributed significantly to the work in my dissertation and to my development as a researcher. I have been fortunate to get to work with Zhenwei Wu from day one in Jeff's group. Over the last three years he has always been open for discussion and I could not imagine going through this processes without him. My many talks with Dr. Guanghui Zhang have immensely improved my knowledge of chemistry and catalysis. Brandon Bukowski has always brought an excitement to our collaboration and his calculations have greatly aided in understanding my experimental results. Thank you to Dr. James Gallagher and Dr. Jeremy Kropf who were always willing and patient teachers and from whom I was able to learn a great deal of what I know about synchrotron characterization techniques. I would also like to acknowledge the others who have played major roles in the works outline in this dissertation: Han-Ting Tseng, Dr. Viktor Cybulkis, Dali Yang, Professor Jeffrey Greeley, Professor Fabio Ribeiro, Dr. Yang Ren, Dr. James Harris, Dr. Rosa Diaz, and Dr. Bruce Ravel.

Lastly, I would like to acknowledge my friends and family who have supported me throughout this journey. To all the friends I have made here, the time we have spent together, whether in academic or social settings, has made my experience in West Lafayette extremely enjoyable. Thank you to my family, especially my parents, grandparents, and sister and brother-in-law, who have always been there for me. Finally, I would like to thank my wife, Olivia. Consistently she has been a calming influence in my life and without her none of this would have been possible.

TABLE OF CONTENTS

LIST OF TABLES

LIST OF FIGURES

ABSTRACT

Author: Wegener, Evan, C. PhD
Institution: Purdue University
Degree Received: May 2018
Title: Reactivity and Characterization of Intermetallic Alloy Catalysts for Alkane Dehydrogenation
Committee Chair: Jeffrey T. Miller

As the United States works towards energy independence shale gas has become an attractive domestic recourse for use as a feedstock to produce fuels. One potential approach to utilize shale gas is to first convert the C_2 and C_3 paraffinic components into olefins, valuable chemical building blocks, by catalytic dehydrogenation. The goal of this dissertation is to study how the geometric and electronic changes to a metal upon alloying influence its selectivity for light alkane dehydrogenation.

In the first three projects bimetallic catalysts comprising of either Pd or Pt and a post-transition metal known to promote olefin selectivity were investigated. In all the systems studied the bimetallic catalysts were found to be more selective for ethane dehydrogenation than the monometallic analogue. *In situ* characterizations revealed the formation of intermetallic compounds (IMC) which contained either small ensembles of or completely isolated active atoms in the bimetallic catalysts. It is believed that these geometric changes to the active metal are the dominant factor leading to improved dehydrogenation selectivities. From a study performed on Pd-In catalysts it was proposed that IMC structures similar to the active metal are preferentially formed. In a separate study, two distinct IMC structures were formed in Pt-In catalysts with different In:Pt atomic ratios and the two phases were found to have different turnover rates (TOR) and apparent activation energies. These results showed that the catalytic properties of metals could be altered by forming different IMC structures. Lastly, a study on Pt-Zn catalysts revealed changes in energy of the 5d states of Pt upon IMC formation. The observed energy change is believed to be responsible for increases in dehydrogenation TOR.

In the fourth project Pt-Fe bimetallic catalysts were investigated as an extrapolation of the findings of the first set of studies. Pt and Fe were found to form three IMC structures as the Fe:Pt atomic ratio was varied. All three structures contained Pt atoms with local geometries identical to the catalysts selective for ethane dehydrogenation. When tested for propane dehydrogenation the

IMC catalysts were found to be highly selective for propylene. Although Pt and Fe are both catalytic, the much higher activity of the former results in the latter behaving as an inert diluent. This results in the small ensembles of and isolated Pt atoms in the IMC structures being highly selective for dehydrogenation. Electronic structure measurements and calculations showed small changes in the average energies of the 5d states of Pt as the Fe content of the IMC changed. Associated with the valance energy shifts were changes in metal-adsorbate bond strengths which were believed to be the cause of increased dehydrogenation TOR. These results demonstrated that it is possible to change the electronic structure of metals by forming IMCs with different promoters or stoichiometries. While electronic effects play a secondary role in alkane dehydrogenation, this insight could provide useful for other catalytic chemistries.

CHAPTER 1. INTRODUCTION

1.1 Motivation

The goal of national energy independence was first proposed by Richard Nixon in 1973 [1] and has been emphasized by nearly every president since. [2] While ultimately this goal will be achieved by utilizing renewable fuels, improvements in current technologies are necessary to make using these energy resources practical. [3] The net energy deficit is largely due to the reliance on imported petroleum for the production of liquid transportation fuels. Finding a domestic energy source to be used as a bridge between petroleum and renewables would help to shorten the time in which the United States can achieve energy independence.

The United States has massive deposits of natural gas trapped in shale formations. [4] The marriage of hydraulic fracturing and horizontal drilling technologies beginning in the early 2000s has made the recovery of gas from these deep-underground shale formations economical. [5] This has led to enormous increases in natural gas production, which are projected to continue for the coming decades [6], and has made shale gas an attractive feedstock for the synthesis of products traditionally derived from petroleum. The major component of shale gas is methane; however, some reserves may contain up to 20 % ethane and propane. This growth in supply of natural gas liquids has resulted in some petrochemical manufactures shifting their feedstocks from petroleum to cheaper shale gas condensates. [7] In addition to fine-chemicals these abundant C_2 and C_3 hydrocarbons offer an opportunity as a feedstock to produce liquid transportation fuels. Typical catalytic gas-to-liquids technologies such as Fischer-Tropsch and the ExxonMobil methanol-to-gasoline process have focused on methane conversion. However, these processes suffer from poor economic returns and are likely not viable options for utilizing shale gas for liquid fuels production. [8] Currently there are no economical technologies to transform ethane and propane into liquid products for use as transportation fuels. Therefore, the development of novel catalytic materials and processes for the conversion of natural gas liquids to fuels offers an opportunity to fully realize the potential of shale gas as an energy source and push the United States towards energy independence.

1.2 Light Alkane Dehydrogenation

Light alkanes can be directly converted to alkenes via catalytic dehydrogenation. The olefin products can then be converted to fuel range molecules. Due to the endothermic nature of dehydrogenation reactions high temperatures are required for equilibrium to favor the formation of olefins. However, at the elevated temperatures required to obtain high alkane conversions the undesired side reactions of hydrogenolysis and coke also occur resulting in yield losses. [9] Therefore, catalyst selectivity towards olefins is paramount when designing a light alkane dehydrogenation process. The on-purpose production of propylene is currently done industrially via the UOP Oleflex process which utilizes a Pt-Sn bimetallic catalyst. Although all group VIII metals are active for dehydrogenation and hydrogenolysis, Pt is used industrially because it is the only metal that shows higher selectivity for the former reaction over the latter. Sn is added to further increase olefin selectivity and catalyst life. [10] While the addition of Sn to Pt catalysts has been widely studied due to its industrial relevance other post-transition elements (Zn [11], Ga [12], and In [13]) have been reported to have similar promotional effects. The increased performance has been attributed to the formation of alloys, but the exact mechanism of the promotional effect is still debated.

Both geometric and electronic effects have been proposed to be the cause of the improved performance of the bimetallic catalysts. The geometric argument is based on the idea of structure sensitive and insensitive reactions proposed by Buodart. [14] Alkane dehydrogenation is a structure insensitive reaction where the active site is a single metal atom. Conversely, alkane hydrogenolysis is a structure sensitive reaction where the active site is an ensemble of several metal atoms. Alloy formation breaks up ensembles of active Pt atoms limiting C-C bond cleavage while C-H bond activation is unaffected. [15-17] Although geometric changes have been proposed to lead to higher selectivity, rarely has the exact structure of the catalytic surface been identified. Increased selectivities have also been attributed to the enhanced desorption of alkene products due to electronic changes to Pt upon alloying. It has been proposed that electron donation from the promoter to Pt due to differences in electronegativity results in weaker metal-olefin bonds. Hydrogenolysis is believed to proceed through deeply dehydrogenated surface species. It is thought that faster olefin desorption reduces the number of deeply dehydrogenated surface species resulting in higher selectivity. [18-21] Determining whether geometric or electronic changes are

the dominant factor responsible for higher olefin selectivity is an important step towards the ability to rationally design improved catalytic materials for light alkane dehydrogenation.

A bimetallic Pd-Zn catalyst has recently been reported to be highly selective for light alkane dehydrogenation. When tested for propane dehydrogenation the bimetallic catalyst was nearly 100% selective for propylene, drastically different from monometallic Pd which produced almost exclusively methane before deactivating. It was determined that the addition of Zn to the Pd catalyst resulted in the formation of a 1:1 Pd-Zn intermetallic compound (IMC) with a AuCu structure. In the IMC structure each metal atom sits in a fixed lattice position, as opposed to a solid solution where the components are randomly distributed, which results in uniform local geometries. In the AuCu structure formed the catalytic Pd atoms are surrounded by inactive Zn. It was proposed that this isolation of active atoms (i.e. a geometric effect) was responsible for the observed increase in selectivity for propane dehydrogenation. [22, 23]

1.3 Dissertation Overview

The purpose of this work is to study whether the formation of intermetallic compounds with isolated active sites can be used as general method to achieve high olefin selectivity during alkane dehydrogenation. Although it is hypothesized that geometric effects dominate selectivity changes, alloying also alters the electronic properties of metals. A secondary goal of this work is to study the nature of these electronic changes and the role they play in alkane dehydrogenation. The approach taken was to study bimetallic catalysts consisting of either Pt or Pd and a known post-transition metal promoter and determine whether IMC structures with isolated active sites are formed. The findings from these studies were then used to select a non-traditional promoter to extrapolate the hypothesis of active site geometry being responsible for high alkane dehydrogenation selectivity.

Chapter 2 is a study on a series of Pd-In bimetallic catalysts selective for ethane dehydrogenation. The study has been published as “Pd-In intermetallic alloy nanoparticles: highly selective ethane dehydrogenation catalysts,” in Catalytic Science and Technology, 2016, 6, 6965-6976. The study found that the addition of In to Pd catalysts isolated the active atoms through the formation of a 1:1 IMC phase with a CsCl structure. Although numerous IMC phases are present in the bulk phase diagram and a range of In:Pd atomic ratios was studied, only the 1:1 phase with a highly symmetric CsCl structure was formed. It was proposed that the formation of the IMC

phase is a kinetically controlled process and structures that require minimal atomic rearrangement are preferentially formed.

A study on Pt-In catalysts is discussed in Chapter 3 and has been published as "Structure and reactivity of Pt-In intermetallic alloy nanoparticles: highly selective catalysts for ethane dehydrogenation," in Catalysis Today, 2018, 299, 146-153. It was found that Pt and In formed two different IMC phases: Pt_3In and $PtIn_2$, having Cu_3Au and CaF_2 type structures, respectively. Both phases were highly selective for ethane dehydrogenation. While the Pt atoms in $PtIn_2$ are isolated there are still adjacent active atoms in the Pt_3In structure which suggests total site isolation is not required to improve selectivity. In addition to the increases in ethylene selectivity, the formation of the IMC structures also resulted in higher turnover rates, indicative of electronic changes to Pt. The turnover rates were also found to be dependent upon the phase formed. From these results it was proposed that it may be possible to tune the electronic properties of catalysts by forming IMC structures with different stoichiometries.

Chapter 4 is a study on Pt-Zn bimetallic catalysts which combined electronic structure measurements and calculations to gain insight into the effect of alloying on the valance states of catalytic metals. The work has been published as "Zinc Promotion of Platinum for Catalytic Light Alkane Dehydrogenation: Insights into Geometric and Electronic Effects," ACS Catalysis, 2017, 7, 4173-4181.It was shown that Pt and Zn form a 1:1 IMC phase with isolated active atoms which results in high selectivity for ethane dehydrogenation and increased turnover rates. Electronic structure measurements revealed that alloy formation shifted the average energy of the unfilled and filled 5d states of Pt upwards and downwards, respectively. Electronic structure calculations were found to agree with the experimental observations. It was proposed that the changes in the average energies of the valance states of Pt are the dominant electronic effect of alloying and that the increased turnover rates result from these shifts.

A study on Pt-Fe bimetallic catalysts selective for propane dehydrogenation is discussed in Chapter 5. The work is currently being finalized for publication. Pt and Fe were found to form three IMC phases: Pt_3Fe (Cu_3Au), PtFe (CuAu), and $PtFe_3$ (Cu_3Au). Although Pt and Fe are both catalytic for dehydrogenation and hydrogenolysis all three IMC phases were highly selective for propylene. This was attributed to the intrinsic activity of Fe being much lower than Pt. On the Pt-Fe IMC surfaces Fe acts as an inert diluent resulting in the small ensembles and isolated Pt atoms present in the structures being highly selective for dehydrogenation. Electronic structure

measurements, which were corroborated by theoretical calculations, revealed continual increases and decreases in the average energies of the unfilled and filled valance states of Pt as the IMC phase become more Fe rich. The directionalities of the shifts are the same as those observed in the PtZn IMC structure; however, the shifts are smaller in magnitude. Changes in the binding strength of carbon monoxide to Pt in the different IMC phases were found to correlate with the observed changes in average energies of the 5d state. It is believed that these changes in bond energy could lead to differences in surface coverages during reaction and result in increased turnover rates. From the findings of this work it is hypothesized that it could be possible to selectivity tune the catalytic properties of a metal by forming intermetallic compounds using different promoters or by changing the phase with a single promoter.

Chapter 6 summarizes the major conclusions of the four studies presented in this dissertation. This includes the implications from the finding of the four studies on the design of new improved materials for alkane dehydrogenation as well as a potential route for continued research on intermetallic compound catalysts.

1.4 References

1. R. Nixon, “Address to the Nation About Policies To Deal With the Energy Shortages," November 7, 1973. Online by Gerhard Peters and John T. Woolley, The American Presidency Project. http://www.presidency.ucsb.edu/ws/?pid=4034
2. C. Homans, “The Best-Laid Plans,” January 3, 2012. foreignpolicy.com. http://foreignpolicy.com/2012/01/03/the-best-laid-plans/
3. Department of Energy “Quadrennial Technology Review: An Assessment of Energy Technologies and Research Opportunities,” September 2015
4. Energy Information Administration, “U.S. Crude Oil and Natural Gas Proved Reserves, Year-end 2016,” February 13, 2018
5. Energy Information Administration, “Hydraulically fractured horizontal wells account for most new oil and natural gas wells,” January 30, 2018
6. Energy Information Administration, “Annual Energy Outlook 2018 with projections to 2050,” February 6, 2018
7. J. J. Siirola, AIChe Journal, 2014, 60, 810-819
8. Energy Information Administration, “Gas-to-liquids plants face challenges in the U.S. market,” February 19, 2014
9. K. J. Caspary, H. Gehrke, M. Heinritz-Adrian, M. Schwefer, “Dehydrogenation of Alkanes,” Handbook of Heterogeneous Catalysis, Ed. G. Ertl. John Wiley & Sons Incorporated, 2008. 3206-3229
10. J. J. Sattler, J. Ruiz-Martinez, E. Santillan-Jimenez, B. M. Weckhuysen, Chemical Reviews, 2014, 114, 10613-10653
11. J. Silvestre-Albero, M. A. Sanchez-Castillo, R. He, A. Sepulveda-Escribano, F Rodriguez-Reinoso, J.A. Dumesic, Catalysis Letters, 74, 2001, 17-25
12. G. Siddiqi, P. Sun, V. Galvita, A. T. Bell, Journal of Catalysis, 2010, 274, 200-206
13. P. Sun, G. Siddiqi, W. C. Vining, M. Chi, A. T. Bell, Journal of Catalysis, 2011, 282, 165-174
14. M. Boudart, Journal of Molecular Catalysis, 1985, 30, 27-38
15. R. D. Cortright, J. A. Dumesic, Journal of Catalysis, 1994, 148, 771-778
16. R. D. Cortright, J. M. Hill, J. A. Dumesic, Catalysis Today, 2000, 55, 213-223
17. V. Galvita, G. Siddiqi, P. Sun and A. T. Bell, Journal of Catalysis, 2010, 271, 209-219

18. M. Armbrüster, R. Schlögl and Y. Grin, Science and Technology of Advanced Materials, 2014, 15, 1-17
19. N. Iwasa and N. Takezawa, Topics in Catalysis, 2003, 22, 215-224
20. T. Takanashi, M. Tamura, Y. Nakagawa and K. Tomishige, RSC Advances, 2014, 4, 28664-28672
21. C. Li, Y. Chen, S. Zhang, S. Xu, J. Zhou, F. Wang, M. Wei, D. G. Evans and X. Duan, Chemistry of Materials, 2013, 25, 3888-3896
22. D. J. Childers, N. M. Schweitzer, S. M. K. Shahari, R. M. Rioux, J. T. Miller and R. J. Meyer, Journal of Catalysis, 2014, 318, 75-84
23. J. R. Gallagher, D. J. Childers, H. Zhao, R. E. Winans, R. J. Meyer and J. T. Miller, Physical Chemistry Chemical Physics, 2015, 17, 28144-28153

CHAPTER 2. PD-IN INTERMETALLIC ALLOY NANOPARTICLES: HIGHLY SELECTIVE ETHANE DEHYDROGENATION CATALYSTS

Wu, Z.; Wegener, E.C.; Tseng, H.; Gallagher, J.R.; Harris, J.W.; Diaz, R.E.; Ren, Y.; Ribeiro, F.H.; Miller, J.T.; "Pd-In intermetallic alloy nanoparticles: highly selective ethane dehydrogenation catalysts," Catal. Sci. Technol. 2016, 6, 6965. Reproduced by permission of The Royal Society of Chemistry, copyright 2016. DOI: 10.1039/c6cy00491a

2.1 Abstract

Silica supported Pd and Pd-In catalysts with different In: Pd atomic ratios and similar particle size (~2 nm) were tested for ethane dehydrogenation at 600 °C. For a monometallic Pd catalyst, at 15 % conversion, the dehydrogenation selectivity and initial turnover rate (TOR, per surface Pd site) were 53 % and 0.03 s^{-1}, respectively. Addition of In to Pd increased the dehydrogenation selectivity to near 100 % and the initial TOR to 0.26 s^{-1}. Carbon monoxide IR, *in situ* synchrotron XAS and XRD analysis showed that for Pd-In catalysts with increasing In loading, different bimetallic structures were formed: at low In loading a fraction of the nanoparticle surface was transformed into PdIn intermetallic compound (IMC, also known as intermetallic alloy) with a cubic CsCl structure; at higher In loading, a Pd-core/PdIn-shell structure was formed and at high In loading the nanoparticles were pure PdIn IMC. While a Pd metal surface binds CO predominantly in a bridge fashion, the PdIn IMC predominantly binds CO linearly. Formation of the PdIn IMC structure on the catalyst surface geometrically isolates the Pd catalytic sites by non-catalytic, metallic In neighbors, which is suggested to be responsible for the high olefin selectivity. Concomitant electronic effects due to Pd-In bond formation likely leads to the increase in TOR. Though multiple IMC structures with different atomic ratios are possible for the Pd-In binary system, only a cubic PdIn IMC with CsCl structure was observed, implying a kinetically controlled solid state IMC formation mechanism.

2.2 Introduction

The past decades have witnessed a steady growth in the demand of light olefin, one of the most important chemical building blocks. Conventional light olefin production methods include

steam cracking and fluidized catalytic cracking (FCC). The recent shale gas boom and corresponding decrease in light alkane prices make on-purpose olefin production via catalytic light alkane dehydrogenation (LAD) economically competitive. [1] Today, several new LAD installations are being built or planned. [2]

Selectivity control is critical for catalytic light alkane dehydrogenation. [3] Under typical reaction condition, noble metal catalysts produce methane in high yield and concomitant production of coke leads to rapid deactivation. Pt is the only noble metal used for LAD catalysts due to its intrinsic selectivity favoring C-H bond activation over C-C bond activation. [2] Commercially supported bimetallic Pt-Sn catalysts are used, in which the promoter Sn reduces side reactions and coke formation. [2-5] It is believed that Sn modifies the electronic structure of Pt by transferring electrons to its valence band. Dissociative adsorption of alkanes is suppressed and olefin desorption is enhanced, leading to less hydrogenolysis and coking. [4, 6-9] A geometric effect for Sn promotion has also been proposed wherein Sn reduces the Pt ensemble size by alloying with Pt or covering Pt sites with low coordination. [3, 10] However, the exact structure of the modified surface sites has seldom been investigated in very small nanoparticles characteristic of commercial catalysts.

Recently, a selective propane dehydrogenation catalyst comprised of a Pd containing intermetallic compound (IMC) was reported. [11, 12] Monometallic Pd was poorly selective (< 10 %) to propylene; however, when Zn was added, the dehydrogenation selectivity increased to greater than 98 %. The pronounced selectivity change was attributed to formation of a β_1-PdZn IMC (tetragonal, CuTi type structure) on the catalyst surface. In this crystal structure, all of the first nearest neighbors of Pd were Zn. No Pd-Pd surface ensemble sites remained, which effectively turned off the structure-sensitive pathway for hydrogenolysis. This work suggested that specific intermetallic compound structure could play a crucial role in determining the selectivity of LAD catalysts. Although monometallic Pd catalysts are typically non-selective for LAD, certain Pd IMC structures may be selective catalysts.

Indium has also been reported as a promoter for Pt based bimetallic light alkane dehydrogenation catalysts. [13-15] However, the exact structure of the bimetallic particles and their influence on catalyst function have not been studied. Studies on Pd-Zn propane dehydrogenation catalysts suggest that intermetallic compound structures may also play an important role in these In promoted LAD catalysts. [11, 12] In and Pd can form 6 Pd-In IMC

phases with different stoichiometries at 600 °C (Figure 2.1). [16] The ordered arrays of two different atom types over specific crystallographic sites characteristic of IMCs give rise to Pd active sites with specific geometric coordination, which is in contrast to alloys where the metal atoms randomly substitute in solid solutions. [17] IMCs formed by In with Pd and other noble metals have recently been reported to exhibit improved catalytic properties in methanol steam reforming and amination of alcohols. [18-20]

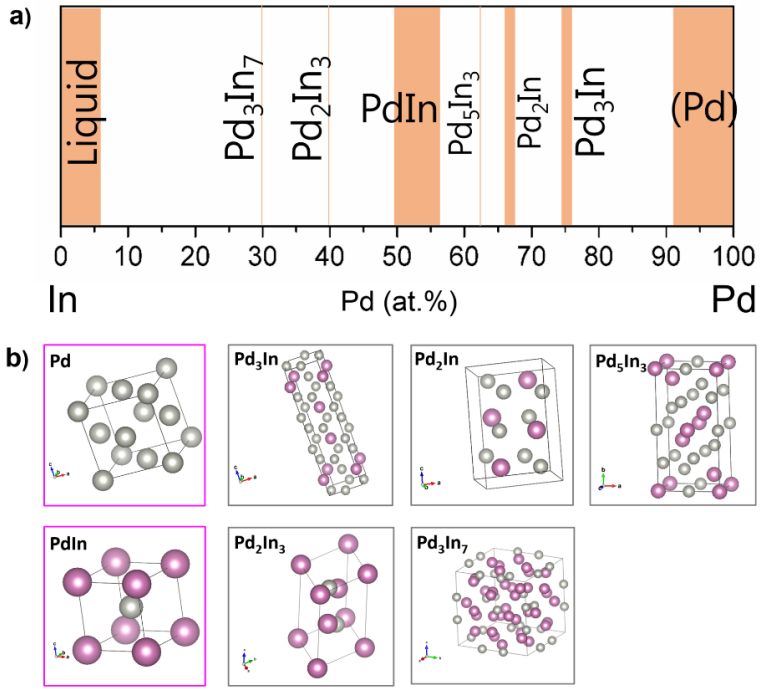

Figure 2.1: a) In-Pd phase diagram at 600 °C adapted from Okamoto et.al. [21] and b) crystal structure of Pd and different Pd-In intermetallic compound phases [22-26]

Determining the crystal structure of supported catalyst nanoparticles is, however, challenging. The small particle size (< 3 nm), low metal loading (< 5 wt. %) and large background from typical amorphous catalyst supports (SiO_2 and γ-Al_2O_3) usually make detection of nanoparticle structure using laboratory XRD instruments very difficult. Gallagher *et al.* recently showed that resolving the broadened diffraction peaks of ~ 2 nm monometallic Pt nanoparticles required *in situ* measurements under H_2 flow and a high signal-to-noise ratio only obtainable from synchrotron radiation. [27] For bimetallic particles, the problem is further complicated since

several structures may be present, [12, 28] resulting in overlapping of multiple broad diffraction peaks. In addition, the diffraction peaks of some IMCs show up at 2θ values very close to those of the parent metals or the other IMCs, for which high spatial resolution of diffraction peaks is required.

Here, we report on the synthesis, testing and characterization of silica supported Pd and Pd-In nanoparticle catalysts with different In:Pd ratios and similar particle size of about 2 nm. The catalysts were characterized by scanning transmission electron microscopy (STEM), infrared spectroscopy of adsorbed CO (CO IR), *in situ* synchrotron X-ray absorption spectroscopy (*in situ* XAS) and *in situ* synchrotron X-ray diffraction (*in situ* XRD). The ethane dehydrogenation reaction was used to evaluate the influence of In on the catalysts' performance. Detailed crystal structure and particle geometry were determined for the nanoparticles with mixed metal and intermetallic compound phases. Their relation with catalyst function is further discussed, suggesting the role of In as both a geometric and an electronic promoter.

2.3 Experimental

2.3.1 Catalyst Preparation

A monometallic Pd catalyst (2 wt. % Pd supported on Davisil 636 silica gel from Sigma–Aldrich, 480 m^2/g and 0.75 mL/g pore volume) was synthesized using the incipient wetness impregnation (IWI) method. 2.81 g of 10 % $Pd(NH_3)_4(NO_3)_2$ solution (Sigma–Aldrich) were dissolved in 1.5 mL of H_2O. 30% ammonium hydroxide solution (Sigma–Aldrich) was then added to the solution until the pH reached 11. The obtained Pd precursor was added dropwise to 5 g of silica and stirred. After drying overnight at 125 °C, the sample was calcined at 500 °C for 3 h and reduced at 200 °C in 5 % H_2/N_2 at 100 cm^3/min for 30 minutes.

A series of Pd-In bimetallic catalysts with target Pd loading of 2 wt. % and In loading of 1, 3, 6 wt. % were synthesized by sequential incipient wetness impregnation (s-IWI) under controlled pH conditions. Various amounts of $In(NO_3)_2$ hydrate (Sigma-Aldrich) were dissolved in about 8 mL of H_2O. Citric acid (Sigma-Aldrich) was added to this solution with a molar ratio of 1:3 to the In in the solution. About 5 mL of 30 % ammonium hydroxide solution was then added to this solution to initially form a white precipitate which dissolved later when additional ammonium hydroxide solution was added. The obtained solution at pH = 11 was added dropwise to 15 g of

silica and stirred. The obtained In/SiO_2 catalyst precursors were dried overnight at 125 °C and then calcined at 600 °C for 3 h. 3.37 g of 10 % $Pd(NH_3)_4(NO_3)_2$ solution were dissolved in ammonia and then added dropwise to 6 g of the obtained In/SiO_2. This catalyst was then dried overnight at 125 °C, calcined at 200 °C for 3 h, reduced at 200 °C in 5 % H_2/N_2 at 100 cm^3/min for 30 min, and then reduced at 600°C in 5% H_2/N_2 at 100 cm^3/min for 30 minutes. These samples are named after the atomic ratio of In: Pd determined by atomic absorption spectroscopy (Table 2.1).

2.3.2 Atomic Absorption Spectroscopy (AAS)

The elemental loadings of Pd and In in the catalyst samples were measured using a PerkinElmer AAnalyst 300 atomic absorption spectrometer. Approximately 40 mg of each sample were dissolved in 2 ml HF (48 wt. %, Macron chemicals) overnight followed by the addition of about 50 ml D.I. water to dilute the concentrated acid solution. AAS standards for Pd and In (Fluka) were diluted to within the linear detection range and used for calibrating the instrument. Weight percentages of Pd and In were calculated from the average absorbance value of two repeat measurements and the atomic ratios of Pd to In were calculated from the obtained weight percentage.

2.3.3 Scanning Transmission Electron Microscopy (STEM)

The STEM images were taken at Birck Nanotechnology Center at Purdue University using the FEI Titan Scanning Transmission Electron Microscope (80-300 kV, 1 nm spatial resolution in STEM). Samples were ground to fine powders and dispersed in isopropyl alcohol. Three drops of the solution were added onto an ultrathin Carbon film-Au TEM ready grid (TedPella) and dried on a hot plate at 80 °C. STEM images were taken using the high angle annular dark field (HAADF) detector at 300 kV and particle size was counted using the ImageJ program. [29] A minimum of 200 particles were counted to obtain the size distribution for each catalyst.

2.3.4 CO Chemisorption

The CO chemisorption measurements on Pd-In catalysts were conducted using a Micromeritics ASAP 2020 chemisorption instrument. Around 0.1 g of each catalyst was loaded into a U-shaped quartz reactor tube. The catalysts were reduced in 50 cm^3/min of 5 % H_2/He at 600 °C for 0.5 h and cooled to RT under the same atmosphere. The sample was then flushed for 30 minutes in He before evacuation and measurements. Difference analysis of the chemisorption

curve was used to obtain the catalyst dispersion. A stoichiometry of CO: Pd =1:1 was assumed in order to estimate the lower bound of dispersion value for Pd-In catalysts.

2.3.5 Ethane Dehydrogenation Kinetics

Ethane dehydrogenation kinetics measurements were carried out in a quartz fixed-bed reactor with 3/8-inch ID. The weight of the catalysts used ranged from 0.2 g to 0.65 g. A thermocouple within a quartz thermocouple well was placed at the bottom center of the catalyst bed to measure the reaction temperature inside the bed. The products were analyzed with Hewlett Packard 5890 Series II gas chromatograph equipped with a thermal conductivity detector (TCD). Before each test, the catalyst was first reduced under 40 cm^3/min 5% H_2/N_2 while the temperature was raised to 600 °C and held at 600 °C for 30 minutes. For selectivity comparison at 15% conversion at 600 °C, a reaction atmosphere of 5 % C_2H_6, 6 % H_2 balanced in N_2 with a total flow rate of 50 cm^3/min was used. When measuring the dehydrogenation turnover rate (TOR, per surface Pd site) at 600 °C and the activation energy, the reaction mixture was 5 % C_2H_6, 2 % H_2, 0.5 % C_2H_4, 43.2 % He, and balance N_2 at a total flow rate of 150 cm^3/min. Co-feeding both hydrogen and ethylene helped make sure that the reactor was operated under differential condition, which was typically not considered in previous works on light alkane dehydrogenation kinetics. [2, 3, 14] Approach to equilibrium was also considered for the calculation of TOR following the work of Koryabkina *et al*. [30] The rate expression is as below,

$$rate = k_f[C_2H_6]^a[C_2H_4]^b[H_2]^c(1 - \beta);\ \beta = \frac{[C_2H_4][H_2]}{K[C_2H_6]}$$

where k_f is the forward rate constant, K is the equilibrium constant and β is the approach to equilibrium index. The value of β was found to be always smaller than 0.17, indicating the reaction was run far from equilibrium. Apparent activation energy was measured at 4 different temperatures between 570 and 600 °C after the catalyst stabilized at conversions below 10%.

2.3.6 *In situ* Infrared Spectroscopy

Infrared spectra were collected using a Nicolet 4700 spectrometer equipped with a Hg-Cd-Te (MCT, cooled to -194 °C by liquid nitrogen) detector in transmission mode. Catalysts were diluted with SiO_2 (Davisil 636 silica gel from Sigma–Aldrich, 480 m^2/g and 0.75 mL/g pore

volume) with a catalyst to silica mass ratio of 1:3. The diluted samples were ground to a fine powder and pressed to form a self-supporting wafer (~0.02 g/cm^2). The wafer was sealed in a specially designed quartz cell with CaF_2 windows. Two K-type thermocouples (Omega) were placed 2 mm from the wafer on each side to measure wafer temperatures. The cell was surrounded by a mineral-insulated resistive heating coil (ARi Industries), and both the cell and coil were encased in an alumina silicate ceramic chamber (Purdue Research Machining Services). A custom glass manifold was connected to the cell to control the gas for pretreatment and the amount of CO introduced. The cell was first purged with He, and then the sample was reduced with 10% H_2 in balance He while the temperature was increased to 600 °C and held for 30 minutes. After reduction, the wafer was cooled to 30 °C in the same gas environment. The wafer was then exposed to dynamic vacuum (Alcatel 2008A rotary vane rough pump, <0.1 Torr) for 15 minutes at 30 °C, and a background scan was recorded, which was averaged over 64 scans with 2 cm^{-1} resolution. The sample was then exposed to 20 kPa CO in sequential doses over ~ 30 minutes followed by dynamic vacuum for 30 minutes to remove gas-phase and weakly adsorbed CO before final IR scan was collected.

2.3.7 *In situ* X-ray Absorption Spectroscopy (XAS)

X-ray absorption spectroscopy measurements at the Pd K (24350 eV) edge and In K edge (27940 eV) were made on the 10-BM bending magnet beamline of the Materials Research Collaborative Access Team (MRCAT) at the Advanced Photon Source (APS), Argonne National Laboratory. Measurements were taken in transmission mode. A palladium foil spectrum was acquired through a third ion chamber simultaneously with each measurement for energy calibration. Samples were prepared by grinding the catalysts into fine powders and pressing them into a cylindrical sample holder to form a self-supported wafer. Before the XAS spectra were obtained, the catalysts were reduced at 600 °C in a 4 % H_2/He mixture at 50 cm^3/min flow rate. After reduction, the samples were purged with He at 100 cm^3/min and cooled to room temperature. Trace oxidants in He were removed by passing through a Matheson PUR-Gas Triple Purifier Cartridge containing a Cu trap. All spectra were obtained at room temperature in He.

WINXAS 3.1 software [31] was used to fit the XAS data. The EXAFS coordination parameters were obtained by a least-squares fit in R-space of the k^2-weighted Fourier transform data from Δk = 3.0 to 12.0 Å^{-1}. The first shell fit of the magnitude and imaginary parts were

performed between ΔR = 1.6 to 2.9 Å for the Pd edge. At the In edge, the first shell fit was performed from ΔR = 1.8 to 2.8 Å. An average coordination number and bond distance were determined for Pd-Pd and Pd-In scattering at Pd edge and In-Pd scattering at In edge by fitting with the experimental phase shift and back scattering amplitude of Pd-Pd scattering extracted from Pd foil XAS data (12 Pd-Pd at 2.75 Å). Such treatment was rationalized based on the small difference in phase shift and amplitude between Pd-Pd and Pd-In scattering due to the close atomic number of Pd and In. While fitting the data with both Pd-Pd and Pd-In scattering path was possible, the similarity between these two paths results in varied fitting parameters giving similar fits. Fits were performed by refinement of the coordination number (CN), bond distance (R), and energy shift (E_0). The $\Delta\sigma^2$ value was kept constant for all of the samples through all fits, and CN and R were allowed to vary in turn to determine the correct fit.

2.3.8 *In situ* X-ray Diffraction (XRD)

In situ XRD measurements were performed at the 11-ID-C beamline at the APS, Argonne National Laboratory. Data was acquired in transmission mode using X-rays at 105.091 keV (λ = 0.11798 Å) and a PerkinElmer large area detector. Samples were pressed into a thin pellet and loaded into a Linkam Thermal Stage which allowed reactant gas flow during the *in situ* XRD measurements. The reactor was first purged with Ar for 5 minutes before a flow of 3 % H_2/Ar at 50 cm^3/min was introduced and the temperature was ramped to 600 °C. After reducing at 600 °C for 20 minutes, diffraction patterns were taken for all the samples. Then the reactor was cooled to room temperature in the same atmosphere and diffraction patterns were taken again for all the samples now without thermal-induced lattice distortion and strain. The bare SiO_2 support, in addition to the empty cell, were treated with the same procedure and corresponding reference measurements were taken at the same conditions. The 2-D diffraction patterns were integrated and converted to the conventional 1-D diffraction data using the Fit2D software [32] to obtain plots of intensity versus 2θ. The diffraction patterns of possible Pd-In alloy phases were simulated based on the known structures [22-26] by MAUD (Materials Analysis Using Diffraction) [33] and used as standards to determine the phase obtained.

2.4 Results

2.4.1 Atomic Absorption Spectroscopy (AAS)

The Pd and Pd-In catalysts were prepared by impregnation and pre-reduced at 600 °C before catalyst testing and characterization. It was found that initial reduction of Pd-In catalysts at 600 °C deposited a yellow solid film on the wall of the reactor tube outlet. This yellow color was almost identical to the color of calcined In-impregnated SiO_2 prepared in the first step of the synthesis and is typical of In_2O_3, suggesting that the deposits correspond to some lost In. The elemental loadings for Pd-In catalysts were measured by AAS. Table 2.1 shows the obtained Pd and In contents and the In: Pd ratio in each catalyst. The Pd content for all Pd-In catalysts was close to the target weight loading. The In content, however, was about half of the target loading, confirming partial In loss. After the initial reduction of the catalyst precursor during preparation, subsequent reduction pretreatments of Pd-In catalysts did not lead to significant additional loss of In.

Table 2.1: Elemental Analysis, Particle Size, and Dispersion

Sample Name [a]	Pd Content (wt. %)	In Content (wt. %)	In: Pd Atomic Ratio	Particle Size by STEM (nm)	Dispersion (%) [b]
Pd	/	/	/	1.9 ± 0.9	47
Pd-In-0.2	2.0	0.5	0.2	2.0 ± 0.6	14
Pd-In-0.8	2.0	1.7	0.8	1.8 ± 0.4	12
Pd-In-2.0	1.6	3.4	2.0	2.7 ± 0.9	2

[a] Named with the measured In: Pd atomic ratios for the Pd-In catalysts
[b] Lower boundary values determined by CO chemisorption assuming a stoichiometry of CO: Pd = 1: 1 for Pd-In catalysts. The dispersion of Pd catalyst was estimated using the STEM particle size.

2.4.2 Particle Size and Catalyst Dispersion

Metal nanoparticle sizes of Pd and Pd-In catalysts were determined by STEM imaging. Images were taken for all four catalysts after pre-reduction in H_2 at 600 °C and exposure to air. An image of Pd-In-0.8 catalyst and corresponding size distribution statistics are shown in Figure 2.2 and are typical of the other samples. The average particle size of this sample was determined to be 1.8 nm with a standard deviation of 0.4 nm. Obtained average particle sizes for the other samples are reported in Table. 2.1. Except for Pd-In-2.0, all the catalysts have roughly the same particle

size of about 2 nm. Pd-In-2.0 has slightly larger particles of 2.7 nm. The similar particle sizes of these catalysts enable comparison between their kinetics and surface structure without having to account for the changes in particle size.

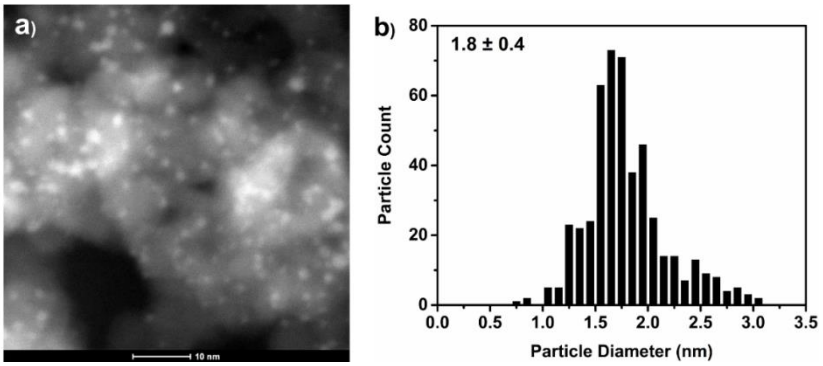

Figure 2.2: a) STEM HAADF image and b) particle size distribution statistics of Pd-In-0.8 sample

The Pd dispersions of the catalysts were determined from CO chemisorption analysis or STEM particle size. For the monometallic Pd catalyst, the dispersion was estimated to be 47% using the average particle size. For Pd-In catalysts, the lower boundary values of dispersion were calculated from the CO uptake in CO chemisorption analysis assuming a stoichiometry of CO: Pd = 1: 1. The IR spectra discussed below show a high fraction of linearly bound CO; thus this assumption is a reasonable estimate. The dispersion values were found to be 14 % for Pd-In-0.2 and 12 % for Pd-In-0.8 catalysts, lower than that of the Pd catalyst with similar particle size, suggesting possible covering of the surface by some In species. The dispersion of the Pd-In-2.0 catalyst was even lower (2 %) and much smaller than one would expect for a catalyst with 2.7 nm nanoparticles. Surface coverage by a species which does not chemisorb CO is likely for this sample.

2.4.3 Ethane Dehydrogenation Kinetics

The catalytic performance of Pd and Pd-In catalysts were determined for ethane dehydrogenation at 600 °C. At this temperature, methane was the only side product (due to ethane hydrogenolysis). Calcined In impregnated silica showed negligible catalytic activity. The conversion in all tests are below 10 % and far from equilibrium as confirmed by approach to equilibrium index β. The TORs were tested at 600 °C, corrected by approach to equilibrium index

β and normalized by the amount of surface Pd obtained from chemisorption (Table 2.1). Apparent activation energy (E_a) was measured at 4 different temperature between 570 and 600 °C after catalysts stabilization. The results for the Pd and PdIn catalysts are shown in Table 2.2 and Figure 2.3. The product distribution was calculated for each catalyst at 15 % ethane dehydrogenation conversion. While the Pd catalyst had an ethylene selectivity of 53 % typical of noble metal nanoparticles, the Pd-In catalysts showed much higher selectivity. Pd-In-0.2 was 98 % selective to ethylene and Pd-In-0.8 was near 100 %. Pd-In-2.0 had a stabilized selectivity of 99 %.

Table 2.2: Catalytic performance and kinetic parameters of ethane dehydrogenation

Sample	Selectivity (%) at 15 % conversion [a]		Initial TOR (s^{-1}) [b]	TOR after 3 h (s^{-1}) [b]	Apparent E_a (kJ/mol) [b]
	C_2H_4	CH_4			
Pd	53	47	0.03	0.003	/
Pd-In-0.2	98	2	0.09	0.03	102
Pd-In-0.8	100	0	0.26	0.12	130
Pd-In-2.0	99	1	0.21	0.16	128

[a] Measured under 5 % C_2H_6, 6 % H_2, and balance N_2 with a total flow rate of 50 cm^3/min at 1 atm and 600 °C. The equilibrium conversion is 27 %.
[b] Measured under 5 % C_2H_6, 2 % H_2, 0.5 % C_2H_4, 43.2 % He, and balance N_2 with a total flow rate of 150 cm^3/min at 1 atm

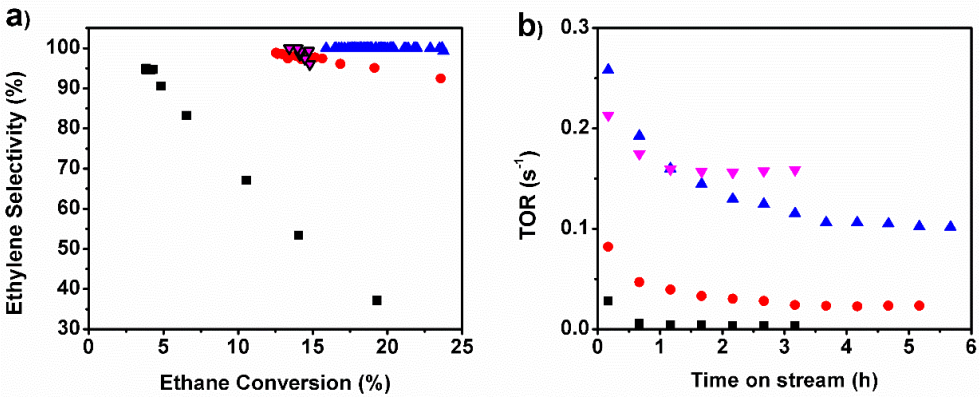

Figure 2.3 Plots of a) Conversion vs selectivity of ethane dehydrogenation measured in 50 cm^3/min of 5 % C_2H_6, 6 % H_2 balanced in N_2 at 1 atm and 600 °C and b) Turnover rate (TOR) vs time on stream measured in 150 cm^3/min of 5 % C_2H_6, 2 % H_2, 0.5 % C_2H_4, 43.2 % He, and balance N_2 at 1 atm and 600 °C of Pd (black square), Pd-In-0.2 (red circle), Pd-In-0.8 (blue up triangle) and Pd-In-2.0 (magenta down triangle) catalysts.

The TORs (low concentrations of H_2 and ethylene products were co-fed with the ethane) were measured under differential conditions (Table 2.2 and Figure 2.3b). Normalizing the moles of ethane converted per second to the moles of surface Pd atoms (using the dispersion value in Table 2.1), the initial TORs were determined for each catalyst and were 0.03 s^{-1}, 0.09 s^{-1}, 0.26 s^{-1} and 0.21 s^{-1} for Pd, Pd-In-0.2, Pd-In-0.8 and Pd-In-2.0, respectively. The TORs of Pd-In-0.8 catalyst increased almost 10 fold compared to monometallic Pd, indicating that In promoted the ethane dehydrogenation reaction rate. The stability of these catalysts was also found to be very different. While Pd quickly deactivated to low conversion, the Pd-In catalysts deactivated moderately within the first 2-3 h and reached a stable conversion, allowing activation energy to be measured. Although the selectivity is close to 100 % for the Pd-In catalysts, there is a small amount of coke deposition over time which contributes to slow activity loss.

The apparent activation energy measurements were performed on Pd-In catalysts after stabilization at similar conversions below 10 % (see Arrhenius plot in Figure. A.1). The results are also shown in Table 2.2. Pd deactivated too rapidly to determine a reliable activation energy. The E_a of Pd-In-0.2 was 102 kJ/mol, and for both Pd-In-0.8 and Pd-In-2.0 it was around 130 kJ/mol. The significantly different E_a of Pd-In-0.8 and Pd-In-2.0 from that of Pd-In 0.2 and the higher TOR's of the former suggests that the two catalysts with higher In loading may have different surface structure compared with Pd-In-0.2 and In likely modifies the electronic properties of Pd for ethane dehydrogenation reaction.

2.4.4 *In situ* Infrared Spectroscopy

In situ IR of chemisorbed CO on reduced Pd and Pd-In catalysts are shown in Figure 2.4. In each spectrum there are two characteristic CO bands, one from 2000 cm^{-1} to 2100 cm^{-1} assigned to linearly adsorbed CO and a second between 1700 and 2000 cm^{-1} associated with bridge bound CO. [34, 35] For the monometallic Pd catalyst, the IR spectrum is dominated by the broad bridge bound CO band. This broad band possibly contains two or more peaks including the ones between 1750 and 1900 cm^{-1} assigned to CO bridge bound on terrace and hollow Pd sites and the ones between 1900 and 2000 cm^{-1} attributed to CO bridge bound to corner and edge sites. [35-38] The linear bound CO band is a small feature on the ~ 2 nm monometallic Pd catalyst. For the Pd-In samples, however, the linear CO peak is much more pronounced, with peak maxima between 2060 cm^{-1} and 2070 cm^{-1}. While the bridge bound CO peak is large relative to the linear bound peak in

Pd-In-0.2 sample, its intensity decreases with increasing In content. For Pd-In-0.8 and Pd-In-2.0, the bridge bound CO peaks are small. The feature between 1750 and 1850 cm^{-1} is no longer present, indicating few terrace and hollow Pd sites in these catalysts.

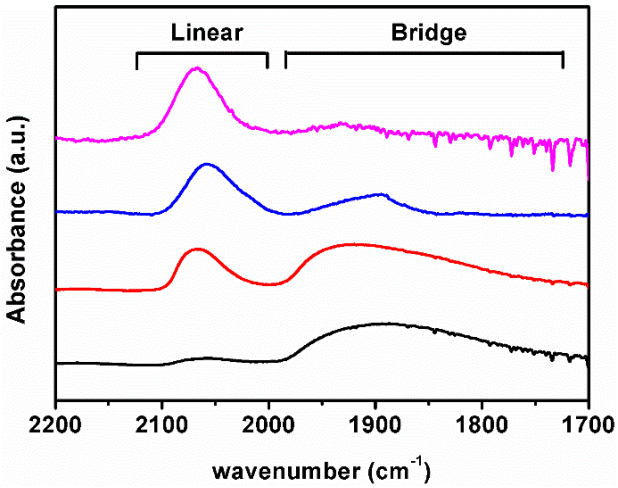

Figure 2.4: IR spectra of adsorbed CO measured after saturation and subsequent evacuation (1800 s, 0.1 Torr, 30 °C) for Pd (Black), Pd-In-0.2 (red), Pd-In-0.8 (blue) and Pd-In-2.0 (magenta) catalysts. The IR signal intensity has been normalized by the thickness of each sample wafer (using the mass of the wafer and a constant cross-sectional area) and the CO chemisorption uptake obtained from chemisorption analysis, so as to be compared on a per surface Pd atom basis.

Table 2.3: Bridge-to-linear peak area ratio from CO IR spectroscopy

Sample name	Bridge to linear ratio
Pd	21 : 1
Pd-In-0.2	3.2 : 1
Pd-In-0.8	0.63 : 1
Pd-In-2.0	0.13 : 1

A decrease in the ratio of bridge bound to linear bound CO is observed with increasing In loading, Table 2.3. Bridge-to-linear ratios for the catalysts were determined by dividing the total peak area between 1700 and 2000 cm^{-1} by the peak area between 2000 and 2100 cm^{-1}. Though these ratios do not take into consideration the extinction coefficients of the different CO adsorption bands and are not quantitatively related to the CO coverages of the various Pd sites, the ratios reflect qualitative changes in the surface of the catalysts. The monometallic Pd catalyst has a bridge

to linear ratio of 21, i.e., primarily bridge bound CO bound to Pd terrace and hollow sites. With increasing In loading, the ratio decreases to 3.2 for Pd-In-0.2, 0.63 for Pd-In-0.8 and finally to 0.13 for Pd-In-2.0. In the Pd-In-0.8 and 2.0 samples, the relative proportion of Pd terrace and hollow sites is significantly reduced and Pd sites capable of binding CO linearly are predominant. The shift in the CO binding mode suggests that In breaks the Pd ensembles and creates isolated Pd sites binding CO linearly. Though Pd atoms with low coordination number are typically thought to be responsible for linear bound CO, the new linear Pd sites are likely from the bimetallic nanoparticle formation since the particle size of the monometallic Pd and Pd-In catalysts are similar.

2.4.5 *In situ* X-ray Absorption Spectroscopy (XAS)

The local structure of Pd and In atoms was determined by *in situ* X-ray absorption spectra (*in situ* XAS) for the Pd and Pd-In catalysts. The spectra were taken at room temperature after the catalysts were pre-reduced in H_2/He at 600 °C. The XANES and EXAFS spectra at both the Pd and In edges are shown in Figure A.2 and Figure 2A.3 for Pd-In-2.0 and is typical of the other Pd-In catalysts (See Figures 2.10, 2.11 for the spectra of Pd, Pd-In-0.2 and Pd-In-0.8). Comparing the Pd edge XANES of Pd-In-2.0 catalyst to Pd foil the edge energy (24350 eV) and white line intensity are similar between these 2 samples indicating the Pd-In-2.0 catalyst is fully reduce to metallic Pd; however, there are some small differences in the shape of the XANES suggesting additional metallic atoms in the nanoparticles. The white line in Pd-In-2.0 decreases slightly in intensity compared to Pd foil (Figure 2.5a), suggesting that Pd has some metallic In neighbors. The EXAFS of Pd-In-2.0 looks similar to that of Pd foil (Figure 2.5b), but with slightly longer bond distance (Table 2.4). Pd and In have a similar number of electrons, therefore, scatter similarly. Nevertheless, difference can still be observed in the position and shape of the scattering peaks corresponding to the first coordination shell, due to the existence of In neighbors and their different bond distance. At the In edge, the edge energy in the XANES of Pd-In-2.0 and In_2O_3 are similar (27940 eV), but the intensity of the white line in Pd-In-2.0 is significantly lower than that in In_2O_3 (Figure 2.6a), which indicates that some metallic In is also present in the sample. This is confirmed in the In edge EXAFS of Pd-In-2.0 as major scattering peak at R = 2.6 Å (phase uncorrected distances) typical for 4d metal is observed (Figure 2.6b). [39] Spectra with the same features were obtained for Pd-In-0.2 and Pd-In-0.8 catalysts, indicating bimetallic interactions in all Pd-In catalysts studied.

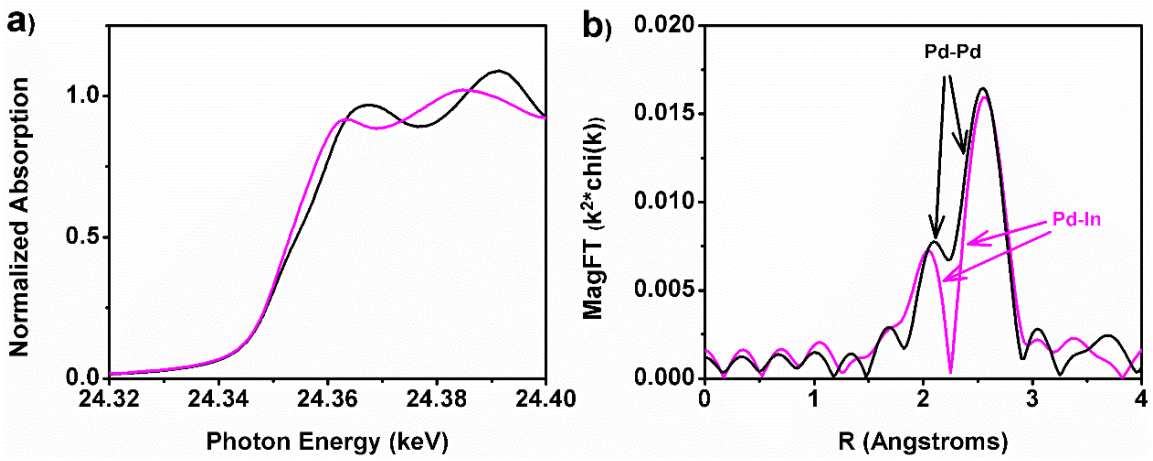

Figure 2.5: Pd K edge a) XANES and b) magnitude of the Fourier Transform of the EXAFS of Pd-In-2.0 (magenta) with Pd Foil Standard (black, 1/3 the original FT EXAFS magnitude). k^2: Δk = 3.0 - 12.0 Å

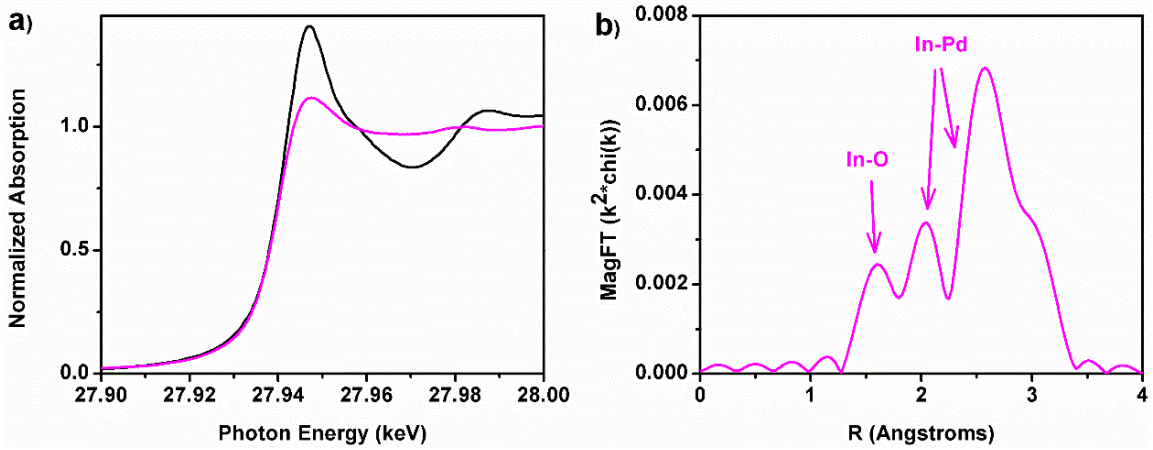

Figure 2.6: In K edge a) XANES of Pd-In-2.0 (magenta) with In_2O_3 Standard (black) and b) magnitude of the Fourier Transform of the EXAFS of Pd-In-2.0 (magenta). k^2: Δk = 3.0 - 12.0 Å

The k^2-weighted EXAFS at both the Pd and In edge of all the samples were fit and the results are given in Table 2.4 (graphical fitting results are shown for Pd-In-2.0 in Figures A.4 and A.5). At the Pd edge, an average coordination number and bond distance was determined for Pd-Pd and Pd-In scattering by fitting with a single Pd-Pd scattering path, since Pd-Pd and Pd-In scattering are very similar. At the In edge, In-Pd scattering was also fitted with the Pd-Pd scattering reference. The average coordination number of In from the fit is the number of In-Pd neighbors normalized to all the In atoms in the sample (including the metallic In in all the Pd-In catalysts and

the oxidized In in two of the catalysts Pd-In-0.8 and Pd-In-2.0). Therefore, for samples containing oxidized In, the obtained coordination number is lower than the expected value for fully reduced In. While for Pd-In-0.8 and Pd-In-2.0 contributions from In-O scattering in the range of R = 1.0-1.8 Å (phase uncorrected distances) are observed, due to the nature of light scattering, their intensity are very low and, therefore, the In-O scattering was not possible to fit. For Pd-In-0.2, the In-Pd coordination number is 8.0 and the bond distance is 2.80 Å, shorter than that of In metal at 2.87 Å, which implies the In has Pd neighbors. At the Pd edge, average Pd-Metal (Pd-M) coordination number is 10.8 and the bond length is 2.78 Å, longer than the values for Pd foil (12 at 2.75 Å), suggesting that there are Pd-In bonds in the first coordination shell. For Pd-In-0.8 and Pd-In 2.0 the Pd-M and In-M bond distances were similar to those of Pd-In-0.2, also indicating the presence of bimetallic nanoparticles, but the coordination numbers vary with changing composition of the nanoparticles and the amount of unreduced In oxide in the samples (see section 2.5.1).

Table 2.4: EXAFS fitting parameters for Pd-In catalysts

Sample Name	Scattering Path	Coordination number	Bond distance (Å)	Debye Waller Factor $\Delta\sigma^2$ (10^{-3})
Pd	Pd-Pd	8.4	2.75	5
Pd-In-0.2	Pd-M	10.8	2.78	5
	In-M	8.0	2.80	5
Pd-In-0.8	Pd-M	7.9	2.77	5
	In-M	5.1	2.78	5
Pd-In-2.0	Pd-M	7.6	2.79	5
	In-M	3.7	2.80	5

2.4.6 *In situ* X-ray Diffraction

While XAS identified that Pd and In formed bimetallic nanoparticles, it was not possible to determine if, or which, ordered structures were formed. To investigate the phase assemblage of the sub-3 nm Pd-In bimetallic nanoparticles, *in situ* synchrotron X-ray diffraction was performed. Background subtracted diffraction patterns were obtained for Pd-In catalysts at 600 °C and at room temperature after reduction (Figure 2.7a). It was found that except for peak displacement caused by thermal induced lattice expansion, the spectra taken at 600 °C (Figure A.6) were very similar

to those taken at RT, indicating unchanged crystal structure of the catalysts at the two different temperatures. The RT patterns were compared to standard diffraction patterns of Pd, Pd-In intermetallic compounds and Indium oxides. No In-only species were identified in the diffraction patterns. FCC Pd and cubic PdIn intermetallic compound (IMC) with a CsCl type structure (shown in Figure 2.7b) were the only two phases observed for the Pd-In nanoparticles. Simulated diffraction patterns of Pd and cubic PdIn IMC structures (dotted, Figure 2.7a) are thus plotted together with the diffraction patterns of the Pd-In catalysts (solid, Figure 2.7a).

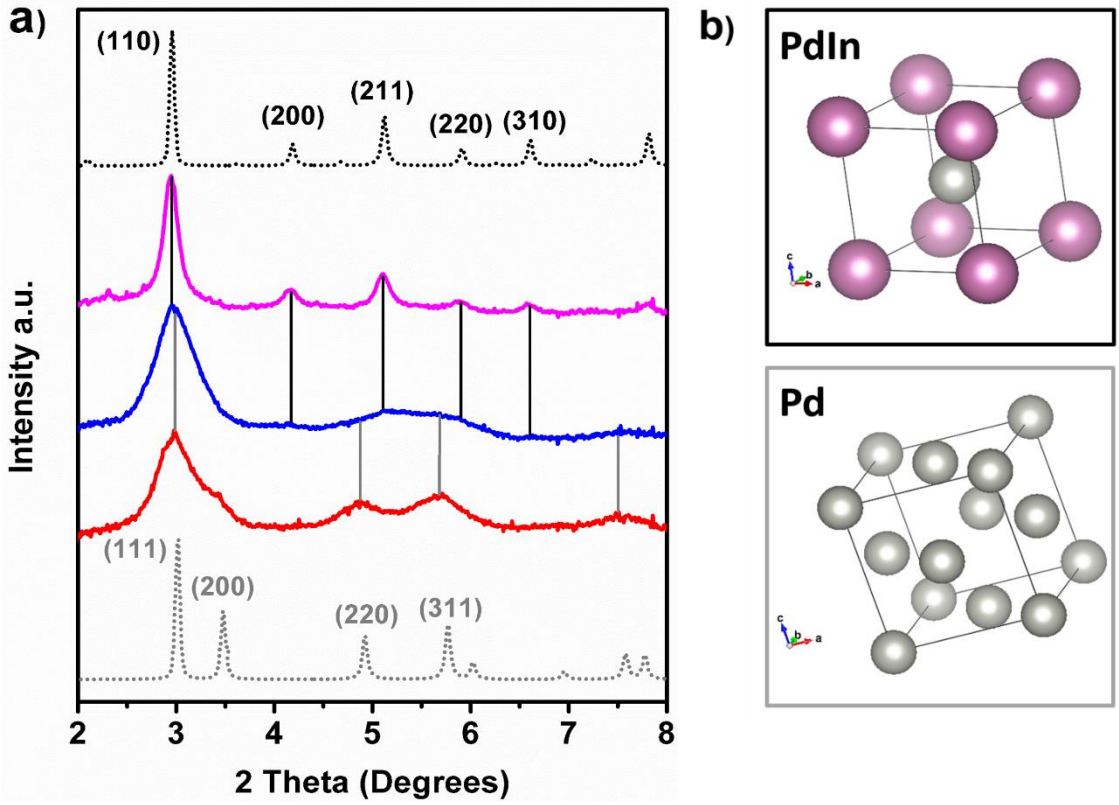

Figure 2.7: a) Background subtracted *in situ* XRD pattern of Pd-In-0.2 (red), Pd-In-0.8 (blue), and Pd-In-2.0 catalyst (magenta, 1/2 the original peak intensity) compared with the simulated XRD pattern (with major peaks indexed) of bulk FCC Pd (grey, dotted), and bulk PdIn intermetallic compound phase (black, dotted). The grey vertical line marks the diffraction features in the samples from FCC Pd phase, while the black vertical line marks those from PdIn IMC phase. b) the crystal structure of PdIn IMC with CsCl type structure and FCC Pd metal

Despite the very low intensity (See Figure A.7 compared to amorphous silica background) and broad shape of the diffraction peaks arising from small particle size (ca. 2 nm), due to the very

high resolution (0.005 °) and signal to noise ratio of synchrotron data it is possible to identify which phases were present in each sample. For Pd-In-2.0 with the highest In loading, its diffraction pattern shows only peaks corresponding to the cubic PdIn IMC phase. The peaks are slightly broadened compared to the simulated bulk PdIn XRD pattern. The crystallite size calculated using the FWHM of the (110) peak is 3.3 nm, slightly larger than the average particle size determined from the STEM image (2.7 nm). This is common for size estimation using these two techniques since STEM measures number distributions while XRD measures volume weighted distributions. [27] For nanoparticles in this size, its high surface portion (30 - 40 %) means any local or surface structure different from the bulk particle would give rise to additional diffraction features or extra peak broadening in the XRD pattern. Accordingly, absence of these features for this catalyst indicates that the nanoparticles are well ordered PdIn IMC.

Identification of the crystal phases in Pd-In-0.8 catalyst is less straightforward. The pattern contains weak features of both Pd and PdIn IMC. Two local maxima can be identified for the most intense peak in this sample. One maximum is observed at 2.95 °, corresponding to the PdIn (110) peak, and another is observed at 3.01 °, which is the position of Pd (111) peak of FCC Pd suggesting diffraction from both phases. Other diffraction features of these two phases are shown by the broad peaks centered around 4.9 °, 5.7 °, and 7.6 ° for FCC Pd marked by the grey vertical lines and the small peaks at 4.1 °, 5.1 °, 5.9 °, and 6.6 ° for PdIn IMC marked by the black vertical lines. These diffraction peaks are very broad and overlapping. Therefore the crystallite size estimated from the FWHM of the most intense peak using the Sherrer equation 1.3 nm would be smaller than the actual crystallite size. The average size from STEM imaging for this catalyst is 1.8 nm.

For Pd-In-0.2, while XAS indicated some In-metal scattering, only broad peaks similar to those of FCC Pd metal were present. Compared to standard FCC Pd, the peaks in Pd-In-0.2 are slightly shifted to lower angle (0.04° for the most intense (111) peak). The shift in peak position increases with 2θ value, suggesting that it is related with increased lattice parameter, i.e. lattice expansion, due to the presence of In in the nanoparticles. Using Bragg's law, the increased lattice parameter is calculated from the peak position of the most intense (111), (220) and (311) peak. The average value is found to be 3.93 Å, corresponding to an average Pd-M bond distance of 2.78 Å, which is in agreement with EXAFS fitting results. The crytallite size estimated from the FWHM

of (111) peak using Sherrer equation is 1.4 nm, which is smaller than the STEM determined particle size 2.0 nm also due to overlapping of diffraction peaks.

2.5 Discussion

2.5.1 Detailed Structure Analysis of Pd-In Intermetallic Catalysts

The structure of Pd-In catalysts with three different In: Pd ratios have been investigated by *in situ* IR, XAS and XRD. While IR shows there are changes occurring at the nanoparticle surface, XAS reveals local structure, and XRD identifies the long-range order of atoms in the catalyst. Combined analysis of these results sheds light on the details of the change of the catalyst structure.

For the Pd-In-2.0 catalyst, XRD indicates that the nanoparticles are very likely fully alloyed cubic PdIn IMC with CsCl type structure, in which Pd has only 8 In and In has 8 Pd as first nearest neighbors at a bond distance of 2.81 Å. [22] EXAFS fitting gives a Pd-M bond distance of 2.79 Å with a coordination number of 7.6 and a In-M bond distance of 2.80 Å, all close to the theoretical coordination environment of the PdIn IMC structure. The average coordination number for In is lower than the expected value 8 as the number of In-Pd neighbors is normalized to both the In in InPd and a roughly identical amount of In oxide estimated from the atomic ratio of In to Pd in the catalysts. The isolation of Pd atoms by In atoms expected for PdIn IMC structure on the particle surface is confirmed by the CO IR, which shows predominantly linear bound CO. The very low CO chemisorption capacity and the low intensity of the IR peaks of this sample compared to the other ones in similar particle size suggest that much of the catalytic surface is covered with non-catalytic In species.

For the Pd-In-0.8 catalyst, a mixture of Pd and PdIn IMC phases was identified by XRD. However, the nanoparticle surface is very likely in PdIn IMC structure only. *In situ* IR shows predominantly linear bound CO, which means the surface has mostly isolated Pd atoms. Pd-In-0.8 undergoes almost identical ethane dehydrogenation kinetics compared with Pd-In-2.0, as shown by their similar selectivity, TOR and their almost identical activation energy, suggesting that they probably have the same PdIn surface structure. Both IR and kinetics results do not favor presence of monometallic Pd on the catalyst surface though it is found to be present in the bulk, indicating a morphology of a Pd-core/PdIn-IMC shell structure. Comparison of the structure of Pd-In-0.8 to that of Pd-In-2.0 suggests that intermetallic alloy formation occurs starting at the surface of Pd

nanoparticles followed by the inward growth of the intermetallic alloys, which has been previously reported for β_1-PdZn alloy catalyst. [40, 41]

At low In loadings, for Pd-In-0.2, only Pd nanoparticles could be identified by XRD. Nevertheless, it is clear from the partial improvement in the ethane dehydrogenation selectivity, an increase in the L/B ratio in IR, and the presence of metallic In-M scattering peaks at the In EXAFS that the nanoparticles surface are not just metallic Pd. The In EXAFS fit gives CN = 8.0 and a bond length of 2.80 Å, almost identical to the expected value for PdIn IMC, suggesting that the majority of In atoms likely form a local PdIn IMC structure. The average bond distance of Pd-M neighbors, 2.78 Å, is between the expected values of those of FCC Pd and the Pd in PdIn structure. The average coordination number of Pd 10.8 is higher than that of monometallic Pd nanoparticles in similar size, likely indicating that there are fewer low-coordination surface Pd atoms in this catalyst, i.e., there are also surface In. *In situ* IR also shows increased linear bound CO, which suggests the formed PdIn IMC is present on the particle surface. It seems that PdIn IMC is preferentially formed over other more Pd rich IMC or substitutional solid solution even at relatively low In loading. Similar phenomenon has been previously reported for a series of Rh-In/C intermetallic catalysts. [19]

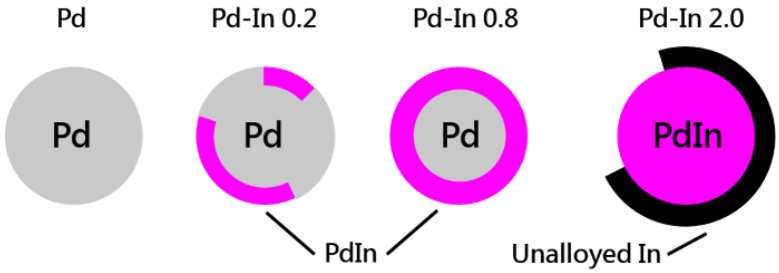

Figure 2.8: Schematic model of geometric structure of the Pd and Pd-In catalysts

In summary, combined analysis of particle size, *in situ* IR, XAS and XRD leads to a general picture of the structure of Pd-In catalysts with different loadings. The evolution of Pd-In nanoparticle structure with increasing In content is demonstrated by a schematic model in Figure 2.8. Pd-In catalysts with increasing In loading have increasing fraction of the nanoparticles transformed from Pd to cubic PdIn IMC with a CsCl type structure. It is very likely that Pd-In-0.2 has an FCC Pd core structure with its surface partially transformed into PdIn alloy and Pd-In-0.8

has a Pd-core with PdIn shell structure. At higher loadings, for Pd-In-2.0, the PdIn IMC structure is fully formed; however, part of the nanoparticle surface is covered by non-catalytic In species.

2.5.2 Structure-function Relationship of Pd-In Intermetallic Catalyst: the Promotion Effect of Indium

Section 2.5.3 shows the ethane dehydrogenation performance (including selectivity, stability, TOR, and apparent activation energy) of Pd and Pd-In catalysts. As with catalyst structure, it is found to vary with In loading. Pd exhibits low selectivity (53 % at 15 % conversion), initial TOR (0.03 s^{-1}) and stability (fast deactivation). When a limited amount of In is introduced, the catalyst performance is greatly improved as seen in Pd-In-0.2. It becomes highly selective (> 97 %), more active (0.09 s^{-1} initial TOR), and stable (0.03 s^{-1} TOR after 3h). Higher In loading results in further improved performance. For Pd-In-0.8 and Pd-In-2.0 catalysts, further increases are seen in their selectivity (> 99 %), initial TOR (0.26 s^{-1} and 0.21 s^{-1}) and TOR after 3 h (0.12 s^{-1} and 0.16 s^{-1}). The latter two catalysts have similar selectivity, TOR and almost identical apparent activation energies (130 kJ/mol) for ethane dehydrogenation, possibly suggesting similar active sites. However, Pd-In-2.0 catalyst has a much lower dispersion and rate per gram compared with Pd-In-0.8. Excess In in the catalyst leads to blocking of active Pd sites and lower activity per gram, although the TOR and Ea of the exposed sites are unchanged.

Correlating the catalyst function with the surface structure suggests that formation of the PdIn IMC leads to higher ethane dehydrogenation selectivity. Pd nanoparticles have Pd ensembles, which catalyze hydrogenolysis. As the fraction of the surface of PdIn IMC increases, and the fraction of ensemble sites decreases, the olefin selectivity increases. Additionally, the TOR and Ea significantly increase. When the surface contains only isolated, catalytically active Pd atoms, the hydrogenolysis (and rapid coke formation) is nearly eliminated. PdIn IMC has a cubic CsCl type structure where the first nearest neighbors of Pd are In atoms at a bond distance of 2.81 Å. The Pd-Pd distance is much longer at 3.25 Å. Thus, all catalytic Pd sites are isolated by the non-catalytic In atoms. This site isolation eliminates the Pd-Pd terrace ensembles responsible for the structure-sensitive reaction, i.e., ethane hydrogenolysis. As a result, this undesirable side reaction is turned off, leaving only structure-insensitive dehydrogenation reactions and a highly selective catalyst. As evidenced from *in situ* IR, Pd terrace and hollow sites are greatly reduced on Pd-In-0.8 and Pd-In-2.0 and isolated Pd sites dominate in these two catalysts.

Changes in nanoparticle composition and geometric structure often concomitantly lead to change in the electronic properties of the catalytic atoms, [42] which may be related with changes in catalyst TORs and E_a. Many previous studies have emphasized the importance of electronic modification in promoting catalyst activity. [4, 6-9, 43] For the Pd-In-0.8 and Pd-In-2.0 catalysts with PdIn IMC surface, although their TORs 0.2-0.3 s^{-1} are lower than the reported TOR 2-3 $s^{-1}$of Pt-In and Pt-Sn catalysts, [14] which suggests that Pt is more active than Pd for ethane dehydrogenation, their TORs are almost 10 times higher than that of monometallic Pd, showing that In is promoting the activity of the Pd catalyst for ethane dehydrogenation. The Pd edge XAS of the Pd-In catalysts shows changes in the shape of the XANES compared to monometallic Pd, indicating a possible change in the electronic properties of Pd due to PdIn IMC formation which may be related with the change in TORs. [14] Further studies to understand the changes in electronic structures of intermetallic alloys compared to monometallic metals by density functional theory are in progress.

Overall, promotional effect of In appears to be both geometric, i.e., isolation of the active Pd atoms, leading to high selectivity and lower deactivation rates, and electronic due to formation of Pd-In bonds leading to higher TOR's and higher activation energies.

Geometric effects have been discussed in a number of previous studies on bimetallic Pt light alkane dehydrogenation catalysts. [3, 10, 14] It has been proposed that the catalyst selectivity is improved when Pt ensembles are reduced by bimetallic particle formation or when Pt sites with low coordination are covered. However, the exact structure of the bimetallic surface ensemble has not been identified in these catalysts. As shown for the phase diagrams for Pd-In in Figure 2.1a, several intermetallic alloys are often possible in bimetallic nanoparticles. [21] Bimetallic nanoparticles, however, may not only form ordered alloy structures, but may also form, solid solutions or alloys without isolated active atoms. [17, 44] This work suggests that only one of the several possible intermetallic compound structures is formed in Pd-In catalysts. That structure has isolated Pd atoms, thus, is selective for alkane dehydrogenation reactions. A similar structure was observed for a β_1-PdZn dehydrogenation catalyst. [11] For both In and Zn promoters, although Pd is not generally thought as a potential alkane dehydrogenation, for Pd alloys where the active atoms are isolated, high olefin selectivity is possible. It is possible that the role of promoter atoms, Sn, Zn, Ga, and In, in Pt is formation of intermetallic alloys with isolated Pt sites. [14, 45-49]

2.5.3 Preferential Alloy Phase Formation

For this study, the In:Pd ratio varies from 0.2 to 2.0, covering the composition range of 6 different possible intermetallic compound phases according to the phase diagram (Figure 2.1a). [21] Nevertheless, the only alloy phase observed is the 1:1 cubic PdIn intermetallic compound with CsCl structure, suggesting preferential formation of this intermetallic phase. During catalyst synthesis, the reaction temperature is far from the melting point of Pd and relevant Pd-In IMCs, indicating that the IMC formation reaction is likely kinetically controlled rather than thermodynamically controlled. This means that for two intermetallic compound phases, both within the relevant composition range, though one may be thermodynamically more stable than the other, formation of the second phase from Pd metal precursor may be preferred due to its lower activation energy, or kinetic barrier. This kinetic barrier is dependent on the difference in the crystal structure of the product phase compared to the reactant phase. When the Pd-In catalysts were prepared, Pd is easily reduced at about 200°C, where InO_x is not reducible. Reduction of InO_x likely occurs at higher temperature on the surface of the Pd nanoparticles by surface dissociated H atoms. [18, 50] The reduced In then diffuses at higher temperature into the Pd nanoparticle from the surface, forming Pd-In IMC. Among all 6 possible Pd-In IMC phases (Figure 2.1b), [22-26] the PdIn 1:1 IMC in a cubic CsCl type structure is most similar in crystal structure to FCC Pd and would require the least rearrangement of Pd atoms, i.e. has the lowest kinetic barrier. Therefore, only this IMC structure formed in all Pd-In catalysts. Further rearrangement does not occur at the temperature of preparation or reaction.

This phenomenon has been observed in other catalysts where intermetallic compounds are known. [12, 18, 19] In almost all cases, the preferred IMCs are characteristic of similar close packed crystal structures to the parent noble metal. It has been reported that in Pd-Zn catalysts, the only IMC phase that form is a 1:1 β_1-PdZn intermetallic compound with the CuTi type structure (tetragonal, shortened in c axis compared to the CsCl type). [12] For Rh-In catalysts, only RhIn 1:1 IMC (in the same structure as PdIn: cubic, CsCl type) forms. [19] Even when the In:Rh is substantially lower than 1:1, the catalysts maintain a high symmetry RhIn structure (tetragonal, AuCu type) by increasing the c/a ratio from the original CsCl structure via lattice distortion but do not form another IMC with major rearrangement of Rh atoms, which also implies a kinetically-controlled reaction mechanism. Other examples include Pt-Sn catalysts with Pt_3Sn and PtSn as the only IMCs formed, [49, 51] and Pt-In catalysts with Pt_3In and $PtIn_2$ preferred. [18, 52] This kind

of diffusion, or kinetically controlled preferential phase formation phenomenon is well-known in metallurgy. [53, 54, 55]

2.6 Conclusions

Monometallic Pd and three Pd-In intermetallic compound (IMC) catalysts with different In loading have been synthesized, characterized and tested for ethane dehydrogenation. Addition of In greatly increases the olefin selectivity for ethane dehydrogenation by forming a PdIn 1:1 IMC (cubic, CsCl type structure) in the Pd-In catalysts. At low In loading, partial surface PdIn IMC is formed. With additional In, there is a complete PdIn surface IMC, and at high In loading fully formed PdIn IMC nanoparticles are present. Although there are several Pd-In IMC structures possible, only the cubic PdIn 1:1 IMC (with a CsCl structure type) is formed in all Pd-In catalysts. It is suggested this occurs by a kinetically controlled mechanism for solid state IMC formation. The PdIn 1:1 IMC is the structure with the lowest kinetic barrier for intermetallic alloy formation and requires the least rearrangement of atoms in the initially formed FCC Pd nanoparticle. In the cubic PdIn IMC structure, the first nearest neighbors of Pd atoms are In at 2.81 Å with the nearest Pd-Pd distance of 3.25 Å, ensuring isolation of the catalytically active Pd atoms. For catalysts with a PdIn IMC surface, the ethane dehydrogenation selectivity is near 100%; while that of Pd nanoparticles of similar size is approximately 50 %. The geometric isolation of the active sites allows for catalytic reaction of structure insensitive reactions, i.e., dehydrogenation, while elimination of hydrogenolysis, a structure sensitive reaction. Concomitant Pd-In bond formation also modifies the electronic properties of Pd atoms, leading to an increase in the TOR by almost 10 times compared with monometallic Pd.

2.7 Acknowledgements

The authors gratefully acknowledge the financial support provided by the School of Chemical Engineering, Purdue University and a Kirk Endowment Exploratory Research Recharge Grant and use of Electron Microscopy facility at Birck Nanotechnology Center, Purdue University. Use of the Advanced Photon Source was supported by the U.S. Department of Energy, Office of Basic Energy Sciences, under contract no. DE-AC02-06CH11357. MRCAT operations, beamline 10-BM, are supported by the Department of Energy and the MRCAT member institutions. The

authors also acknowledge the use of beamline 11-ID-C. We thank Yanran Cui for experimental assistance on CO chemisorption analysis and Atish Parekh together with Arthur Shih for experimental assistance on AAS analysis.

2.8 References

1. J. J. Siirola, AIChE Journal, 2014, 60, 810-819.
2. J. J. Sattler, J. Ruiz-Martinez, E. Santillan-Jimenez and B. M. Weckhuysen, Chemical reviews, 2014, 114, 10613-10653.
3. R. Cortright and J. Dumesic, Journal of Catalysis, 1994, 148, 771-778.
4. S. de Miguel, A. Castro, O. Scelza, J. L. G. Fierro and J. Soria, Catalysis letters, 1996, 36, 201-206.
5. V. Galvita, G. Siddiqi, P. Sun and A. T. Bell, Journal of Catalysis, 2010, 271, 209-219.
6. L. Nykänen and K. Honkala, ACS Catalysis, 2013, 3, 3026-3030.
7. J. Shen, J. M. Hill, R. M. Watwe, B. E. Spiewak and J. A. Dumesic, The Journal of Physical Chemistry B, 1999, 103, 3923-3934.
8. M.-L. Yang, Y.-A. Zhu, X.-G. Zhou, Z.-J. Sui and D. Chen, ACS Catalysis, 2012, 2, 1247-1258.
9. M. Natal-Santiago, S. Podkolzin, R. Cortright and J. Dumesic, Catalysis letters, 1997, 45, 155-163.
10. A. Virnovskaia, S. Morandi, E. Rytter, G. Ghiotti and U. Olsbye, The Journal of Physical Chemistry C, 2007, 111, 14732-14742.
11. D. J. Childers, N. M. Schweitzer, S. M. K. Shahari, R. M. Rioux, J. T. Miller and R. J. Meyer, Journal of Catalysis, 2014, 318, 75-84.
12. J. R. Gallagher, D. J. Childers, H. Zhao, R. E. Winans, R. J. Meyer and J. T. Miller, Physical Chemistry Chemical Physics, 2015, 17, 28144-28153.
13. F. B. Passos, D. A. Aranda and M. Schmal, Journal of Catalysis, 1998, 178, 478-488.
14. P. Sun, G. Siddiqi, W. C. Vining, M. Chi and A. T. Bell, Journal of Catalysis, 2011, 282, 165-174.
15. J. Wu, Z. Peng, P. Sun and A. T. Bell, Applied Catalysis A: General, 2014, 470, 208-214.
16. T. B. Massalski, H. Okamoto, P. Subramanian, L. Kacprzak and W. W. Scott, Binary alloy phase diagrams, American Society for Metals Metals Park, OH, 1986.
17. M. Armbrüster, R. Schlögl and Y. Grin, Science and Technology of Advanced Materials, 2014, 15, 1-17.
18. N. Iwasa and N. Takezawa, Topics in Catalysis, 2003, 22, 215-224.

19. T. Takanashi, M. Tamura, Y. Nakagawa and K. Tomishige, RSC Advances, 2014, 4, 28664-28672.
20. C. Li, Y. Chen, S. Zhang, S. Xu, J. Zhou, F. Wang, M. Wei, D. G. Evans and X. Duan, Chemistry of Materials, 2013, 25, 3888-3896.
21. H. Okamoto, ASM International, Member/Customer Service Center, Materials Park, OH 44073-0002, USA, 2000. 828, 2000.
22. I. Harris, M. Norman and A. Bryant, Journal of the Less Common Metals, 1968, 16, 427-440.
23. U. Häussermann, M. Elding-Pontén, C. Svensson and S. Lidin, Chemistry–A European Journal, 1998, 4, 1007-1015.
24. E. Hellner and F. Laves, Zeitschrift für Naturforschung A, 1947, 2, 177-184.
25. H. Kohlmann and C. Ritter, Zeitschrift für anorganische und allgemeine Chemie, 2009, 635, 1573-1579.
26. H. Kohlmanna and C. Ritter, Zeitschrift für Naturforschung B, 2007, 62, 929-934.
27. J. R. Gallagher, T. Li, H. Zhao, J. Liu, Y. Lei, X. Zhang, Y. Ren, J. W. Elam, R. J. Meyer and R. E. Winans, Catalysis Science & Technology, 2014, 4, 3053-3063.
28. E. M. Fiordaliso, I. Sharafutdinov, H. W. Carvalho, J.-D. Grunwaldt, T. W. Hansen, I. Chorkendorff, J. B. Wagner and C. D. Damsgaard, ACS Catalysis, 2015, 5, 5827-5836.
29. C. A. Schneider, W. S. Rasband and K. W. Eliceiri, Nat methods, 2012, 9, 671-675.
30. N. Koryabkina, A. Phatak, W. Ruettinger, R. Farrauto and F. Ribeiro, Journal of Catalysis, 2003, 217, 233-239.
31. T. Ressler, Journal of synchrotron radiation, 1998, 5, 118-122.
32. A. Hammersley, S. Svensson, M. Hanfland, A. Fitch and D. Hausermann, International Journal of High Pressure Research, 1996, 14, 235-248.
33. L. Lutterotti, S. Matthies and H. Wenk, IUCr: Newsletter of the CPD, 1999, 21.
34. R. Eischens, S. Francis and W. Pliskin, The Journal of Physical Chemistry, 1956, 60, 194-201.
35. M. Skotak, Z. Karpiński, W. Juszczyk, J. Pielaszek, L. Kępiński, D. Kazachkin, V. Kovalchuk and J. d'Itri, Journal of Catalysis, 2004, 227, 11-25.

36. T. Lear, R. Marshall, J. A. Lopez-Sanchez, S. D. Jackson, T. M. Klapötke, M. Bäumer, G. Rupprechter, H.-J. Freund and D. Lennon, The Journal of chemical physics, 2005, 123, 174706.
37. J. Lu, B. Fu, M. C. Kung, G. Xiao, J. W. Elam, H. H. Kung and P. C. Stair, Science, 2012, 335, 1205-1208.
38. K. Wolter, O. Seiferth, H. Kuhlenbeck, M. Bäumer and H.-J. Freund, Surface Science, 1998, 399, 190-198.
39. D. B. Buchholz, Q. Ma, D. Alducin, A. Ponce, M. Jose-Yacaman, R. Khanal, J. E. Medvedeva and R. P. Chang, Chemistry of Materials, 2014, 26, 5401-5411.
40. M. W. Tew, H. Emerich and J. A. van Bokhoven, The Journal of Physical Chemistry C, 2011, 115, 8457-8465.
41. K. Föttinger, J. A. van Bokhoven, M. Nachtegaal and G. n. Rupprechter, The Journal of Physical Chemistry Letters, 2011, 2, 428-433.
42. N. Schweitzer, H. Xin, E. Nikolla, J. T. Miller and S. Linic, Topics in Catalysis, 2010, 53, 348-356.
43. F. B. Passos, M. Schmal and M. Vannice, Journal of Catalysis, 1996, 160, 118-124.
44. H. Lorenz, C. Rameshan, T. Bielz, N. Memmel, W. Stadlmayr, L. Mayr, Q. Zhao, S. Soisuwan, B. Klötzer and S. Penner, ChemCatChem, 2013, 5, 1273-1285.
45. S. B. Kogan, N. R. Bursian, B. V. Pantusov, A. M. Moroz and D. S. Orlov, U.S. Patent, 4078743, 1978.
46. J. L. Robbins, E. Marucchi-Soos, J. W. Johnson and J. F. Brody, U.S. Patent, 5346871, 1995.
47. Y. Zhou and S. M. Davis, U.S. Patent, 5219816, 1993.
48. G. Siddiqi, P. Sun, V. Galvita and A. T. Bell, Journal of Catalysis, 2010, 274, 200-206.
49. J. Wu, Z. Peng and A. T. Bell, Journal of Catalysis, 2014, 311, 161-168.
50. Y. Uemura, Y. Inada, Y. Niwa, M. Kimura, K. K. Bando, A. Yagishita, Y. Iwasawa and M. Nomura, Physical Chemistry Chemical Physics, 2012, 14, 2152-2158.
51. R. Srinivasan and B. H. Davis, Platinum Metals Review, 1992, 36, 151-163.
52. N. Iwasa, T. Mayanagi, N. Ogawa, K. Sakata and N. Takezawa, Catalysis letters, 1998, 54, 119-123.
53. R. E. Reed-Hill and R. Abbaschian, 1973.

54. Q. Chen, N. Ma, K. Wu and Y. Wang, Scripta Materialia, 2004, 50, 471-476.

55. S. Wang and M. Starink, International Materials Reviews, 2005, 50, 193-215.

CHAPTER 3. STRUCTURE AND REACTIVITY OF PT-IN INTERMETALLIC ALLOY NANOPARTICLES: HIGHLY SELECTIVE CATALSYTS FOR ETHANE DEHYDROGENATION

Wegener, E.C.; Wu, Z.; Tseng, H.; Gallagher, J.R.; Ren, Y.; Diaz, R.E.; Ribeiro, F.H.; Miller, J.T.; "Structure and reactivity of Pt-In intermetallic alloy nanoparticles: highly selective catalysts for ethane dehydrogenation," *Catalysis Today* 2018, 299, 146-153. Reproduced with permission by Elsevier, copyright 2018. DOI: 10.1016/j.cattod.2017.03.054

3.1 Abstract

The structure of silica supported Pt and Pt-In bimetallic catalysts with nominal In:Pt atomic ratios of 0.7 and 1.4 were determined by *in situ* synchrotron XAS and XRD. It was seen that the addition of In led to the formation of two different intermetallic alloy phases. At an In:Pt ratio of 0.7 the Pt_3In phase with a Cu_3Au structure was formed. When the ratio was increased to 1.4 a shell of $PtIn_2$ having a CaF_2 structure formed around a core of Pt_3In. The catalysts were tested for ethane dehydrogenation at 600 ^oC to determine the effect of alloying on ethylene selectivity and turnover rate (TOR). The monometallic Pt catalysts was 73% selective for ethylene and had an initial TOR of 0.7 s^{-1}. Both alloy catalysts were ≈100% selective for dehydrogenation and had higher initial TOR, 2.8 s^{-1} and 1.6 s^{-1} for In:Pt ratio of 0.7 and 1.4, respectively. The increase in selectivity is attributed to the elimination of large Pt ensembles resulting from geometric changes to the catalyst surface upon alloying. Electronic changes due to the formation of Pt-In bonds are thought to be responsible for the increases in TOR in the alloy catalysts.

3.2 Introduction

The past decade has brought tremendous growth in the production of natural gas resulting from advancements in drilling technologies which have allowed for the recovery of gases trapped in shale formations. This increase in supply has made natural gas a viable feedstock for the production of chemicals and fuels. While predominately methane, shale deposits can contain up to 20% ethane and propane. These plentiful alkane resources can be directly converted by catalytic

dehydrogenation to alkenes, valuable chemical building blocks. High purity products can be utilized in the polymer industry while mixtures can be converted to fuel range hydrocarbons. [1]

Catalyst selectivity for dehydrogenation over hydrogenolysis, the primary competing reaction pathway, is paramount in light alkane dehydrogenation (LAD) processes. Industrially, Pt is used for LAD due to its intrinsic nature of favoring C-H bond activation over C-C bond activation. [2] The addition of Sn as a promoter results in higher olefin selectivity and catalyst stability. [3-12] The promotional effects have been attributed to the formation of Pt-Sn alloys. [3, 10-12] Alloying can change the geometric and electronic properties of catalysts and both effects have been proposed to be the dominate factor responsible for improved selectivity and stability. For the geometric case it has been proposed that alloying with Sn eliminates large Pt ensembles responsible for hydrogenolysis and coke forming reactions while retaining catalytic activity for dehydrogenation. [3-5] The Pt_3Sn, PtSn, and $PtSn_2$ alloy phases have been identified in model Pt-Sn catalysts. However, because of the very small particles and low metal loadings the crystal phase of commercial catalysts has not been reported. [13-17] For the electronic case the formation of Pt-Sn bonds is thought to transfer electron density from Sn to Pt resulting in enhanced olefin desorption and improved selectivity. [17-20]

Recently Pd-Zn bimetallic catalysts have been shown to be highly selective for propane dehydrogenation. The addition of Zn to Pd catalysts led to the formation of a 1:1 intermetallic alloy with a AuCu structure and resulted in an increase in propylene selectivity from 10% for monometallic Pd to 98% for the alloy. [21,22] Similar results have been reported for bimetallic Pd-In catalysts used for ethane dehydrogenation. A 1:1 PdIn intermetallic alloy with a CsCl structure was formed which led to an increase in ethylene selectivity from 53% to 98%. [23] In both studies the increase in olefin selectivity was attributed to the formation of the 1:1 alloy phase in which the active Pd atoms are geometrically isolated by inactive Zn or In. These works demonstrate that selective LAD catalysts can be made through the formation of certain intermetallic alloy structures.

The addition of In to Pt catalysts has also been shown to increase olefin selectivity for LAD [24] and to reduce activity for hydrogenolysis. [25, 26] The changes in catalytic properties have been attributed to the formation of bimetallic Pt-In particles, but exact structures have not been determined. The binary phase diagram for Pt and In at 600 ^{o}C is shown in Figure 3.1.

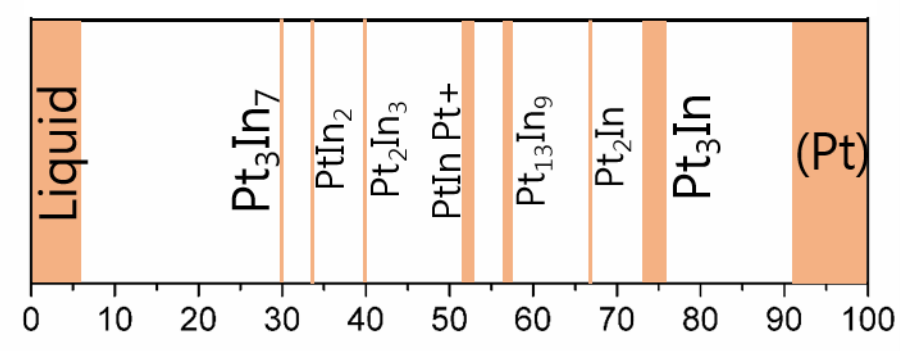

Figure 3.1: Binary Pt-In phase diagram at 600 °C adapted from Okamoto [27]

Pt and In can form seven intermetallic alloys. Unlike solid solutions where atoms occupy random lattice positions, atoms in intermetallic alloys sit in fixed sites which results in active sites with well-defined geometric and electronic properties. [28] Therefore, determination of the exact structure of bimetallic nanoparticles is crucial for understanding catalytic properties.

Here, we report on the synthesis, characterization, and catalytic performance of a monometallic Pt and two bimetallic Pt-In catalysts with different Pt:In atomic ratios supported on silica. The catalysts were characterized by CO chemisorption, scanning transmission electron microscopy (STEM), *in situ* X-ray absorption spectroscopy (XAS), and *in situ* X-ray diffraction (XRD). Ethane dehydrogenation was used to evaluate the effect of In on the olefin selectivity and reaction rate.

3.3 Experimental

3.3.1 Catalyst Synthesis

Pt-In bimetallic catalysts (target loadings of 4 wt. % Pt and 3 and 6 wt. % In) were synthesized by sequential incipient wetness impregnation. The required amount of $In(NO_3)_3 \cdot xH_2O$ (Sigma Aldrich) was dissolved in 8 mL of water. Citric acid (Sigma Aldrich) was added to the solution at a 3:1 molar ratio of citric acid to $In(NO_3)_3$. Approximately 5 mL of ammonium hydroxide solution (30%, Sigma Aldrich) was then added to the solution. Initially a white precipitate formed which dissolved upon further addition of ammonium hydroxide. The resulting solution (pH≈11) was added dropwise to 15 g of Silica (Davisil 636 silica gel, Sigma Aldrich, 480 m2/g surface area and 0.75 mL/g pore volume) with continuous stirring. The obtained catalysts

were dried overnight at 125 ºC and then calcined for 3 hr at 600 ºC. 0.48 g of $Pt(NH_3)_4(NO_3)_2$ was dissolved in a mixture of 3 mL of ammonium hydroxide solution and 3.5 mL of water. The resulting solution was added dropwise to 6 g of the In/SiO_2 precursor catalysts. The obtained catalysts were dried overnight at 125 ºC and calcined at 225 ºC for 3 hr. The Pt-In catalysts were reduced at 250 ºC for 30 min and then at 600 ºC for 30 min in 5% H_2/N_2 at 100 cc/min.

For comparison a 2 wt. % monometallic Pt catalyst was synthesized by the strong electrostatic adsorption method (SEA). 5g of silica was added to 50 mL of water. Ammonium hydroxide was added until the pH of the mixture was ≈11. 0.2 g of $Pt(NH_3)_4(NO_3)_2$ was dissolved in 25 mL of water and ammonium hydroxide solution was added until a pH ≈11. The Pt solution was added to the silica mixture with constant stirring. The obtained catalyst was filtered, washed with H_2O, filtered, and dried overnight at 125 ºC. The catalyst was calcined at 300 ºC for 3 hr followed by reduction at 250 ºC for 30 min and then 600 ºC for 30 min in 5% H_2/N_2 at 100 cc/min.

3.3.2 Atomic Absorption Spectroscopy

The indium content of the bimetallic catalysts after reduction at 600 ºC was determined by AAS using a PerkinElmer AAnalyst 300 spectrometer. 3 mL of aqua regia was added to approximately 40 mg of sample and left overnight to dissolve. The solutions were then diluted with H_2O to be within the linear detection range of the instrument. The instrument was calibrated using an In AAS standard obtained from Sigma Aldrich. Metal loadings were obtained from the average values of two sets of dissolved samples, which differed by less than 5%.

3.3.3 CO Chemisorption

Pt dispersions were measured by CO chemisorption using a Micromeritics ASAP 2020 chemisorption device. Approximately 0.1g of catalyst was placed in a U-shaped quartz reactor. Before measurements the catalysts were reduced at 600 ºC for 30 min in a flow of 5% H_2/He at 50 cc/min, cooled to 35 ºC under vacuum, and then held under vacuum for 30 min. Measurements were conducted at 35 ºC with the CO adsorption on Pt being determined from the difference between two repeat isotherms. A binding stoichiometry of 1:1 was assumed to calculate dispersion.

3.3.4 Scanning Transmission Electron Microscopy (STEM)

STEM images were acquired using the FEI Titan Scanning Transmission Electron Microscope (80-300 kV, 1 nm spatial resolution in STEM) at Birck Nanotechnology Center,

Purdue University. Catalysts samples were ground to a fine powder and dispersed in isopropyl alcohol. The solutions were added dropwise onto ultrathin Carbon film-Au TEM ready grids (TedPella) and the solvent evaporated on a hot plate. Images were taken using the high angle annular dark field (HAADF) detector at 300 kV. 200 particles were counted to determine the size distribution for each sample using the ImageJ program.

3.3.5 *In situ* X-ray Absorption Spectroscopy

XAS measurements at the Pt L_{III} edge (11.564 keV) and In K edge (27.940 keV) were taken at the bending magnet beamline of the Materials Research Collaborative Access Team (MR-CAT) at the Advanced Photon Source (APS), Argonne National Lab. Measurements were taken in step-scan transmission mode in about 10 min.

Samples were ground to a fine powder and pressed into a stainless-steel sample holder to form a self-supporting wafer. The sample holder was placed in a quartz tube with ports containing Kapton windows so samples could be treated prior to measurements. Samples were reduced in 100 cc/min of 3% H_2/He for 30 min at 600 ^oC. Following reduction, the samples were cooled to room temperature in 100 cc/min of He. Trace oxidants in He were removed by passing through a Matheson PUR-Gas Triple Purifier Cartridge. Spectra were obtained at room temperature in He. WINXAS 3.1 software [29] was used to fit XAS data. The EXAFS coordination parameters were obtained by a least-squares fit in R-space of the k^2-weighted Fourier transform data from 3.0 to 12.0 $Å^{-1}$. The first shell fit of the magnitude and imaginary parts were performed between 1.8 and 2.9 Å at the Pt L_{III} edge and between 1.5 and 3.2 Å at the In K edge. Fits were performed by refinement of coordination numbers (CN), bond distances (R), and energy shift (E_o). $\Delta\sigma^2$ was kept constant for each sample and CN and R were allowed to vary to determine the correct fit. Phase and amplitude fitting functions for Pt-Pt were determined from Pt foil (CN=12 at 2.77 Å) and FEFF calculations for Pt-In. [30]

3.3.6 *In situ* X-ray Diffraction

XRD measurements were performed at the 11-ID-C beam line at the APS, Argonne National Lab. Diffraction patterns were collected in transmission mode with a PerkinElmer large area detector using x-rays at 105.091 keV (λ=0.11798 Å). Samples were ground to a fine powder, pressed into a thin wafer, and loaded into a Linkam Thermal Stage. Prior to measurements the

stage was purged with Ar for 5 min at room temperature and then ramped to 600 ºC in 3% H_2/Ar at 50 cc/min. Diffraction patterns (the summation of 30 exposures of 5 seconds each) were collected after reduction at 600 ºC for 20 min. Samples were then cooled to room temperature in the same atmosphere and diffraction patterns collected. The empty sample stage and bare silica support were treated with the same procedure for background subtraction. The obtained 2-D diffraction patterns were integrated to 1-D intensity versus 2Θ plots using the Fit2D software. [31] MAUD (Materials Analysis Using Diffraction) was used to simulate theoretical diffraction patterns of potential Pt-In alloy phases which were used as standards to determine the crystal structure of each catalyst. [32]

3.3.7 Ethane Dehydrogenation Kinetics

Ethane dehydrogenation kinetics were measured using a quartz fixed-bed reactor with 3/8-in ID. A thermocouple was placed within a quartz thermocouple well positioned at the bottom center of the catalyst bed to measure the reaction temperature within the bed. Before testing the catalyst was reduced under 40 cc/min of 5% H_2/N_2 while the temperature was raised to 600 ºC where it was held for 30 min. Catalysts were compared under two sets of conditions. To compare catalyst selectivity for ethylene the catalysts were tested at an initial conversion of 15% under a reaction atmosphere of 5% C_2H_6, 6% H_2, 49.3% N_2, balanced in He at a total flow rate of 150 cc/min and 600 ºC. Turnover rates (TOR) were measured at 600 ºC under a reaction atmosphere of 5% C_2H_6, 2% H_2, 0.5% C_2H_4, 49.3% N_2, balanced in He at a total flow rate of 150 cc/min. The approach to equilibrium was considered for the calculation of TOR following the work of Koryabkina et al. [33] The rate expression used is,

$$rate = k_f[C_2H_6]^a[C_2H_4]^b[H_2]^c(1 - \beta);\ \beta = \frac{[C_2H_4][H_2]}{K[C_2H_6]}$$

where k_f is the forward rate constant, K is the equilibrium constant, and β is the approach to equilibrium. The value of β was found to be less than 0.17 for all reactions indicating the reactions were far from equilibrium. Apparent activation energies were measured at four temperatures between 570 and 600ºC once the catalysts had stabilized at conversions below 10%.

3.4 Results

3.4.1 Atomic Absorption Spectroscopy

After the bimetallic catalysts were initially reduced at 600 ^{o}C, a yellow residue was observed at the outlet of the reactor tube. The yellow color, characteristic of In_2O_3 and identical to the color of the calcined, In impregnated SiO_2, suggests the residue is a result of a loss of In oxide from the catalyst. The actual In:Pt ratios in the reduced bimetallic catalysts were determined by AAS and are reported in Table 3.1.

Table 3.1: AAS, CO Chemisorption, and STEM Results

Catalyst	Pt Loading (wt. %)	In Loading (wt. %)	In:Pt Atomic Ratio	Pt Dispersion (%)	Particle Size (nm)
Pt	2.0	/	/	29	3.5 ± 1.6
Pt-In(0.7)	4.0	1.7	0.7	13	3.0 ± 0.7
Pt-In(1.4)	4.0	3.2	1.4	9	3.4 ± 1.2

After high temperature reduction the In loadings of the two bimetallic catalysts were approximately half the nominal loading, resulting in catalysts with 1.7% and 3.2% In by weight. The two bimetallic catalysts were named for the reduced In:Pt atomic ratios determined from AAS, Pt-In(0.7) and Pt-In(1.4), respectively. The yellow residue was not seen after subsequent reductive pretreatments of the bimetallic catalysts indicating further loss of In was negligible.

3.4.2 Co Chemisorption and Scanning Transmission Electron Microscopy

CO chemisorption and STEM were used to determine platinum dispersions and particle size distributions of the three catalysts. The results are given in Table 3.1. The average particle size of the monometallic Pt catalyst is 3.5 nm, in agreement with what would be expected from the measured dispersion value of 29%. Pt-In(0.7) and Pt-In(1.4) were determined to have Pt dispersions of 13% and 9% respectively. The average particle sizes of the two bimetallic catalysts were found to be 3.0 nm and 3.4 nm, smaller than what would be expected from the measured dispersion values. The lower dispersion values for the bimetallic catalysts are likely from coverage of the nano-particle surface by a species which does not adsorb CO, for example metallic In.

3.4.3 *In situ* X-ray Absorption Spectroscopy

XAS measurements were conducted at the Pt L_{III} (11.564 keV) and In K (27.940 keV) edges to determine the local coordination environments of Pt and In and determine whether bimetallic nanoparticles were formed in the Pt-In catalysts. Spectra were collected at room temperature in He after reduction at 600 ^{o}C. Pt L_{III} edge XANES of the Pt and Pt-In catalysts are shown in Figure 3.2a and In K edge XANES of the Pt-In catalysts and an In_2O_3 reference are shown in Figure 3.2b.

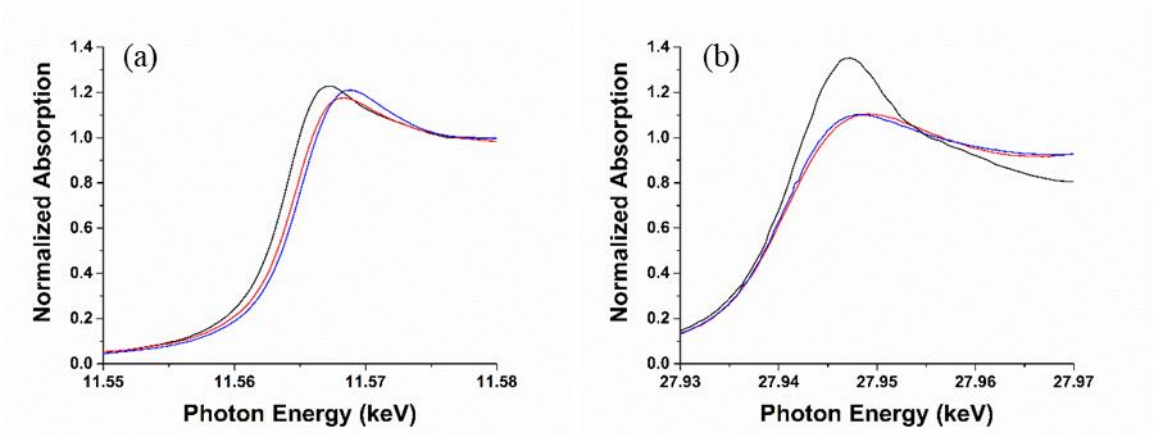

Figure 3.2: XANES spectra of catalysts reduced at 600^{o}C (a) Pt L_{III} Edge - Pt (black), Pt-In(0.7) (red), and Pt-In(1.4) (blue) and (b) In K Edge - In_2O_3 (black), Pt-In(0.7) (red), and Pt-In(1.4) (blue)

The XANES shape, white line intensity, and edge energy (11.5640 keV, Table 3.2) of the Pt catalyst are very similar to that of the Pt foil. The white line intensities of Pt-In(0.7) and Pt-In(1.4) are consistent with metallic Pt, but the edge energies have been shifter to higher energy, 11.5648 keV and 11.5651 keV, also given in Table 3.2. The change in the shape and energy of the XANES spectra of the Pt-In catalysts is consistent with the formation of bimetallic PtIn nanoparticles. Comparison of the Pt-In(0.7) and Pt-In(1.4) XANES spectra show differences in edge energy and position of the first peak in the white line suggesting the Pt in the two samples also have different coordination environments. The energy of the In XANES are 27.9402 keV, shifted to higher energy than metallic In (27.940 keV) and are given in Table 3.2. The decrease in the white line intensity of the spectra of the Pt-In catalysts compared to the In_2O_3 reference is indicative of a fraction of In being metallic. The Pt L_{III} and In K edge EXAFS of the catalysts after

reduction at 600 ºC are shown in Figure 3.3. The local structure, coordination numbers (CN) and bond distances (R), of the Pt and In were determined from the k^2-weighted first shell EXAFS spectra, and the results are in Table 3.2.

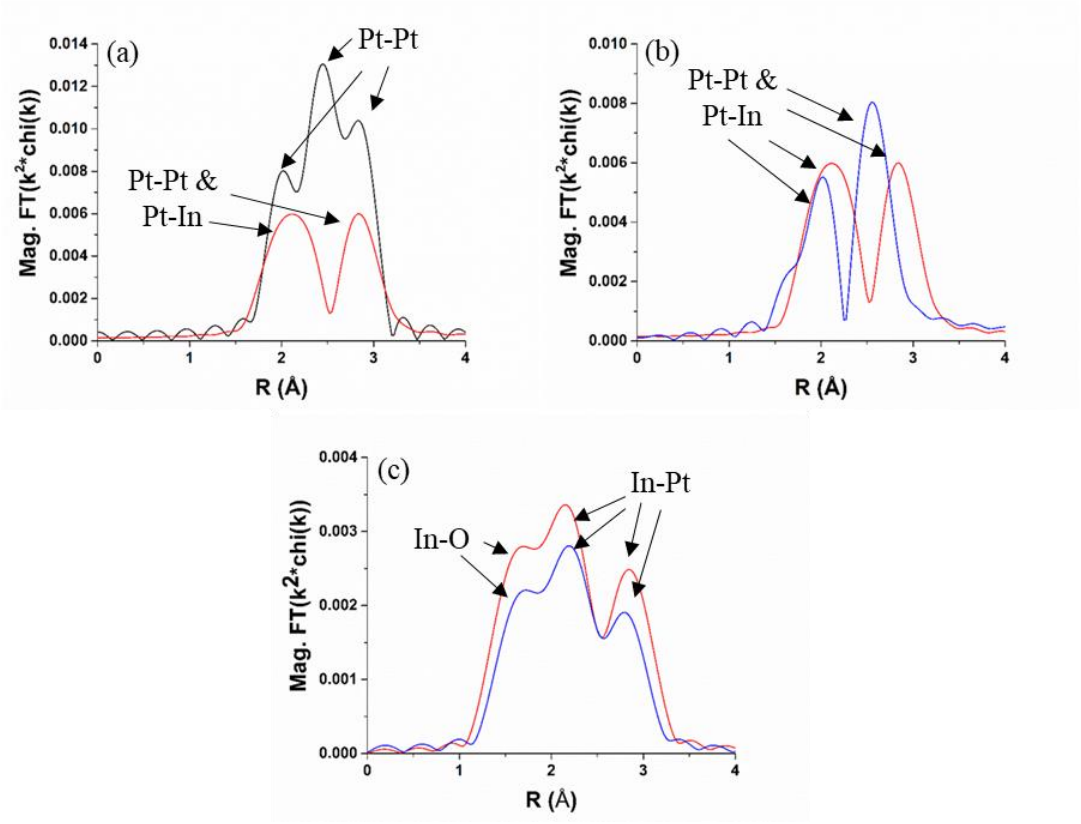

Figure 3.3: EXAFS spectra of catalysts reduced at 600ºC (a) Pt L_{III} Edge of – Pt (black) and Pt-In(0.7) (red), (b) Pt L_{III} Edge of – Pt-In(0.7) (red) and Pt-In(1.4) (blue), and (c) In K Edge of – Pt-In(0.7) (red) and Pt-In(1.4) (blue)

Table 3.2: XANES and EXAFS fitting parameters following reduction at 600 ºC

Catalyst	Edge	XANES Energy (keV)	Scattering Pair	CN	R (Å)	$\Delta\sigma^2 \times 10^3$	E_o (eV)
Pt	Pt	11.5640	Pt-Pt	8.4	2.76	2.0	-0.1
Pt-In(0.7)	Pt	11.5648	Pt-Pt	5.7	2.79	4.0	-6.0
			Pt-In	3.3	2.79	4.0	4.7
	In	27.9402	In-O	0.8	2.11	4.0	-8.2
			In-Pt	3.5	2.79	4.0	-1.2
Pt-In(1.4)	Pt	11.5651	Pt-Pt	4.4	2.79	4.0	-10.0
			Pt-In	5.1	2.74	4.0	2.9
	In	27.9402	In-O	0.7	2.14	4.0	-8.9
			In-Pt	2.9	2.74	4.0	-2.4
Pt Foil	Pt	11.5640	Pt-Pt	12	2.77	0.0	-0.1

The Pt-Pt CN of 8.4 at a distance of 2.76 Å for the monometallic Pt catalyst are typical of 3 nm Pt nanoparticles, in agreement with chemisorption and STEM results. [34] The Pt-In catalysts cannot be fit with only Pt-Pt scattering and a good fit was obtained by adding a contribution for Pt-In scattering. Pt-In(0.7) has a Pt-In CN of 3.3 and a Pt-Pt CN of 5.7. Both Pt-In and Pt-Pt are at a distance of 2.79 Å, the latter is slightly longer than the Pt-Pt bonds in the monometallic Pt catalyst. The Pt-In coordination number in Pt-In(1.4) is 5.1, larger than that in Pt-In(0.7). However, the Pt-In bond distance of 2.74 Å is shorter than that of Pt-In(0.7). The increase in Pt-In coordination was accompanied by a decrease in the Pt-Pt CN to 4.4, but at the same bond distance, 2.79 Å, as Pt-In(0.7).

At the In edge, the bimetallic catalysts show a set of two peaks between 2-3 Å (phase uncorrected distance), typical of metal-metal scattering, and a shoulder around 1.8 Å (phase uncorrected distance), typical of In-O scattering. Pt-In(0.7) has an In-O CN of 0.8 at a distance of 2.11 Å and an In-Pt CN of 3.5 at a distance of 2.79 Å. Similar values of In-O CN and bond distance, 0.7 and 2.14 Å respectively, were present in Pt-In(1.4). Pt-In(1.4) was found to have a In-Pt CN of 2.9 at a distance of 2.74 Å, fewer In-Pt bonds at a shorter distance compared to Pt-In(0.7). The In-O scattering seen in both catalysts is a result of unreduced indium oxide on the catalyst. The In-O coordination numbers of 0.8 and 0.7 for Pt-In(0.7) and Pt-In(1.4) are lower than the In-O coordination number of 6 in bulk In_2O_3 and it can be estimated that approximately 90% of the In in each catalyst has been incorporated into the bimetallic particles. The In-O bond distances are in agreement with what has been reported for amorphous In_2O_3. [35] No evidence of In-In scattering was seen in the EXAFS of either bimetallic catalyst. From XAS it is evident that bimetallic

nanoparticles are formed in both Pt-In catalysts. However, XAS provides local structural information and does not determine whether a specific alloy phase or a disordered structure is formed.

3.4.4 *In situ* X-ray Diffraction

To determine if the bimetallic Pt-In particles formed an ordered structure, in-situ synchrotron XRD measurements were performed. Due to their small size a high fraction of the atoms are at the surface and are oxidized in air. Therefore, to obtain meaningful structural information the data has to be collected *in situ*. [36] Diffraction patterns were collected at 600 ^{o}C after reduction and then after cooling to room temperature. Aside from peak displacement due to thermally induced lattice expansion, the diffraction patterns were identical indicating the same crystal structure present at 600 ^{o}C and room temperature. To identify the phases present, the room temperature spectra were compared to simulated diffraction patterns of known Pt-In alloys. The diffraction pattern of the isolated nanoparticles in each catalyst and the simulated pattern of the identified phases are shown in Figure 3.4. The patterns were obtained by subtracting the scattering due to the silica support, the empty cell, and gases present in the X-ray path from the full diffraction patterns. The energy of the synchrotron X-rays was 105.091 keV, much higher than Cu Kα radiation (8.0463 keV) which is typically used in lab-based instruments. Thus, the diffraction peaks occur at much lower angles in the synchrotron XRD patterns. The weak and broad diffraction peaks result from the low metal loading and small size of the nanoparticles.

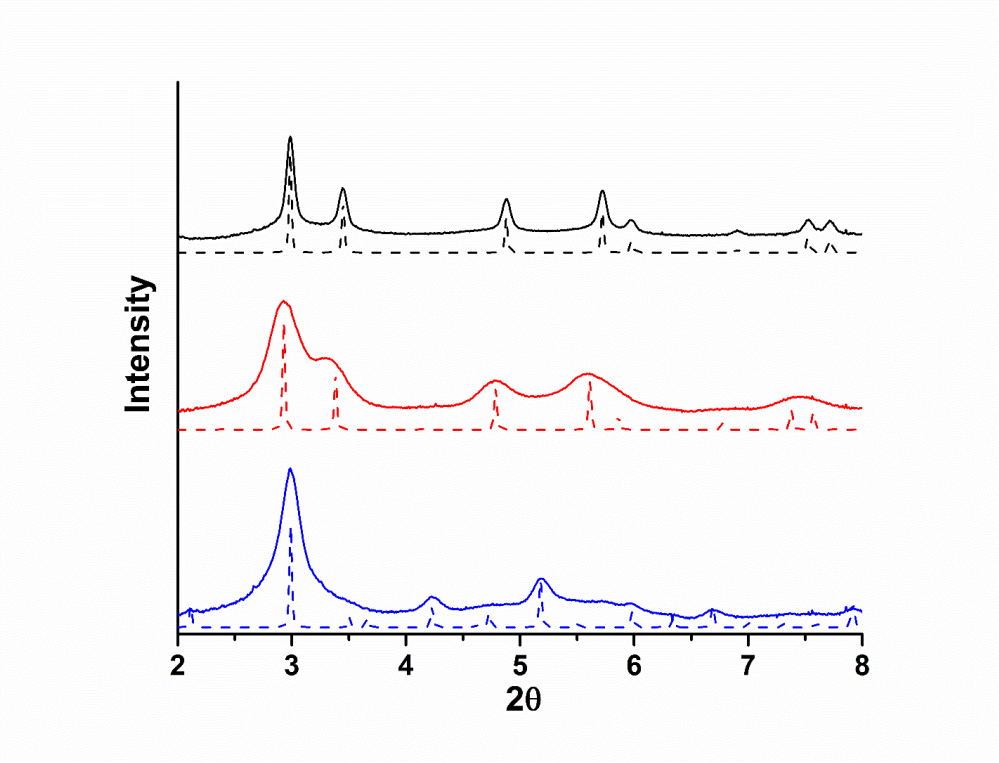

Figure 3.4: Background subtracted XRD patterns of catalysts following reduction at 600°C (Pt (black), Pt-In(0.7) (red), and Pt-In(1.4) (blue)) and simulated spectra of identified phases (Pt (black dashed), Pt_3In (red dashed), and $PtIn_2$ (blue dashed)).

The diffraction pattern from the monometallic catalyst is characteristic of FCC Pt with peaks from the (111) and (200) reflections at 2.99° and 3.45°. The average lattice parameter calculated from Bragg's law and the position of the (111) and (200) reflections is 3.92 Å which corresponds to a Pt-Pt bond distance of 2.77 Å and is consistent with EXAFS results. Pt-In(0.7) has a diffraction pattern similar to FCC Pt, however, all the peaks are shifted to lower angles indicating an increase in the size of the unit cell. The diffraction pattern of Pt-In(0.7) matches that of the Pt_3In alloy with a Cu_3Au structure with the most intense peaks at 2.93° and 3.33° corresponding to the (111) and (200) reflections. The diffraction pattern of Pt-In(1.4) is distinctly different from the other two catalysts. There is one main peak in the diffraction pattern centered at 2.99° which has been identified as the (220) reflection of the $PtIn_2$ alloy with a CaF_2 structure. However, all the peaks present are shifted to lower angle by 0.01°-0.02°, indicating a larger unit cell than the ideal structure.

3.4.5 Ethane Dehydrogenation Kinetics

Initial turnover rates and selectivity of ethane dehydrogenation were determined at 600 ^{o}C at 15% conversion using a reaction mixture of 5% ethane and 6% H_2 balanced in inert. The results are given in Table 3.3. Selectivity was calculated from the observed gas phase products (ethylene from dehydrogenation and methane from hydrogenolysis) The small amount of coke on the catalyst was not included. Alloy formation led to increased ethylene selectivity and stability. The Pt catalyst was 73% selective for ethylene and deactivated after one hour to a constant conversion of 9% with selectivity improving to 91% as the catalyst deactivated. Pt-In(0.7) and Pt-In(1.4) exhibited high ethylene selectivities of 99% and 98% with little deactivation in 5 hr. The In impregnated silica was tested under the same conditions and showed negligible conversion.

Table 3.3: Catalytic results for ethane dehydrogenation reactions

	$C_2H_6 + H_2$		$C_2H_6 + C_2H_4 + H_2$		
Catalyst	Initial Selectivity	Initial TOR* (s^{-1})	Initial TOR* (s^{-1})	Steady State TOR* (s^{-1})	E_{app} (kJ/mol)
Pt	73%	1.8	0.7	0.2	76
Pt-In(0.7)	99%	5.3	2.8	1.0	95
Pt-In(1.4)	98%	1.9	1.6	1.0	137

* Per mole of surface Pt as measured by CO chemisorption

Turnover rates (TOR) and apparent activation energies (E_{app}) were determined with a reaction gas of 0.5% ethylene with 5% ethane and 2% H_2. Results are also shown in Table 3.3. The initial TOR and steady state TOR were higher on the alloy catalysts than the monometallic Pt catalyst. The initial TOR of the Pt catalyst was 0.7 s^{-1} and deactivated to a steady-state value of 0.2 s^{-1}. Pt-In(0.7) had the highest initial TOR of the three catalysts, 2.8 s^{-1}, while Pt-In(1.4) had an initial TOR of 1.6 s^{-1}. The Pt-In catalysts had equivalent steady state TOR of 1.0 s^{-1}. The addition of ethylene to the feed decreased the initial TOR's of Pt and Pt-In(0.7) while the TOR of Pt-In(1.4) was almost unchanged. Alloy formation also led to increases in the apparent activation energy. The addition of In led to an increase in E_{app} from 76 kJ/mol for Pt to 95 kJ/mol for Pt-In(0.7) and 137 kJ/mol for Pt-In(1.4). The increase in TOR and higher E_{app} in the Pt-In catalysts are consistent with an electronic promotion of Pt by In. Differences in the TOR and E_{app}'s of the two Pt-In

catalysts also suggests that there is a different In promotional effect due to the different Pt-In alloy structures.

3.5 Discussion

The addition of In to the Pt catalyst led to the formation of multiple Pt-In intermetallic alloy phases. The catalyst synthesized with a bulk In:Pt atomic ratio of 0.7 formed the Pt_3In phase with a Cu_3Au structure. Pt_3In has the same structure as the Pt_3Sn alloy which has been reported for Pt-Sn bimetallic catalysts. [14-17] The Pt-In and Pt-Pt bond distances of 2.79 Å seen by EXAFS is in agreement with the bond distances in the ideal Pt_3In structure of 2.82 Å. Increasing the In:Pt ratio to 1.4 led to the formation of a second alloy phase, $PtIn_2$ with a CaF_2 structure. $PtSn_2$ alloys of equivalent structure have been reported to be selective for alkane dehydrogenation. [13, 14] The Pt-In bond distance in the ideal $PtIn_2$ structure is 2.76 Å, similar to the distance seen by EXAFS, 2.74 Å. However, there is still Pt-Pt scattering in the EXAFS spectra of the Pt-In(1.4) catalysts. In the ideal $PtIn_2$ structure Pt has only In first nearest neighbors; therefore, the Pt-Pt scattering indicates a second phase is also present. The AAS results provide further evidence since the measured In:Pt ratio is 1.4, less than the minimum ratio necessary to form a complete alloy of the correct stoichiometric ratio of 2:1. The Pt-Pt bond distance determined by EXAFS is 2.79 Å, the same as was seen in the Pt-In(0.7) catalyst indicating the second phase present is likely Pt_3In. It has been reported for Pd-Zn intermetallic alloy catalysts that alloy formation occurs first on the surface of Pd nanoparticles and progresses towards the center suggesting that the promoter metal diffuses into the Pd nanoparticles as more ZnO is reduced to metal at higher temperatures. [21, 22] Based on these observations it is likely that for the Pt-In(1.4) catalyst as more In_2O_3 is reduced it forms a shell of $PtIn_2$ around a core of Pt_3In. Figure 3.5 shows the evolution of nanoparticle structure with increasing In:Pt ratio and the unit cells of the alloy phases identified.

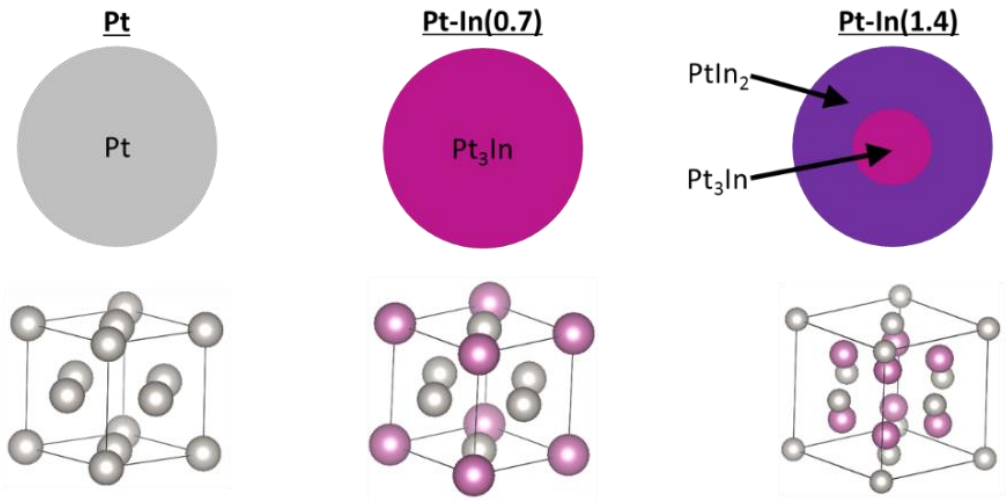

Figure 3.5: Schematic of geometric structure of Pt and Pt-In catalysts and crystal structures of the active phase [37, 38]

Initial addition of In leads to the formation of the Pt_3In phase and continued addition leads to the formation of the $PtIn_2$ phase at the surface of the Pt_3In nanoparticles. Due to the limiting amount of In present in the Pt-In(1.4) catalyst, a shell of $PtIn_2$ is formed around a core of the Pt_3In phase.

The alloy phases formed in the Pt-In catalysts have different stoichiometry's and structures than those which have been reported to form in highly selective Pd-Zn and Pd-In dehydrogenation catalysts, which both form alloys with atomic ratios of 1:1 having a AuCu and a CsCl structure, respectively. [21-23] While the bulk phase diagrams show multiple intermetallic alloy phases over the composition ranges studied, only the 1:1 alloys were formed in the Pd-Zn and Pd-In catalysts. [39, 40] For Pd-In it was also proposed that alloy formation was kinetically controlled and that the 1:1 alloy was selectively formed due to its similar crystal structure to FCC Pd. Similar phenomena occurs in the Pt-In catalysts. The structures of the Pt-In intermetallic alloys that were not formed in the Pt-In catalysts are shown in Figure 3.6.

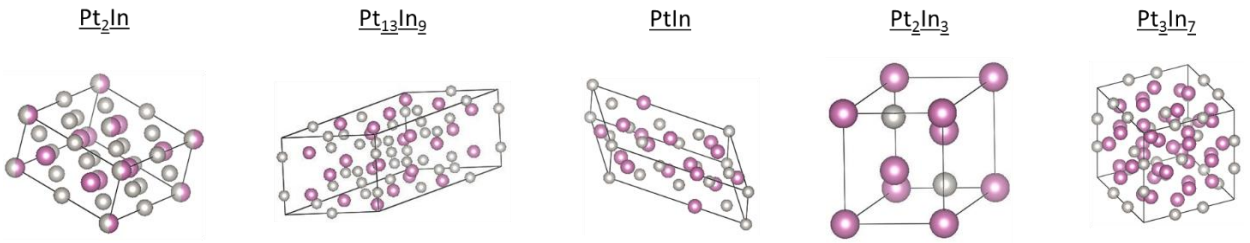

Figure 3.6: Crystal structures of Pt-In intermetallic alloys not formed in the Pt-In catalysts [41-45]

The phases formed, Pt_3In and $PtIn_2$, have crystal structures which can be formed by minimal rearrangement of the Pt atoms in the initially reduced FCC structure. The structures in Figure 3.6 require significant reordering of the Pt and In atoms and are not formed. The observed structures suggest that alloy formation is kinetically, rather than thermodynamically controlled, consistent with previous studies on PdZn and PdIn bimetallic nanoparticles. Thus, all compositionally possible structures are not formed.

Although the 1:1 alloys were the only phases formed in the PdZn and PdIn catalysts, the structure of equivalent stoichiometry was not observed in the present work. The unit cell of the PdZn 1:1 alloy is body-centered tetragonal while that of PdIn is body-centered cubic, both similar in structure to FCC Pd. As seen in Figure 3.6, the 1:1 PtIn alloy has a monoclinic unit cell very different in structure from FCC Pt. This large difference in crystal structure is believed to be responsible for the 1:1 PtIn phase not forming even though alloys with the same stoichiometry were formed in the PdZn and PdIn bimetallic catalysts.

The observed changes in crystal structure coincide with changes in the ethane dehydrogenation performance of each catalyst. The monometallic Pt catalyst exhibited a moderate selectivity of 73% at 15% conversion and deactivated quickly, behavior typical of Pt catalysts. [3, 22] Ethylene selectivities of nearly 100% were achieved over the alloy catalysts which also showed more stable performance than monometallic Pt. Alloy formation also increased dehydrogenation TORs. The Pt_3In phase present in Pt-In(0.7) had the highest initial TOR of the three catalysts, almost 4 times that of the monometallic Pt catalyst. Increased In content and formation of the $PtIn_2$ phase in Pt-In(1.4) resulted in a lower initial TOR than Pt-In(0.7), but still higher than that measured for Pt. Similar behavior was seen by Sun et al, where bimetallic Pt-In nanoparticles were confirmed by EXAFS; however the exact structure was not determined. It was reported that the

addition of In and formation of bimetallic particles increased the ethylene selectivity from 60% for monometallic Pt to greater than 96% for all the Pt-In catalysts. The TOR increased from 0.7 s^{-1} for Pt with increasing In:Pt ratios before reaching a maximum of 1.6 s^{-1} at a ratio of 1.7 and decreasing to 0.5 s^{-1} with further addition of In. [24] Pt-In(0.7) and Pt-In(1.4) had equivalent steady state TOR, approximately five times that of monometallic Pt.

The increase in selectivity for dehydrogenation of the alloy catalysts compared to the monometallic catalyst can be attributed to the elimination of large Pt ensembles upon alloy formation, i.e. a geometric effect. Dehydrogenation is a structure insensitive reaction requiring a single active atom [46, 47] while hydrogenolysis is a structure sensitive reaction requiring an ensemble of active atoms. [47] It has been shown that Pt 3-fold hollow sites present in large Pt ensembles are responsible for the formation of strongly adsorbed alkylidyne species which are precursors of hydrogenolysis and coke forming reactions. [48-51] The formation of Pt_3In reduces the number of Pt 3-fold hollow sites and it has been shown that the formation of ethylidyne is suppressed on Pt_3Sn alloys with equivalent structures to the Pt_3In phase in Pt-In(0.7). [48,50,51] While the number of Pt 3-fold hollow sites is reduced, they are not completely eliminated, and trimers of Pt atoms are still present in the alloy structure. However, the Pt-Pt bond distance of 2.82Å is slightly elongated from 2.77Å, the Pt-Pt bond distance in FCC Pt. It has been proposed that two adjacent active atoms are required for hydrogenolysis reactions. [52-54] Although Pt-In(0.7) contains three adjacent Pt atoms it is highly selective for dehydrogenation suggesting that C-C bond cleavage requires ensembles of more than three active atoms. In the $PtIn_2$ phase, catalytic Pt atoms are geometrically isolated by inactive In atoms which completely eliminates Pt 3-fold hollow sites necessary for ethylidyne formation. Although the bulk stoichiometry and structure are different, the local coordination environment of Pt in $PtIn_2$ is equivalent to Pd in the 1:1 PdZn and PdIn alloys where high dehydrogenation selectivity was attributed to the isolation of Pd atoms by the inactive metal. [21-23] Accordingly, the isolated Pt atoms in Pt-In(1.4) are highly selective for dehydrogenation reactions.

Accompanying the geometric changes of alloy formation are concomitant electronic changes to Pt which are likely responsible for the increases seen in the TORs and E_{app} of the Pt-In catalysts. XPS and XANES studies on bimetallic Pt-Sn catalysts have shown that the electronic properties of Pt are altered by interactions with Sn. The binding energy of Pt $4f_{7/2}$ electrons as measured by XPS has been reported to decrease while the Pt L_{III} XANES energy has been reported

to increase. [20,55] It has been proposed that these changes are due to a d → s, p rehybridization that occurs upon formation of Pt-Sn bonds resulting in a decrease in the occupancy of the Pt 5d orbitals. [20,55-57] However, this would yield no change in the XANES energy and an increase in the white line intensity.

For the bimetallic catalysts the Pt L_{III} XANES energy increases and the white line intensity decreases. The increase in XANES energy indicates an upward shift in the unfilled valance states of Pt while the decrease in the white line intensity suggests higher occupancy of the 5d orbitals. Molecular Orbital (MO) Theory would predict that the formation of Pt-In bonds would result in new filled bonding and unfilled anti-bonding state in Pt. A shift to higher energy in the PtIn XANES spectra suggests that the energy of the empty 5d orbitals are at higher energy compared to Pt. From MO Theory, this also implies Pt-In bond formation results in the filled 5d orbitals in Pt being lower in energy. A shift to lower energy would result in less hybridization of the 5d with the 6s and 6p orbitals leading to higher electron density in the 5d states and a decrease in the white line intensity. The effects of rehybridization on white line intensity is well documented for changes in size of metal clusters. [34, 58-60] Changes in the 5d states likely modify the adsorption of reactants and products leading to changes in catalytic performance. Electronic changes are also evident from the increases in the apparent activation energy, a convolution of heat of adsorption and intrinsic activation energy, seen for the Pt-In catalysts. Experimental and theoretical results on Pt-Sn surfaces have shown that alloy formation reduces the binding strengths of alkenes to Pt. [3,4,51] It is possible that the formation of Pt-In alloys leads to weaker adsorption of alkenes, resulting in faster ethylene desorption and promoting dehydrogenation TORs, similar to what has been proposed for Pt-Sn catalysts.

3.6 Conclusions

The addition of In to Pt catalysts leads to the formation of intermetallic alloy nanoparticles. At an In:Pt atomic ratio of 0.7 the Pt_3In phase with a Cu_3Au structure formed. A shell of $PtIn_2$ with a CaF_2 structure forms around a core of Pt_3In when the In:Pt ratio is increased to 1.4. The Pt_3In and $PtIn_2$ alloys are structurally similar to FCC Pt and their formation requires minimal atomic rearrangement when compared to phases not observed suggesting alloy formation is kinetically controlled. When compared to a monometallic Pt catalyst the intermetallic alloys exhibited superior performance for ethane dehydrogenation, i.e. higher ethylene selectivity and turnover

rates. The increase in selectivity to nearly 100% can be attributed to geometric changes to the catalytic Pt atoms. Ensembles responsible for structure sensitive hydrogenolysis reactions are eliminated upon alloy formation; while structure insensitive dehydrogenation, which requires a single active site, is unaffected. The increases in TOR are likely due to electronic changes to Pt arising from the formation of Pt-In bonds. Further studies are necessary to fully understand the electronic properties of Pt intermetallic alloy nanoparticles. This work shows that it is possible to tailor both the geometric and electronic properties of catalysts by synthesizing intermetallic alloy nanoparticles of different stoichiometry's and structures.

3.7 Acknowledgements

Financial support was provided by the Davidson School of Chemical Engineering, Purdue University. The authors acknowledge the use of the Electron Microscopy facility at Birck Nanotechnology Center, Purdue University, support for which was provided by a Kirk Endowment Exploratory Research Recharge Grant. Use of the Advanced Photon Source was supported by the U.S. Department of Energy, Office of Basic Energy Sciences, under contract no. DE-AC02-06CH11357. MRCAT operations are supported by the Department of Energy and MRCAT member institutions. The authors acknowledge the use of the 10-BM and 11-ID-C beamlines at the APS.

3.8 References

1. J. J. Siirola, AIChE Journal, 2014, 60, 810-819
2. J. J. Sattler, J. Ruiz-Martinez, E. Santillan-Jimenez, B. M. Weckhuysen, Chemical Reviews, 2014, 114, 10613-10653
3. R. D. Cortright, J. A. Dumesic, Journal of Catalysis, 1994, 148, 771-778
4. R. D. Cortright, J. M. Hill, J. A. Dumesic, Catalysis Today, 2000, 55, 213-223
5. V. Galvita, G. Siddiqi, P. Sun, A. T. Bell, Journal of Catalysis, 2010, 271, 209-219
6. D. Sanfilippo, I. Miracca, Catalysis Today, 2006, 111, 133-139
7. D. Akporiaye, S. F. Jensen, U. Olsbye, F. Rohr, E. Rytter, M. Rønnekleiv, A. I. Spjelkavik, Industrial & Engineering Chemistry Research, 2001, 40, 4741-4748
8. O. A. Bariås, A. Holmen, E. A. Blekkan, Journal of Catalysis, 1996, 158, 1-12
9. A. Virnovskaia, S. Morandi, E. Rytter, G. Ghiotti, U. Olsbye, Journal of Physical Chemistry C, 2007, 111, 14732-14742
10. L. Bednarova, C. E. Lyman, E. Rytter, A. Holman, Journal of Catalysis, 2002, 211, 335-346
11. N. Nava, P. Del Angel, J. Salmones, E. Baggio-Saitovitch, P. Santiago, Applied Surface Science, 2007, 253, 9215-9220
12. J. Llorca, N. Homs, J. León, J. Sales, J. L. G. Fierro, P. Ramirez de la Piscina, Applied Catalysis A: General, 1999, 189, 77-86
13. J. Llorca, N. Homs, J. L. G. Fierro, J. Sales, P. Ramirez de la Piscina, Journal of Catalysis, 1997, 166, 44-52
14. B. K. Vu, M. B. Song, I. Y. Ahn, Y. Suh, D. J. Suh, W. Kim, H. Koh, Y. G. Choi, E. W. Shin, Catalysis Today, 2011, 164, 214-220
15. L. Deng, T. Shishido, K. Teramura, T. Tanaka, Catalysis Today, 2014, 232, 33-39
16. R. Srinivasan, R. Sharma, S. Su, B. Davis, Catalysis Today, 1994, 21, 83-99
17. L. Deng, H. Miura, T. Shishido, S. Hosokawa, K. Teramura, T. Tanaka, ChemCatChem, 2014, 6, 2680-2691
18. M. Yang, Y. Zhu, X. Zhou, Z. Sui, D. Chen, ACS Catalysis, 2012, 2, 1247-1258
19. J. Ruiz-Martínez, A. Sepúlveda-Escribano, J. A. Anderson, F. Rodríguez-Reinoso, Catalysis Today, 2007, 123, 235-244

20. G. J. Siri, J. M. Ramallo-López, M. L. Casella, J. L. G. Fierro, F. G. Requejo, O. A. Ferretti, Applied Catalysis A: General, 2005, 278, 239-249
21. D. J. Childers, N. M. Schweitzer, S. Mehdi Kamali Shahari, R. M. Rioux, J. T. Miller, R. J. Meyer, Journal of Catalysis, 2014, 318, 75-84
22. J. R. Gallagher, D. J. Childers, H. Zhao, R. E. Winans, R. J. Meyer, J. T. Miller, Physical Chemistry Chemical Physics, 2015, 17, 28144-28153
23. Z. Wu, E. C. Wegener, H. Tseng, J. R. Gallagher, J. W. Harris, R. E. Diaz, Y. Ren, F. H. Ribeiro, J. T. Miller, Catalysis Science and Technology, 2016, 6, 6965-6976
24. P. Sun, G. Siddiq, W. C. Vining, M. Chi, A. T. Bell, Journal of Catalysis, 2011, 282, 165-174
25. P. Mériaudeau, C. Naccache, A. Thangaraj, C. L. Bianchi, R. Carli, S. Narayanan, Journal of Catalysis, 1995, 152, 313-321
26. P. Mériaudeau, A. Thangaraj, J. F. Dutel, P. Gelin, C. Naccache, Journal of Catalysis, 1996, 163, 338-345
27. H. Okamoto, Journal of Phase Equilibria and Diffusion, 2005, 26, 399
28. M. Armbrüster, R. Schlögl, Y. Grin, Science and Technology of Advanced Materials, 2014, 15, 1-17
29. T. Ressler, Journal of Synchrotron Radiation, 1998, 5, 118-122
30. J. J. Rehr, R. C. Albers, Reviews if Modern Physics, 2000, 72, 621-654
31. A. Hammersley, S. Svensson, M. Hanfland, A. Fitch, D. Hausermann, International Journal of High Pressure Research, 1996, 14, 235-248
32. L. Lutterotti, S. Matthies, H. Wenk, IUCr: Newsletter of the CPD, 1999, 21
33. N. A. Koryabkina, A. A. Phatak, W. F. Ruettinger, R. J. Farrauto, F. H. Ribeiro, Journal of Catalysis, 2003, 217, 233-239
34. J. T. Miller, A. J. Kropf, Y. Zha, J. R. Regalbuto, L. Delannoy, C. Louis, E. Bus, J. A. van Bokhoven, Journal of Catalysis, 2006, 240, 222-234
35. D. B. Buchholz, Q. Ma, D. Alducin, A. Ponce, M. Jose-Yacaman, R. Khanal, J. E. Medvedeva, R. P. H. Chang, Chemistry of Materials, 2014, 26, 5401-5411
36. J. R. Gallagher, T. Li, H. Zhao, J. Liu, Y. Lei, X. Zhang, Y. Ren, J. W. Elam, R. J. Meyer, R. E. Winans, J. T. Miller, Catalysis Science and Technology, 2014, 4, 3053-3063
37. H. E. Swanson, E. Tatge, National Bureau of Standards (U.S.), 1953, 539, 95

38. Z. Yu, Acto Geologica Sinica, 1997, 71, 480-485
39. H. Okamoto, Binary Alloy Phase Diagrams, II Edition, Editor T. B. Massalski, 1990, 3, 3068-3070
40. H. Okamoto, Journal of Phase Equilibria, 2003, 24, 481
41. S. Bhan, K. Schubert, Journal of the Less-Common Metals, 1969, 17, 73-90
42. M. Ellner, S. Bhan, K. Schubert, Journal of the Less-Common Metals, 1969, 19, 245-252
43. S. Heinrich, K. Schubert, Journal of the Less-Common Metals, 1978, 57, 1-7
44. K. C. Jain, S. Bhan, Transaction of the Indian Institute of Metals, 1972, 25, 100-102
45. H. A. Friedrch, J. Koehler, Zeitschrift fuer Kristallographie – New Crystal Structures, 2002, 217, 24
46. P. Biloen, F. M. Dautzenberg, W. M. H. Sachtler, Journal of Catalysis, 1977, 50, 77-86
47. M. Boudart, Journal of Molecular Catalysis, 1985, 30, 27-38
48. Y. Tsai, B. E. Koel, Journal of Physical Chemistry B, 1997, 101, 2895-2906
49. Z. Nomikou, M. A. Van Hove, G. A. Somorjai, Langmuir, 1996, 12, 1251-1256
50. J. Shen, J. M. Hill, R. M. Watwe, B. E. Spiewak, J. A. Dumesic, Journal of Physical Chemistry B, 1999, 103, 3923-3934
51. R. M. Watwe, R. D. Cortright, M. Mavrikakis, J. K. Nørskov, J. A. Dumesic, Journal of Chemical Physics, 2000, 114, 4663-4668
52. S. A. Goddard, M. D. Amiridis, J. E. Rekoske, N. Cardona-Martinez, J. A. Dumesic, Journal of Catalysis, 1989, 117, 155-169
53. G. A. Martin, Journal of Catalysis, 1979, 60, 345-355
54. D. W. Flaherty, E. Iglesia, Journal of the American Chemical Society, 2013, 135, 18586-18599
55. J. M. Ramallo-López, G. F. Santori, L. Giovanetti, M. L. Casella, O. A. Ferretti, F. G. Requejo, Journal of Physical Chemistry B, 2003, 107, 11441-11451
56. J. A. Rodriguez, S. Chaturvedi, T. Jirsak, J. Hrbek, Journal of Chemical Physics, 1998, 109, 4052-4062
57. J. A. Rodriguez, T. Jirsak, S. Chaturvedi, J. Hrbek, Journal of the American Chemical Society, 1998, 120, 11149-11157

58. M. G. Mason, Physical Review B, 1983, 27, 748-762

59. L. F. Mattheiss, R. E. Dietz, Physical Review B, 1980, 22, 1663-1676

60. P. K. Jain, Structural Chemistry, 2005, 16, 421-426

CHAPTER 4. ZINC PROMOTION OF PLATINUM FOR CATALYTIC LIGHT ALKANE DEHDROGENATION: INSIGHTS INTO GEOMETRIC AND ELECTRONIC EFFECTS

Reproduced with permission from Cybulskis, V.J.; Bukowski, B.C.; Tseng, H.; Gallagher, J.R.; Wu, Z.; Wegener, E.C.; Kropf, A.J.; Ravel, B.; Ribeiro, F.H.; Greeley, J.; Miller, J.T.; "Zinc Promotion of Platinum for Catalytic Light Alkane Dehydrogenation: Insights into Geometric and Electronic Effects," *ACS Catal*. 2017, 7, 4173-4181. Copyright 2017 American Chemical Society. DOI: 10.1021/acscatal.6b03603

4.1 Abstract

Supported metal nanoparticles are vital as heterogeneous catalysts in the chemical transformation of hydrocarbon resources. The catalytic properties of these materials are governed by the surface electronic structure and valence orbitals at the active metal site and can be selectively tuned with promoters or by alloying. Through an integrated approach using density functional theory (DFT), kinetics, and *in situ* X-ray spectroscopies, we demonstrate how Zn addition to Pt/SiO_2 forms high symmetry Pt_1Zn_1 nanoparticle alloys with isolated Pt surface sites that enable near 100% C_2H_4 selectivity during ethane dehydrogenation (EDH) with a six-fold higher turnover rate (TOR) per mole of surface Pt at 600 °C compared to monometallic Pt/SiO_2. Furthermore, we show how DFT calculations accurately reproduce the resonant inelastic X-ray spectroscopic (RIXS) signatures of Pt 5*d* valence orbitals in the Pt/SiO_2 and $PtZn/SiO_2$ catalysts that correlate with their kinetic performance during EDH. This technique reveals that Zn modifies the energy of the Pt 5*d* elections in PtZn, which directly relates to TOR promotion, while ensemble effects from the incorporation of Zn into the catalyst surface lead to enhanced product selectivity.

4.2 Introduction

The recent surge in gas production from shale formations throughout the United States presents a tremendous opportunity to develop catalytic innovations that efficiently transform hydrocarbon resources (i.e., methane, ethane, propane, butanes) directly into value-added chemicals and fuels with reduced environmental impact by selectively activating paraffinic C-H

bonds. [1] Although various routes to synthesize alkene and aromatic building block molecules over metal-containing catalysts by dehydrogenation [2] and cyclization [3], respectively, have been well-studied, fundamental understanding of issues regarding long-term catalyst stability, product selectivity, and turnover rates (TOR) still remain problematic. [4-5] Many of the challenges associated with developing new materials to overcome these limitations can only be addressed at the molecular level.

Noble metals, such as Pt, are well-known for exceptional performance in hydrocarbon catalysis, particularly for hydrogenation and isomerization reactions, due to their affinity for paraffinic C-H bonds. [2] Since the reactivity of metal nanoparticle surfaces is determined by the electronic states through the valence *d*-bands, which is a region in the partial density of states (DOS) [6, 7], one way we may alter the electronic structure of these surfaces, and hence, their reactivity, is by alloying of the surface with various promoters that can influence the availability and energies of the valence electrons to form chemical bonds with adsorbates. For example, the addition of Zn or Sn to Pt-containing catalysts has led to improved alkene selectivity during alkane dehydrogenation. [8-10] It has been suggested that these ad-metals modify the electronic properties of the noble metal sites by donating electron density and weakening the adsorption of π-bonded alkenes; thus, inhibiting the formation of coke precursors. [10-13] Yet, the energy levels of the *d* states of Pt and Pt-containing alloys, which also direct bond formation, have seldom been directly measured experimentally.

While structure-insensitive reactions, such as alkene hydrogenation and alkane dehydrogenation can occur on isolated Pt sites, it has been shown that larger Pt ensembles catalyze structure-sensitive reactions, including cracking and hydrogenolysis. [14-18] Recent experimental work by Childers et al. [19] has also shown that Zn addition to supported Pd catalysts can enhance propylene selectivity during propane dehydrogenation (PDH). The improved catalyst stability is attributed to the formation of a PdZn alloy with isolated Pd surface sites that eliminate the structure-sensitive hydrogenolysis pathway. [20] Similar conclusions regarding the importance of active site isolation (i.e., geometric effects) have been reported for SiO_2-supported PdIn [21] and PtIn [22] intermetallic alloys during ethane dehydrogenation (EDH).

Experimentally, the electronic structure of metal nanoparticles on heterogeneous catalysts can be accessed by using *L* edge, resonant inelastic X-ray scattering (RIXS) to monitor the energy of the *d*-band filled and unfilled states. [23-25] As a hard X-ray, two-photon process, RIXS permits

the elucidation of electron excitations between inner-shell and valence levels within a specific element under working reaction conditions, thus making it possible to directly probe the surface chemistry at metal active sites and map the entire *d*-band spectrum to identify electronic descriptors of catalytic activity. As shown for the Pt L_3 edge in Figure 4.1, absorption of a photon with energy Ω promotes a 2*p* electron to an unoccupied state in the 5*d* valence shell and leaves behind a core hole that is subsequently refilled by an electron from filled orbitals. Filling of the core hole results in an emitted photon whose energy is dependent on the energy of the filled orbital. With a high-energy resolution spectrometer, the energy (ω) of the fluorescent photon from the filled 5*d* orbital can be determined (e.g., Pt $L\beta_5$ transition). The difference in energy between Ω and ω represents the overall energy transfer of the system (ΔE).

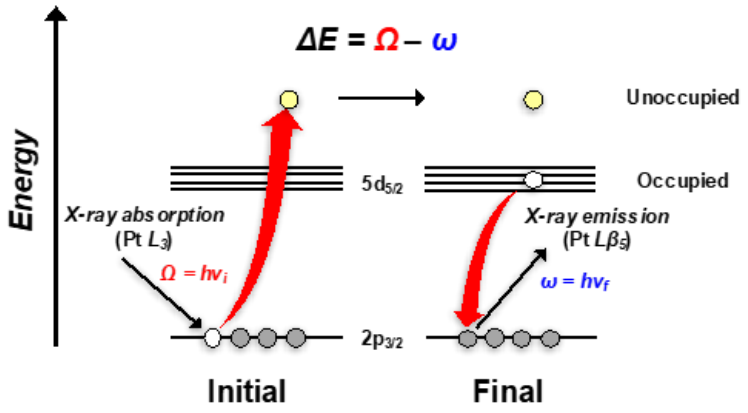

Figure 4.1: RIXS Energy Scheme for Pt 2p ↔ 5d Transitions

Many of the valence-to-core X-ray emission studies to date have been focused on the *K* edge ($s \rightarrow p$) for inorganic and bioinorganic metal complexes to examine metal-to-ligand charge transfer as well as changes in bonding and anti-bonding states. [26] However, the *K* edge cannot access chemical information on the valence *d* electrons that are relevant for catalysis. While RIXS has successfully been applied at the *L* edge for 3*d* and 4*d* transition metal complexes to examine crystal field splitting and orbital occupancy [27-29], there are relatively few studies on 5*d* metals [24, 30, 31], such as Pt, that examine the electronic structure of supported noble metal nanoparticles.

Here, by using *in situ* X-ray absorption and synchrotron X-ray diffraction, we show that Pt_1Zn_1 intermetallic alloy nanoparticles are preferentially formed from Pt and Zn precursors on an amorphous SiO_2 support. These bimetallic alloy catalysts contain isolated surface Pt atoms with only metallic Zn nearest neighbors and display high ethylene selectivity (~100%) during EDH at 600 °C. We also show how the capabilities of RIXS analysis can provide a unique fingerprint for the catalytic properties of Pt/SiO_2 and $PtZn/SiO_2$ dehydrogenation catalysts. This spectroscopic characterization of metal nanoparticle electronic valence states can be coupled with kinetic measurements of catalytic performance to describe how Zn addition to Pt/SiO_2 modifies the metal nanoparticle electronic structure to affect the EDH TOR. Lastly, we suggest that DFT RIXS calculations for Pt-containing alloy compositions provide additional electronic structural information; thereby, complementing and strengthening existing *d*-band models.

4.3 Results and Discussion

4.3.1 Ethane Dehydrogenation on Pt/SiO_2 and $PtZn/SiO_2$

The Pt/SiO_2 and $PtZn/SiO_2$ catalysts for this study were prepared by pH-controlled incipient wetness impregnation (pH-IWI) of high-purity SiO_2 with $(NH_3)_4Pt(NO_3)_2$ and $Zn(NO_3)_2{\cdot}6H_2O$ precursors to obtain 9.70 wt.% Pt for Pt/SiO_2, and 9.28 wt.% Zn and 9.53 wt.% Pt for $PtZn/SiO_2$. A high Pt loading was required in order to obtain sufficient signal-to-noise during *in situ* RIXS experiments due to the relatively weak intensity of the valence $5d_{5/2} \rightarrow 2p_{3/2}$ ($L\beta_5$) X-ray emission line for Pt. Pt dispersions based on the measured H_2 uptake (Table B.1) on the freshly-reduced Pt/SiO_2 and $PtZn/SiO_2$ catalysts were determined to be 27% and 44%, respectively. Catalyst testing was performed at 600 °C in a gas mixture of 2.5% C_2H_6, 1% H_2, and 0.5% C_2H_4 to achieve differential C_2H_6 conversion ($X < 0.1$) and allow the reaction rate to be treated as constant throughout the reactor (Appendix B).

As shown in Figure 4.1(a), the EDH TOR, normalized per surface Pt atom, for Pt/SiO_2 (blue closed circles) stabilized at 0.01 s^{-1} after 5 h on stream from a starting value of 0.05 s^{-1}. During this period, the C_2H_4 selectivity reached 96% ($X = 0.09$) from a starting value of 74% ($X = 0.4$) as shown in Figure 4.1(b) (blue closed circles). Following the catalyst stabilization, the apparent activation energy between 570 °C and 600 °C was determined to be 72±4 kJ $mole^{-1}$ (Fig. B.1). At the start of the run, the carbon mass balance closed at 83%, indicating significant coke deposition on the clean

catalyst surface, and then ultimately reached 100% after the stabilization period. This result, along with observed CH_4 formation during the reaction, shows that C_2H_6 hydrogenolysis and C_2H_4 decomposition reactions occur concomitantly with dehydrogenation on Pt. For $PtZn/SiO_2$, the EDH TOR per surface Pt was a factor of six higher than on Pt/SiO_2, as indicated by the red closed squares in Figure 4.2(a), and reached 0.06 s^{-1} after 12 h from a starting value of 0.2 s^{-1}. Throughout the stabilization period, the C_2H_4 selectivity (Figure 4.2(b)) and carbon mass balance both remained near 100% to indicate that dehydrogenation occurs almost exclusively on PtZn. The measured apparent activation energy for $PtZn/SiO_2$ was 99±5 kJ $mole^{-1}$ (Fig. B.1) and is similar to the 102 kJ $mole^{-1}$ result reported by Galvita et al. [17] for PtSn/Mg(Al)O. Metal cluster size distributions on the used Pt/SiO_2 and $PtZn/SiO_2$ samples after EDH at 600 °C were analyzed from HAADF-STEM and TEM images and determined to be 3.3±1.9 nm and 2.5±0.6 nm, respectively (Figs. B.2 – B.4).

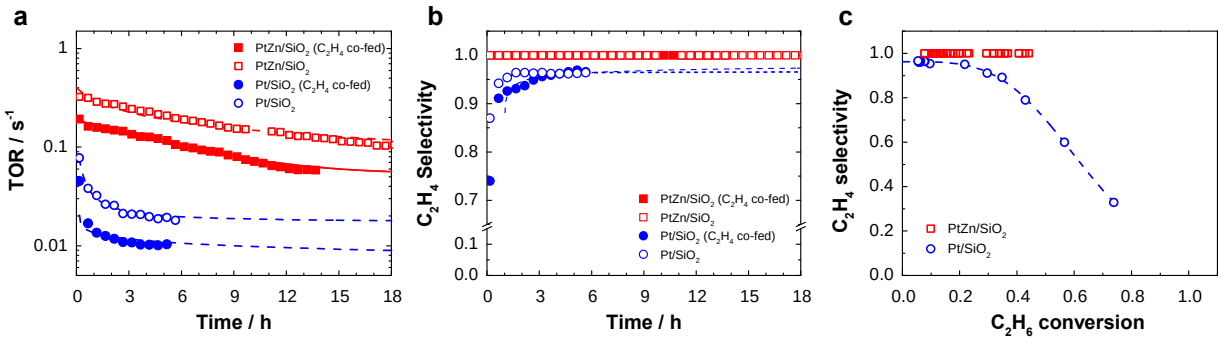

Figure 4.2: Ethane dehydrogenation kinetics for Pt/SiO_2 and $PtZn/SiO_2$. (a) TOR as a function of time on stream during EDH (2.5% C_2H_6, 1% H_2, 0.5% C_2H_4) at 600 °C on 9.70 wt.% Pt/SiO_2 with C_2H_4 co-fed (blue closed circles), 9.70 wt.% Pt/SiO_2 without C_2H_4 co-fed (blue open circles), 9.53 wt.% Pt – 9.28 wt.% Zn/SiO_2 with C_2H_4 co-fed (red closed squares), and 9.53 wt.% Pt – 9.28 wt.% Zn/SiO_2 without C_2H_4 co-fed (red open squares). (b) C_2H_4 selectivities as a function of time on stream during EDH at 600 °C. (c) C_2H_4 selectivities as a function of C_2H_6 conversion during EDH (2.5% C_2H_6, 1% H_2) at 600 °C for 9.70 wt.% Pt/SiO_2 (blue open circles) and 9.53 wt.% Pt – 9.28 wt.% Zn/SiO_2 (red open squares).

When C_2H_4 was removed from the reaction feed stream (Figure 4.2(a)), the TOR for both Pt/SiO_2 (blue open circles) and $PtZn/SiO_2$ (red open squares) increased by a factor of two, which indicates that C_2H_4 inhibits the EDH reaction by competing with C_2H_6 for Pt surface sites. As

shown in Figure 4.2(b), the C_2H_4 selectivities for both Pt/SiO_2 and $PtZn/SiO_2$ were comparable to EDH with C_2H_4 co-fed in the reaction mixture. At low C_2H_6 conversion ($X < 0.1$) the C_2H_4 selectivity on Pt/SiO_2 was similar to $PtZn/SiO_2$, but decreased to less than 50% at conversions above the equilibrium limit for dehydrogenation ($X_{eq} = 0.54$) as concomitant C-C bond cleavage reactions became dominant (Figure 4.2(c)). Conversely, $PtZn/SiO_2$ was able to maintain near 100% selectivity to C_2H_4 up to the thermodynamically-limited equilibrium conversion, indicating that the active Pt surface sites are able to suppress cracking and hydrogenolysis reactions, even with H_2 (produced during EDH) present in the reactor.

4.3.2 Geometric Structures of Pt and PtZn Nanoparticles

The Pt and PtZn nanoparticle structures were determined by using *in situ* X-ray absorption spectroscopy (XAS) and synchrotron X-ray diffraction (XRD). The X-ray absorption near edge structure (XANES) at the Pt L_3 edge ($E = 11{,}564$ eV) shows that the supported Pt nanoparticles on Pt/SiO_2 were metallic (Pt^0), as evidenced by the similar edge positons (defined as the inflection point in the first derivative of the experimental XANES spectrum) and white-line intensities between the Pt foil and the Pt/SiO_2 catalyst (Fig. B.5). The Pt atoms in $PtZn/SiO_2$ were also metallic and the edge energy increased as a result of Zn addition by 0.9 eV compared to Pt/SiO_2. Although the shape of the Pt L_3 XANES for metallic nanoparticles below approximately 3 nm in diameter exhibits slight differences compared to that for Pt foil, the edge energy is not changed. [32] Thus, changes in the edge energy can only be attributed to the formation of bimetallic PtZn nanoparticles. The *in situ* extended X-ray absorption fine structure (EXAFS) spectrum (black open circles) and fit of the isolated first scattering shell for 9.70 wt.% Pt/SiO_2 (blue dashed line) in the top half of Figure 4.3(a) revealed that the metallic Pt nanoparticles on Pt/SiO_2 are structurally similar to the bulk Pt foil (black open triangles) and that each Pt atom was surrounded by an average of 8.9±0.9 Pt nearest neighbors at a bond distance of 2.76±0.01 Å. Based on the metal dispersion correlation reported by Miller et al. [33], the average Pt cluster size on Pt/SiO_2 was 4.2±1.1 nm, consistent with the 3.3±1.9 nm cluster size distribution from HAADF-STEM and TEM images of the used catalyst after EDH (Fig. B.2 and B.4(a)).

For $PtZn/SiO_2$, each Pt atom was surrounded by an average of approximately 7 Zn nearest neighbors (7.1±0.6) at a bond distance of 2.62±0.01 Å as shown by the first shell fit in the bottom half for Fig. 4.3(a) (red dashed line). A Pt-Pt contribution was also fit in $PtZn/SiO_2$ with a

coordination number of 3.6±0.3 at an average bond distance of 2.81±0.02 Å as shown by the first shell fit in the bottom half for Fig. 4.3(a) (blue dashed line). This Pt-Pt distance is longer than that in monometallic Pt (i.e., at a non-bonding distance) and indicates that the Pt atoms in the PtZn nanoparticles were geometrically isolated from one another. Individual fitting parameters for the Pt foil, Pt/SiO_2, and $PtZn/SiO_2$ samples can be found in Table B.2.

The synchrotron XRD pattern for Pt/SiO_2 at room temperature further confirms that the Pt nanoparticles were metallic, as indicated by the agreement between the peak positions of the simulated Pt metal pattern (red line) and the data (black line) in Fig. 4.3(b). The Pt/SiO_2 diffraction peaks were broadened due to the small (3.3±1.9 nm by HAADF-STEM and TEM) nanoparticle size. In order to isolate these structural features, background scattering due to the SiO_2 support and empty heating stage were subtracted from the patterns for the Pt/SiO_2 and $PtZn/SiO_2$ catalysts according to the method described by Gallagher et al. [34]. The background-subtracted patterns taken at 600 °C (Fig. B.6) were found to be identical to those obtained at room temperature (Fig. 4.3(b)) except for shifts in diffraction peaks due to thermal lattice expansion, thereby indicating that the crystal structures of the Pt and PtZn nanoparticles remained unchanged throughout this temperature range. Thus, the diffraction patterns collected at room temperature were used for comparison with standard patterns simulated under the same conditions.

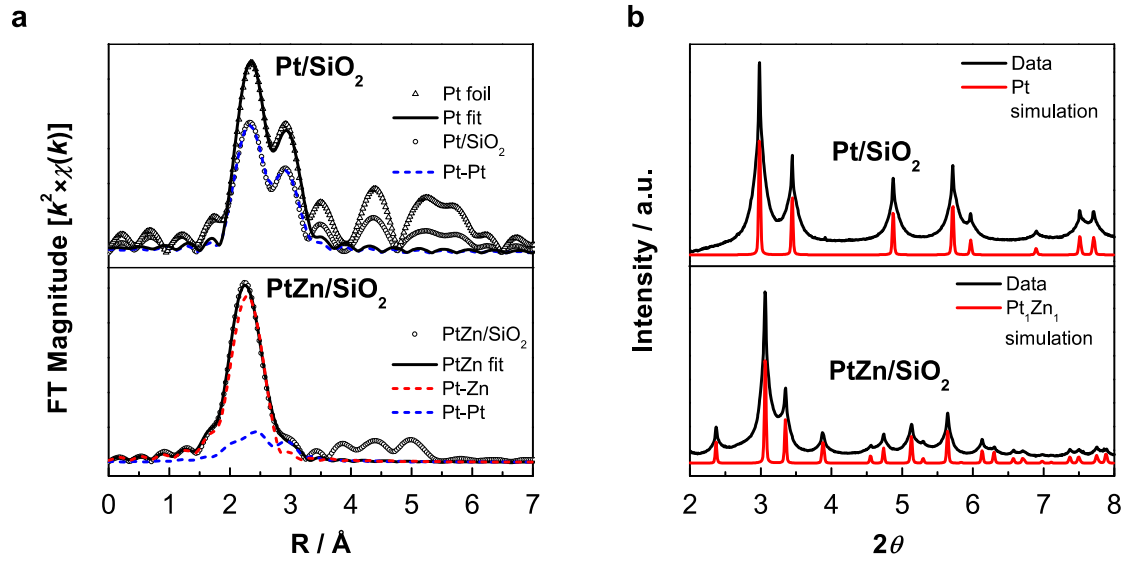

c

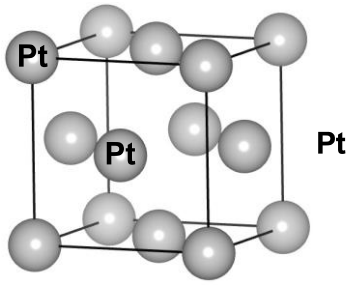

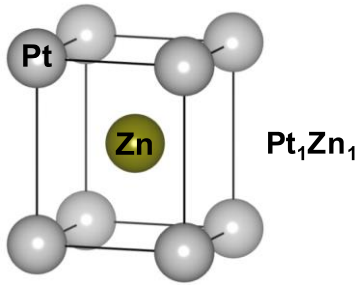

Method	$R_{Pt\text{-}Pt}$ / Å
EXAFS	2.76±0.01
XRD	2.78±0.01

Method	$R_{Pt\text{-}Zn}$ / Å	$R_{Pt\text{-}Pt}$ / Å
EXAFS	2.63±0.01	2.81±0.02
XRD	2.66±0.01	2.84±0.01

Figure 4.3: Structural characterization of Pt and PtZn nanoparticles. (a) *In situ* EXAFS at the Pt L_3 edge and isolated first scattering shell fits for 9.70 wt.% Pt/SiO_2 and 9.53 wt.% Pt – 9.28 wt.% Zn/SiO_2 obtained at room temperature after H_2 reduction at 600 °C. (b) *In situ* XRD patterns obtained for 9.70 wt.% Pt/SiO_2 and 9.53 wt.% Pt – 9.28 wt.% Zn/SiO_2 at room temperature and compared to simulated patterns for Pt and Pt_1Zn_1, respectively. (c) Structures of Pt and Pt_1Zn_1 intermetallic alloy along with bond distances from *in situ* EXAFS simulation of *in situ* XRD patterns for 9.70 wt.% Pt/SiO_2 and 9.53 wt.% Pt – 9.28 wt.% Zn/SiO_2 at room temperature.

PtZn nanoparticles on the $PtZn/SiO_2$ sample (black line) in Fig. 4.3(b) show diffraction peaks attributed to a Pt_1Zn_1, 1:1 intermetallic alloy phase (red line) with a tetragonal AuCu structure. No additional PtZn alloy phases (i.e., Pt_3Zn, Pt_3Zn_{10}, $PtZn_{1.7}$) were observed on the $PtZn/SiO_2$ catalyst, thereby indicating that the high symmetry Pt_1Zn_1 alloy was preferentially formed. Figure 4.3(c) shows a structural comparison between the Pt (fcc) and Pt_1Zn_1 (tetragonal

AuCu) phases along with a comparison of the Pt-Pt and Pt-Zn bond distances as determined by EXAFS fittings and from the diffraction peaks below 6° in the XRD patterns of the reduced samples at room temperature. The Pt-Pt and Pt-Zn bond distances derived from *in situ* XRD and EXAFS are quite similar except for a small systematic error of ~0.02 Å between the two techniques that has been observed by others. [34] A complete list of Pt and Pt_1Zn_1 unit cell parameters can be found in Table B.3.

The diffraction pattern of $PtZn/SiO_2$ collected at room temperature upon exposure to air after reduction at 600 °C exhibited features in addition to those for the PtZn intermetallic alloy, likely due to surface alloy decomposition induced by exposure to oxygen (Fig. B.7). The difference pattern (black line) obtained by subtraction of the room temperature oxidized $PtZn/SiO_2$ from reduced $PtZn/SiO_2$ is shown in Fig. 4.4. The peaks in the difference pattern correspond to Pt_1Zn_1, and show that the alloy surface structure was identical to that of the fully reduced Pt_1Zn_1 intermetallic nanoparticle. This Pt_1Zn_1 intermetallic structure on the nanoparticle surface isolated all the surface Pt sites and thereby contributed to the high alkane dehydrogenation selectivity. This relation is consistent with previous observations for SiO_2-supported PdZn [19, 20], PdIn [21], and PtIn [22] catalysts.

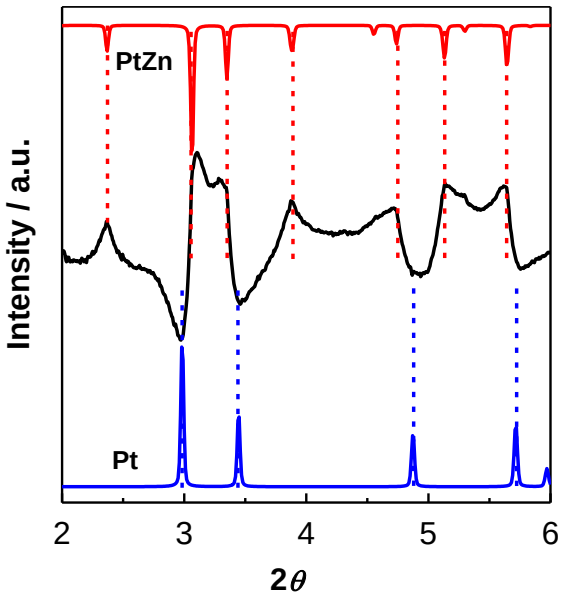

Figure 4.4: *In situ* XRD patterns for PtZn surface layer on $PtZn/SiO_2$. Comparison of simulated XRD patterns for Pt (blue line) and Pt_1Zn_1 (red line) with experimentally obtained difference pattern for 9.53 wt.% Pt – 9.28 wt.% Zn/SiO_2 (black line).

4.3.3 Experimental and Calculated RIXS Planes for Pt and PtZn

Energy differences between the unoccupied and occupied Pt 5*d* states (i.e., the energy transfer, ΔE, see Figure 4.1) for reduced Pt/SiO_2 and $PtZn/SiO_2$ catalysts were examined with *in situ* RIXS by monitoring the Pt L_3 X-ray absorption and emission. The X-ray emission intensity was measured as a function of the incident and emitted photon energies for the Pt L_3 XANES and $L\beta_5$ regions, respectively. The experimentally measured RIXS spectra for Pt/SiO_2 and $PtZn/SiO_2$ are presented in Fig. 4.5 as two-dimensional contour plots that show the energy transfer (ΔE) as a function of the incident photon energy (Ω). For Pt/SiO_2, the maximum RIXS intensity (red region) occurred at Ω = 11,564 eV with an energy transfer of 4.0 eV. Addition of Zn to Pt/SiO_2 shifted the maximum RIXS intensity to higher energy transfer by approximately 2.0 eV at 11,566 eV (ΔE ~ 6 eV), with a high intensity tail that extended along the diagonal to 11,572 eV. A comparison of Pt L_3 XANES in Fig. B.5 for Pt and PtZn indicates that the edge energy of the latter was shifted to 0.9 eV higher than that in the former. Since the energy transfer for Pt_1Zn_1 was 2.0 eV, the energy of the filled valence states was 1.1 eV lower for Pt_1Zn_1 than that in the monometallic Pt sample. The longer tail in the energy transfer plot for Pt_1Zn_1 (Fig. 4.5) is, in part, due to the broader XANES spectrum of PtZn compared to that of Pt (Fig. B.5).

Simulations of *in situ* RIXS spectra for Pt and PtZn were performed on Pt(111) and Pt_1Zn_1(110) surfaces and are also shown in Fig. 4.5. The (111) and (110) close-packed surface orientations were chosen in order to represent the bulk nanoparticle surface structures of Pt and Pt_1Zn_1, respectively. Calculated bulk and surface *d*-DOS were averaged for Pt(111) and Pt_1Zn_1(110) in order to approximate the Pt and Pt_1Zn_1 nanoparticles, respectively. The formalism for calculating RIXS spectra from the DOS has been discussed elsewhere. [24, 35, 36] RIXS intensities (*F*) were calculated from the following equation [24]:

$$F(\Omega,\omega) = \int_{\varepsilon_i}^{\varepsilon_j} d\varepsilon \frac{\rho_d(\varepsilon)\rho'_d(\varepsilon+\Omega-\omega)}{(\varepsilon-\omega)^2+\frac{\Gamma_n^2}{4}}$$

Here, *F* was calculated by integrating over the DOS energies (ε) for the occupied valence states (*i*) and unoccupied valence states (*j*), where $\boldsymbol{\rho_d}$ and $\boldsymbol{\rho'_d}$ are the partial *d*-band DOS of Pt for the occupied and unoccupied states, respectively. The lifetime broadening of the $2p_{3/2}$ core hole

($\boldsymbol{\Gamma_n}$) was taken as 5.41 eV. [24] This method does not account for interactions from the photoexcitation process; however, it has been shown to give accurate results when compared to experiment. [24] The calculations, which were performed by using the *d*-band DOS obtained through self-consistent DFT calculations, exhibited similar features to the experimental spectra. In particular, the simulations revealed a ~1.8 eV increase in the energy transfer of the RIXS maximum that occurred at ~0.9 eV higher incident energy than on Pt(111), in agreement with the measured 0.9 eV edge energy increase for $PtZn/SiO_2$ from *in situ* XAS.

Previous theoretical studies have provided strong evidence that the metal *d*-band center is a useful descriptor of catalytic activity for various transition metals and alloys. [6, 7, 37-40] For the present study, the calculated Pt *d*-band center for monometallic Pt(111) was found to be -2.19 eV and was shifted upward to -2.08 eV for Pt_1Zn_1(110), as shown in Fig. 4.6. Use of a modified electronic structure descriptor [41], defined as the sum of *d*-band center and half the *d*-DOS width, yielded values of -0.64 eV and -0.61 eV for Pt and Pt_1Zn_1, respectively. Such small changes are within the uncertainty of DFT calculations and do not differentiate the electronic properties in these samples. Indeed, when compared to the experimentally measured RIXS spectra in Fig. 4.5, it is evident that the calculated $L\beta_5$ RIXS planes for Pt(111) and Pt_1Zn_1(110), which contain information corresponding to the surface *d*-band DOS that affects catalytic activity, accurately reproduce trends in the PtZn and Pt RIXS signatures and provide additional details regarding the Pt valence electronic structure, including a more direct comparison between theoretical and experimental spectra for Pt and PtZn compared to the *d*-band model alone.

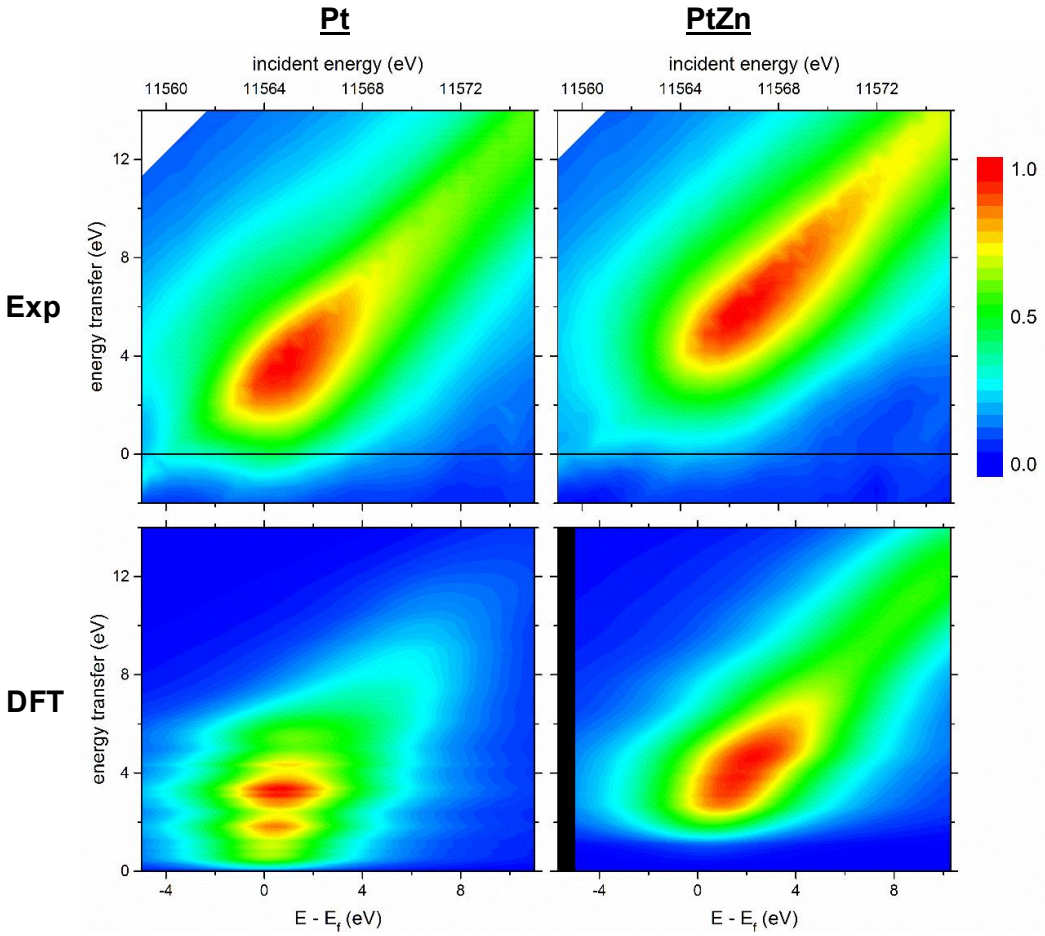

Figure 4.5: RIXS planes for supported Pt and PtZn nanoparticles. Comparisons between experimentally (Exp) measured RIXS for 9.70 wt.% Pt/SiO_2 with calculated RIXS for Pt(111) by DFT (left column), and experimental RIXS for 9.53 wt.% Pt – 9.28 wt.% Zn/SiO_2 with calculated RIXS for Pt_1Zn_1(110) by DFT (right column).

The effect of Zn addition on the energy levels of both the occupied and unoccupied Pt 5*d* bands, evaluated from the energy transfer (ΔE) and Pt L_3 edge energy obtained during *in situ* RIXS and XANES, respectively, is shown in Figure 4.7. Compared to monometallic Pt, the occupied Pt 5*d* bands in PtZn were shifted by approximately 1.1 eV further below the Fermi energy, while the unoccupied bands were shifted to higher energies by approximately 0.9 eV. As discussed in Appendix B, the lower energies of the occupied states led to an upward shift in the high intensity peak for the Pt_1Zn_1 alloy compared to monometallic Pt, while the extended unoccupied states led to a longer tail for PtZn compared to Pt. This combination of lower energy for the filled and higher energy for the unfilled electronic states changes the relative energy between the Pt *d* orbitals in

$PtZn/SiO_2$ and the adsorbate electrons, which decreases the Pt-adsorbate bond energy and increases the number of reaction turnovers per Pt site per unit time. Previous microcalorimetric and DFT studies by Dumesic and coworkers [11-13] have shown that the addition of Zn and Sn ad-metals to Pt- and Pd-containing catalysts weakened the interaction of the metal surface with C_2H_4 to inhibit production of coke-forming ethylidyne species. These findings align with the kinetic and structural characterization results from the present study that show suppressed coke deposition and TOR enhancement on the Pt_1Zn_1 nanoparticle alloys. Furthermore, DFT calculations and *in situ* RIXS measurements indicate that the mechanism of this electronic promotion of Pt by Zn for EDH is driven by changes in energy of the Pt 5*d* electrons, rather than a change in electron occupancy due to electron donation as previously suggested for PtZn [8, 10] and PtCu [40], which effectively reduces the binding energies of adsorbates and increases the TOR per surface Pt.

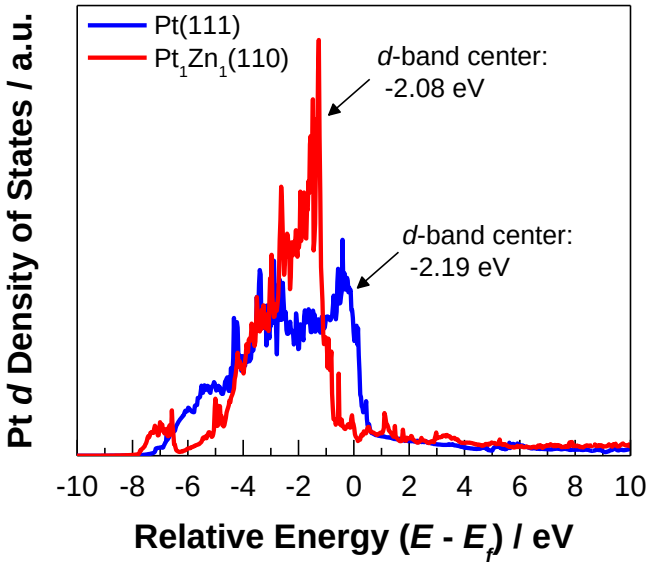

Figure 4.6: Projected density of states (DOS) for *d* orbitals of Pt(111) and $Pt_1Zn_1(110)$. The vertical axis represents the electron density and the horizontal axis corresponds to the energy relative to the Fermi energy (E_f).

A major challenge in the development of catalytic materials is the ability to identify the most important properties of a solid surface which govern its chemical reactivity. The molecular level insight obtained in the present study provides a model to suggest that control of the geometric structure of the Pt active sites affects product selectivity, while control of the metal promoter

affects the adsorbate binding strength and TOR. Furthermore, the direct experimental validation of DFT-predicted RIXS planes for Pt/SiO_2 and $PtZn/SiO_2$ enables new opportunities to investigate relationships between the energy levels of filled and unfilled valence states for various Pt-containing alloys, the binding energies of adsorbates, and their effects on catalytic activity for EDH. While only monometallic Pt and the Pt_1Zn_1 alloy have been considered here for EDH, we envision that this approach could be applied to other nanoparticle alloys and reactions of interest.

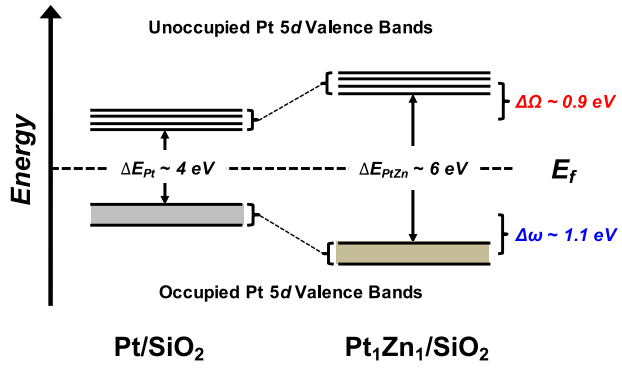

Figure 4.7: Energy Level Diagram for Pt 5d Valence Bands in Pt/SiO_2 and Pt_1Zn_1/SiO_2

4.4 Conclusions

The combined theoretical and experimental approach for EDH on Pt/SiO_2 and $PtZn/SiO_2$ demonstrates that the addition of Zn to Pt effectively suppresses C-C bond cleavage pathways during dehydrogenation at 600 °C to achieve nearly 100% C_2H_4 selectivity up to the thermodynamic limit of C_2H_6 conversion. Additionally, Zn incorporation into the Pt nanoparticles leads to a six-fold TOR increase per mole of surface Pt compared to the monometallic Pt catalyst.

Geometric and electronic characterization reveals that the Pt active sites on the surface of the metallic nanoparticles in these catalysts are both structurally and chemically different. The role of the Zn promoter is two-fold: (i) to form a Pt_1 Zn_1 intermetallic alloy structure with uniformly isolated Pt surface sites that effectively suppress the rate of structure-sensitive reactions, such as hydrogenolysis and cracking, while retaining the structure-insensitive dehydrogenation pathway, and (ii) to lower the energy of the filled states of the Pt surface; thus, weakening the bond formation

between the 5*d* orbitals and adsorbates. While the selectivity changes may be explained by an ensemble effect related to isolated Pt sites, the TOR enhancement implies an electronic change within the individual Pt atoms, as evidenced by differences in apparent activation energies along with an increase in the Pt RIXS ΔE for $PtZn/SiO_2$ compared to the monometallic Pt/SiO_2 sample. The agreement between experimental and theoretical energies of the Pt 5*d* valence orbitals for the Pt and Pt_1Zn_1 nanoparticles in this application demonstrates that DFT calculations provide accurate simulations of the RIXS spectra, yielding insights into the electronic structural details and reactivity of these metal surfaces while also supplementing existing studies based on the first moment of the *d*-band.

4.5 Experimental

4.5.1 Catalyst Synthesis

4.5.1.1 Pt/SiO_2.

The incipient wetness impregnation (IWI) method was used with 5 g of commercially available high-purity SiO_2 (Davisil Grade 636, 480 m^2 g^{-1}) and an aqueous solution of 0.8 g $(NH_3)_4Pt(NO_3)_2$ (Sigma Aldrich) in 5 ml deionized water for ~5 wt.% Pt loading. The pre-catalyst was dried in an oven at 100 °C for 24 h, followed by a second impregnation of 0.8 g $(NH_3)_4Pt(NO_3)_2$ in 5 ml deionized water to obtain 9.70 wt.% Pt loading, as measured by elemental analysis (Galbraith Labs). The sample was dried a second time at 100 °C for 24 h, and then calcined in air at 225 °C for 3 h. After cooling to room temperature (RT), the sample was reduced in 25% H_2 and balance He according to the following temperature cycle: (i) ramp from RT to 100 °C at 5 °C min^{-1}, hold at 100 °C for 15 min; (ii) ramp to 150 °C at 5 °C min^{-1}, hold at 150 °C for 15 min; (iii) ramp to 200 °C at 2.5 °C min^{-1}, hold at 200 °C for 30 min; (iv) ramp to 225 °C at 2.5 °C min^{-1}, hold at 225 °C for 30 min; (v) ramp to 300 °C at 2.5 °C min^{-1}, hold at 300 °C for 15 min; (vi) ramp to 600 °C at 5 °C min^{-1}, hold at 600 °C for 15 min; (vii) purge with He at 600 °C for 15 min and cool to RT in He.

4.5.1.2 $PtZn/SiO_2$.

An aqueous solution of $Zn(NO_3)_2$ was prepared by dissolving 1.8 g of $Zn(NO_3)_2{\cdot}6H_2O$ (Sigma Aldrich) into 3 ml of deionized water and adjusting the pH to 11 with 2 ml concentrated

NH_4OH. Deionized water was added to raise the solution volume to 10 ml. IWI was used with 5 g of high-purity SiO_2 (Davisil Grade 636, 480 m^2 g^{-1}) and the $Zn(NO_3)_2$ solution to obtain ~5 wt.% Zn loading. The pre-catalyst was dried in an oven at 100 °C for 24 h, followed by a second impregnation of $Zn(NO_3)_2$ solution (pH adjusted to 11) to obtain 9.28 wt.% Zn loading. The sample was dried a second time at 100 °C for 24 h, and then calcined in air at 550 °C for 3 h followed by annealing in He at 600 °C for 15 min. After cooling to RT, the 10 wt.% Zn/SiO_2 sample was twice impregnated with aqueous solutions of 0.8 g $(NH_3)_4Pt(NO_3)_2$ (Sigma Aldrich) in 5 ml deionized water to obtain 9.53 wt.% Pt loading. The final Zn and Pt loadings were measured by elemental analysis (Galbraith Labs). The 9.53 wt.% Pt – 9.28 wt.% Zn/SiO_2 pre-catalyst was calcined in air and reduced in 25% H_2 and balance He per the same procedure as the 9.70 wt.% Pt/SiO_2 catalyst.

4.5.2 Ethane Dehydrogenation Kinetics

Catalyst testing was performed in a quartz, plug-flow reactor (9.5 mm I.D.) with a U-shaped effluent line. The catalyst section has a well for a K-type thermocouple (3.2 mm O.D.) for temperature indication that is contained within a quartz sheath and placed in the bottom center of the catalyst bed to measure the reaction temperature inside of the bed. A furnace connected to a temperature controller is used to supply heat to the reactor and maintain the reaction at the desired temperature. The mass of the catalyst sample ranged from 0.01 g to 0.2 g, depending upon the desired conversion. The catalyst was diluted with high-purity SiO_2 (Davisil Grade 636, 480 m^2 g^{-1}) to maintain the catalyst bed height at ~12.7 mm (1/2 in).

The reactor gas delivery system consists of five mass flow controllers (2-Brooks 5850E, 2-Porter 201, 1-Tylan FC-260) and a manifold that mixes the gases prior to entering the reactor. First, the catalyst was reduced in 5% H_2 (Praxair, 99.999%) and balance N_2 (Matheson, 99.995%) at 40 ml min^{-1} total flow while the temperature was ramped from RT to 600 °C at 10 °C min^{-1} and then held at 600 °C for 30 min. The total flow rate was confirmed at the reactor outlet. Then, following the reduction, the EDH reaction mixture was introduced into the reactor at 600 °C and 150 ml min^{-1} total flow. The EDH reaction mixture consists of 2.5% C_2H_6 (Matheson, 99.95%), 1% H_2 (Praxair, 99.999%), 0.5% C_2H_4 (Matheson, 99.999%), 46.7% He (Matheson, 99.999%), and balance N_2 (Matheson, 99.995%), which was used as an internal standard. The reactor effluent was analyzed by using a Hewlett Packard 5890 Series II gas chromatograph (GC) equipped with a thermal conductivity detector (TCD). A Carboxen-1010 PLOT Capillary GC Column was used to separate

the components in the reactor effluent gas mixture. After the C_2H_6 conversion stabilized below 10% at 600 °C, the apparent activation energy (E_{app}) was measured between 570 °C and 600 °C. Details regarding the calculation of EDH rates, ethane conversion, and ethylene selectivity can be found in Appendix B. During each run, carbon mass balances closed from 83 – 100% for Pt/SiO_2 (with C_2H_4 co-fed), 95 – 100% for Pt/SiO_2 (without C_2H_4 co-fed), and ~100% for both $PtZn/SiO_2$ with and without C_2H_4 co-fed.

4.5.3 X-ray Characterization

4.5.3.1 *In situ* X-ray Absorption Spectroscopy

Platinum L_3 (11,564 eV) XAS experiments were performed in transmission mode at the Materials Research Collaborative Access Team (MRCAT) bending magnet (10-BM) beamline at the Advanced Photon Source (APS) within Argonne National Laboratory to identify the Pt chemical state, coordination (N), types of nearest neighbors, and interatomic bond distances (R). A cylindrical sample holder containing six wells to hold self-supporting catalyst wafers was placed inside of a quartz tube (25.4 mm O.D.) and sealed with Kapton windows and Ultra-Torr fittings to allow gases to flow through the cell. The thickness of the catalyst wafers (~15 mg) was chosen to give an X-ray absorbance of approximately 2.0 and a Pt edge step of approximately 0.5. After reduction at 600 °C in 3% H_2 and balance He, the Pt/SiO_2 and $PtZn/SiO_2$ samples were cooled to room temperature in H_2 and then X-ray absorption spectra were collected by using standard methods and energy calibrated to the simultaneously obtained edge position of a Pt foil. The Pt edge energy was determined based on the position of the maximum of the first peak in the first derivative of the XANES region. Phase shifts and backscattering amplitudes for the EXAFS spectra were determined for monometallic Pt scatterers (i.e. Pt-Pt) based on the experimentally obtained Pt foil spectra (12 scatterers at 2.77 Å). Pt-Zn scatterers were calculated by using two atom calculations with FEFF6 code. [42-43] X-ray absorption spectra were analyzed with WinXAS v. 3.11 software. [44] The values for the amplitude reduction factor, S_0^2, and Debye-Waller factor (DWF), $\Delta\sigma^2$, were determined by fitting the foils with FEFF. The EXAFS parameters were calculated for the first scattering shell by using the FEFF references and performing a least squares fit in R-space of the k^2-weighted Fourier transform. Once the nanoparticle structure was determined by XRD, the final EXAFS fit was performed by using Artemis software [45] based on a two shell fit (i.e., Pt-Zn and Pt-Pt) of the Pt_1Zn_1 structure.

4.5.3.2 Synchrotron X-ray Diffraction

XRD measurements were performed in transmission mode at the Sector 11 insertion device (11-ID-C) beamline at the APS. XRD patterns were acquired by using X-rays at 105 keV (λ = 0.11798 Å) and a PerkinElmer large area detector with a typical exposure time of 5 s and a total of 30 scans. Catalyst samples were pressed into cylindrical, self-supporting wafers (d ~ 7 mm) and placed on a Pt crucible inside of a ceramic sample cup within a Linkam Scientific TS1500 heating stage. The heating stage is equipped with water cooling and allows for temperature-controlled operation while flowing gases across the catalyst wafer. The 2-D scattering images were converted to 1-D scattering patterns by using Fit2D software in order to obtain plots of intensity as a function of 2θ. [46] Materials Analysis Using Diffraction (MAUD) v. 2.55 software was used to simulate standard XRD patterns of Pt, Pt_1Zn_1, Pt_3Zn, Pt_3Zn_{10}, and $PtZn_{1.7}$ phases. [47-50] These simulated patterns were then compared with the experimentally measured pattern for 10 wt.% Pt/SiO_2 and 10 wt.% $PtZn/SiO_2$.

4.5.3.3 Resonant Inelastic X-ray Scattering

RIXS measurements were obtained on the MRCAT insertion device (10-ID) beamline at the APS. Catalyst samples (~50-75 mg) were pressed into self-supporting wafers at a 45° angle and placed inside of a custom *in situ* gas cell that is equipped with a resistively-heated sample stage, water-cooled Kapton windows, dual thermocouples for temperature indication and control, and connections to allow gases to flow through the cell. [51] The catalysts were reduced in 3% H_2 and balance He (50 ml min^{-1} total flow) at 550 °C for 0.5 h, and then cooled to 100 °C in the same gas mixture prior to analysis.

The X-ray emission spectrometer was based on a bent silicon Laue analyzer [52], optimized for high resolution. Soller slits were used for background suppression and a Pilatus 100K pixel area detector (Dectris Ltd.) was used to detect the X-rays. The silicon analyzer element was a 55 μm thick wafer, <100> orientation, cylindrically bent to a minimum radius of 480 mm (as a logarithmic spiral). The (133) reflection with a calculated asymmetry of 13.26° was used to select the pass band. The calculated reflectivity, absorption, and local bandwidth at 11,560 eV were 53%, 30%, and 1.1 eV, respectively. Soller slits absorbed unreflected X-rays and reduced the background scatter. To generate the RIXS planes, the incident X-ray energy was scanned from 11,547 eV to 11,589 eV in 0.7 eV steps above 11,558 eV. The entire emission energy range was

measured at once by carefully setting the analyzer angle and distance from the sample. Once set, the analyzer remained fixed during the measurement. Each pixel of the array detector then must be assigned an energy. Resonant valence emission has a complication for energy calibration in that the elastic scatter and the X-ray emission are at nearly the same energy over a portion of the spectrum. Post-processing of the images was required to generate energy masks for the entire array detector surface. These masks were used to convert the images into intensity versus X-ray energy. To balance the intensity of the elastically scattered X-rays used for calibration with the low background required to observe the X-ray emission, the center of the analyzer was offset by 10° elevation from the plane of the X-ray beam polarization, while being set at 90° in the plan view of the beam, sample, and analyzer. The combined energy resolution of the source, beam size, and analyzer was measured to be about 2.4 eV: comparable to the calculated resolution (2.1 eV) and as well as the valence emission line width.

4.5.4 DFT Methods

All calculations were performed by using self-consistent, periodic density functional theory (DFT), as implemented within the Vienna Ab-Initio Simulation Package (VASP). [53-56] The Perdew-Burke-Ernzerhof exchange-correlation functional was used for all calculations. [57] The projector augmented wave (PAW) core potentials developed from PBE calculations were used. [58, 59] For the Pt and PtZn bulk lattice optimizations, a cutoff energy of 600 eV and a 20x20x20 Monkhorst-Pack K-point grid with Methfessel-Paxton smearing was used to accurately reduce Pulay stress. Lattice constants are converged to within a force criterion of 0.02 eV $Å^{-1}$, which resulted in lattice parameters of 3.98 Å for Pt and 2.88 Å and 3.53 Å for the *a* and *c* unit vectors, respectively, of Pt_1Zn_1. For DOS calculations on the Pt and Pt_1Zn_1 bulk, a cutoff energy of 1000 eV and a 30x30x30 Monkhorst-Pack K-point grid was implemented along with tetrahedron Blöchl smearing. The projected density of state (PDOS) was lm-decomposed according to the Wigner-Seitz radius provided by the PAW potential. Close packed surfaces corresponding to the (111) for Pt as well as the (110) and (101) surfaces for Pt_1Zn_1 were cut from the lattice optimized bulk. Each surface was a 5 layer slab with 10 Å vacuum. Cell dimensions for the Pt surface were 5.62 Å, 5.62 Å, and 29.18 Å along the *a*, *b*, and *c* unit vectors, respectively, including vacuum. Cell dimensions for the Pt_1Zn_1(110) surface were 4.08 Å, 3.53 Å, and 28.16 Å along the *a*, *b*, and *c* unit vectors, respectively, including vacuum. Cell dimensions for the

PtZn(101) surface were 4.58 Å, 2.88 Å, and 28.93 Å. A comparison of the predicted RIXS planes for the (110) and (101) surfaces is included in Appendix B. The bottom two layers were fully constrained and the rest of the slab was allowed to relax to a force criterion of 0.02 eV $Å^{-1}$. An energy cutoff of 400 eV, 6x6x1 Monkhorst-Pack K-point grid, and Methfessel-Paxton smearing was found to minimize Pulay stress and converge total energies. DOS calculations were performed with a 1000 eV cutoff energy, 8x8x1 Monkhorst-Pack K-point grid, and tetrahedron Blöchl smearing by using the relaxed surface geometries.

4.6 Acknowledgements

Support for this research was provided by Qatar National Research Fund No. 13121024. Use of the Advanced Photon Source is supported by the U.S. Department of Energy, Office of Science, and Office of Basic Energy Sciences, under Contract DE-AC02-06CH11357. MRCAT operations are supported by the Department of Energy and the MRCAT member institutions. We also acknowledge the use of beamline 11-ID-C at the Advanced Photon Source. J.G. and B.C.B. acknowledge support from the DMREF program of the National Science Foundation (CBET1437219). We would like to thank Chang Wan Han and Volkan Ortalan in the School of Materials Engineering at Purdue University for providing the STEM and TEM images.

4.7 References

1. Siirola, J. J., AIChE J. 2014, 60, 810-819.
2. Sattler, J. J. H. B.; Ruiz-Martinez, J.; Santillan-Jimenez, E.; Weckhuysen, B. M., Chem. Rev. 2014, 114, 10613-10653.
3. Bhan, A.; Nicholas Delgass, W., Catal. Rev. 2008, 50, 19-151.
4. Sattler, J. J. H. B.; Gonzalez-Jimenez, I. D.; Luo, L.; Stears, B. A.; Malek, A.; Barton, D. G.; Kilos, B. A.; Kaminsky, M. P.; Verhoeven, T.; Koers, E. J.; Baldus, M.; Weckhuysen, B. M., Angew. Chem. Int. Ed. 2014, 53, 9251-9256.
5. Biscardi, J. A.; Iglesia, E., Catal. Today 1996, 31, 207-231.
6. Hammer, B.; Nørskov, J. K., Adv. Catal. 2000, 45, 71-129.
7. Hammer, B.; Nørskov, J. K., Surf. Sci. 1995, 343, 211-220.
8. Yu, Z.; Sawada, J. A.; An, W.; Kuznicki, S. M., AIChE J. 2015, 61, 4367-4376.
9. Andy, P.; Davis, M. E., Ind. Eng. Chem. Res. 2004, 43, 2922-2928.
10. Yu, C. L.; Xu, H. Y.; Ge, Q. J.; Li, W. Z., J. Mol. Catal. A Chem. 2007, 266, 80-87.
11. Hill, J. M.; Shen, J. Y.; Watwe, R. M.; Dumesic, J. A., Langmuir 2000, 16, 2213-2219.
12. Shen, J. Y.; Hill, J. M.; Watwe, R. M.; Spiewak, B. E.; Dumesic, J. A., J. Phys. Chem. B 1999, 103, 3923-3934.
13. Silvestre-Albero, J.; Sanchez-Castillo, M. A.; He, R.; Sepulveda-Escribano, A.; Rodriguez-Reinoso, F.; Dumesic, J. A., Catal. Lett. 2001, 74, 17-25.
14. Boudart, M.; Djega-Mariadassou, G., Structure-Insensitive and Structure-Sensitive Reactions on Metals. In Kinetics of Heterogeneous Catalytic Reactions, 1 ed.; Princeton University Press: Princeton, NJ, 1984; pp 155-193.
15. Yang, M.-L.; Zhu, Y.-A.; Fan, C.; Sui, Z.-J.; Chen, D.; Zhou, X.-G., Phys. Chem. Chem. Phys. 2011, 13, 3257-3267.
16. Virnovskaia, A.; Rytter, E.; Olsbye, U., Ind. Eng. Chem. Res. 2008, 47, 7167-7177.
17. Galvita, V.; Siddiqi, G.; Sun, P.; Bell, A. T., J. Catal. 2010, 271, 209-219.
18. Yagasaki, E.; Masel, R. I., Surf. Sci. 1989, 222, 430-450.
19. Childers, D. J.; Schweitzer, N. M.; Shahari, S. M. K.; Rioux, R. M.; Miller, J. T.; Meyer, R. J., J. Catal. 2014, 318, 75-84.
20. Gallagher, J. R.; Childers, D. J.; Zhao, H. Y.; Winans, R. E.; Meyer, R. J.; Miller, J. T., Phys. Chem. Chem. Phys. 2015, 17, 28144-28153.

21. Wu, Z.; Wegener, E. C.; Tseng, H. T.; Gallagher, J. R.; Harris, J. W.; Diaz, R. E.; Ren, Y.; Ribeiro, F. H.; Miller, J. T., Catal. Sci. Tech. 2016, 6, 6965-6976.
22. Wegener, E. C.; Wu, Z.; Tseng, H.-T.; Gallagher, J. R.; Ren, Y.; Diaz, R. E.; Ribeiro, F. H.; Miller, J. T., Catalysis Today 2018, 299, 146-153
23. Singh, J.; Lamberti, C.; van Bokhoven, J. A., Chem. Soc. Rev. 2010, 39, 4754-4766.
24. Glatzel, P.; Singh, J.; Kvashnina, K. O.; van Bokhoven, J. A., J. Am. Chem. Soc. 2010, 132, 2555-2557.
25. Singh, J.; Nelson, R. C.; Vicente, B. C.; Scott, S. L.; van Bokhoven, J. A., Phys. Chem. Chem. Phys. 2010, 12, 5668-5677.
26. Pollock, C. J.; DeBeer, S., Acc. Chem. Res. 2015, 48, 2967-2975.
27. Meyer, D. A.; Zhang, X. N.; Bergmann, U.; Gaffney, K. J., J. Chem. Phys. 2010, 132, 1345021-1345028.
28. Thomas, R.; Kas, J.; Glatzel, P.; Al Samarai, M.; de Groot, F. M. F.; Mori, R. A.; Kavcic, M.; Zitnik, M.; Bucar, K.; Rehr, J. J.; Tromp, M., J. Phys. Chem. C 2015, 119, 2419-2426.
29. Glatzel, P.; Yano, J.; Bergmann, U.; Visser, H.; Robblee, J. H.; Gu, W. W.; de Groot, F. M. F.; Cramer, S. P.; Yachandra, V. K., J. Phys. Chem. Solids 2005, 66, 2163-2167.
30. Zhou, Y.; Doronkin, D. E.; Chen, M. L.; Wei, S. Q.; Grunwaldt, J. D., ACS Catal. 2016, 6, 7799-7809.
31. Kale, M. J.; Christopher, P., ACS Catal. 2016, 6, 5599-5609.
32. Lei, Y.; Jelic, J.; Nitsche, L. C.; Meyer, R.; Miller, J. T., Top. Catal. 2011, 54, 334-348.
33. Miller, J. T.; Kropf, A. J.; Zha, Y.; Regalbuto, J. R.; Delannoy, L.; Louis, C.; Bus, E.; van Bokhoven, J. A., J. Catal. 2006, 240, 222-234.
34. Gallagher, J. R.; Li, T.; Zhao, H.; Liu, J.; Lei, Y.; Zhang, X.; Ren, Y.; Elam, J. W.; Meyer, R. J.; Winans, R. E.; Miller, J. T., Catal. Sci. Technol. 2014, 4, 3053-3063.
35. Kotani, A.; Shin, S., Rev. Mod. Phys. 2001, 73, 203-246.
36. Jiménez-Mier, J.; van Ek, J.; Ederer, D. L.; Callcott, T. A.; Jia, J. J.; Carlisle, J.; Terminello, L.; Asfaw, A.; Perera, R. C., Phys. Rev. B 1999, 59, 2649-2658.
37. Mavrikakis, M.; Hammer, B.; Nørskov, J. K., Phys. Rev. Lett. 1998, 81, 2819-2822.
38. Hammer, B.; Norskov, J. K., Nature 1995, 376, 238-240.
39. Hammer, B.; Morikawa, Y.; Nørskov, J. K., Phys. Rev. Lett. 1996, 76, 2141-2144.

40. Linke, R.; Schneider, U.; Busse, H.; Becker, C.; Schröder, U.; Castro, G. R.; Wandelt, K., Surf. Sci. 1994, 307, 407-411.
41. Vojvodic, A.; Norskov, J. K.; Abild-Pedersen, F., Top. Catal. 2014, 57, 25-32.
42. Rehr, J. J.; Albers, R. C.; Zabinsky, S. I., Phys. Rev. Lett. 1992, 69, 3397-3400.
43. Rehr, J. J.; Albers, R. C., Phys. Rev. B 1990, 41, 8139-8149.
44. Ressler, T., J. Synchrotron Radiat. 1998, 5, 118-122.
45. Ravel, B.; Newville, M., J. Synchrotron Radiat. 2005, 12, 537-541.
46. Hammersley, A. P.; Svensson, S. O.; Hanfland, M.; Fitch, A. N.; Hausermann, D., High Pressure Res. 1996, 14, 235-248.
47. Hull, A. W., Phys. Rev. 1921, 17, 571-588.
48. Nowotny, H.; Bauer, E.; Stempfl, A., Monatsh. Chem. 1950, 81, 1164-1164.
49. Nowotny, H.; Bauer, E.; Stempfl, A.; Bittner, H., Monatsh. Chem. 1952, 83, 221-236.
50. Johansso.A; Westman, S., Acta Chem. Scand. 1970, 24, 3471-3479.
51. Bolin, T. B.; Wu, T.; Schweitzer, N.; Lobo-Lapidus, R.; Kropf, A. J.; Wang, H.; Hu, Y.; Miller, J. T.; Heald, S. M., Catal. Today 2013, 205, 141-147.
52. Kropf, A. J.; Fortner, J. A.; Finch, R. J.; Cunnane, J. C.; Karanfil, C., Phys. Scripta 2005, T115, 998-1000.
53. Kresse, G.; Hafner, J., Phys. Rev. B 1993, 47, 558-561.
54. Kresse, G.; Hafner, J., Phys. Rev. B 1994, 49, 14251-14269.
55. Kresse, G.; Furthmüller, J., Comput. Mater. Sci. 1996, 6, 15-50.
56. Kresse, G.; Furthmüller, J., Phys. Rev. B 1996, 54, 11169-11186.
57. Perdew, J. P.; Burke, K.; Ernzerhof, M., Phys. Rev. Lett. 1996, 77, 3865-3868.
58. Blöchl, P. E., Phys. Rev. B 1994, 50, 17953-17979.
59. Kresse, G.; Joubert, D., Phys. Rev. B 1999, 59, 1758-1775.
60. Boudart, M.; Djega-Mariadassou, G., Kinetics of Overall Reactions. In *Kinetics of Heterogeneous Catalytic Reactions*, 1st ed.; Princeton University Press: Princeton, NJ, 1984; pp 77-90.

CHAPTER 5. PT-FE INTERMETALLIC NANOPARTICLES: EFFECT OF ALLOY PHASE ON PROPANE DEHYDROGENATION

5.1 Abstract

In this work, a series of silica-supported Pt-Fe bimetallic catalysts were synthesized and compared to monometallic Pt and Fe catalysts for propane dehydrogenation. *In situ* X-ray absorption spectroscopy (XAS) and X-ray diffraction (XRD) revealed that Pt and Fe formed intermetallic alloys and that the phase varied with the Fe:Pt ratio. As the atomic ratio was increased, first the Pt_3Fe phase was formed, then PtFe, and lastly $PtFe_3$. When tested for propane dehydrogenation the bimetallic catalysts were greater than 95% selective towards propylene. Monometallic Pt was only 75% selective and the Fe catalyst showed no activity under the test conditions used. The Pt-Fe catalysts also exhibited higher apparent turnover rates (TOR) than monometallic Pt. The elimination of Pt ensembles, the active site for undesirable side reactions, in the alloy structures is proposed to be the dominate factor responsible for the increase in selectivity. The increase in TOR suggests changes to the valance electronic states of Pt upon alloy formation. To investigate the changes in the 5d-states of Pt, *in situ* resonant inelastic X-ray scattering (RIXS) measurements were performed on the Pt-Fe and Pt catalysts and corroborated with density functional theory calculations (DFT). The electronic structure measurements and calculations revealed that as the alloy structures become more Fe rich the average energies of the unfilled and filled states increase and decrease, respectively. It is believed that this change in energy of the valance states is the dominant electronic effect of alloy formation.

5.2 Introduction

The findings from the previous chapters support geometric changes upon alloying being the dominant factor leading to increased catalyst selectivity for alkane dehydrogenation. The formation of specific intermetallic structures eliminates ensembles of catalytic atoms responsible for hydrogenolysis, a structure sensitive reaction, while dehydrogenation, a structure insensitive reaction, is unaffected. These results suggest that promoters other than the traditionally post-transition metals could be used to make selective catalysts if they can form the correct structures.

The bulk Pt-Fe phase diagram (Figure 5.1) shows three intermetallic compound phases: Pt_3Fe (Cu_3Au), PtFe (CuAu), and $PtFe_3$ (Cu_3Au).

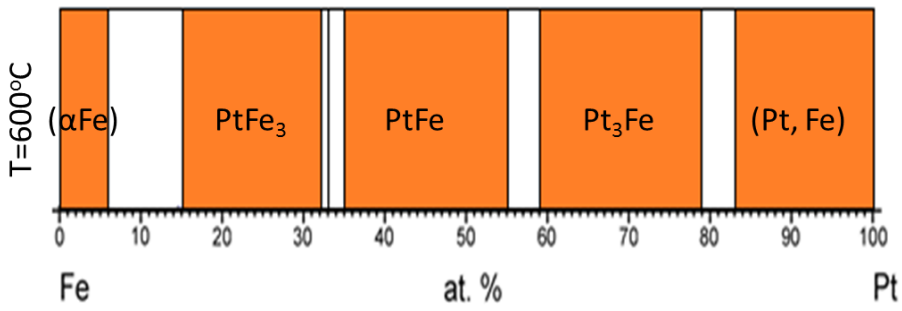

Figure 5.1: Pt-Fe phase diagram at 600 °C adapted form Okamoto [1]

All three phases are cubic and would require minimal atomic rearrangement to form. Pt_3Fe and PtFe have the same structure types as IMC catalysts which have been reported to be selective for alkane dehydrogenation [2-9]. While catalysts with the same structure as the $PtFe_3$ phase have not been reported as selective alkane dehydrogenation catalysts, the Pt atoms are geometrically isolated by Fe. Pt-Fe catalysts have been reported to be selective for isobutane dehydrogenation. [10] The improved olefin selectivity compared to Pt was attributed to the formation of bimetallic particles, but the exact structure of the catalyst was not determined.

Unlike the post-transition metals commonly used as promoters, Fe has an unfilled d-shell in the metallic state. This likely results in Pt-Fe alloys having different electronic properties from intermetallic compounds of Pt and post-transition metals. If the Pt-Fe IMC phases are formed, it allows for the study of catalysts with the same structures as those reported to be selective, but different electronic properties. This affords the opportunity to investigate the role of electronic changes during alkane dehydrogenation reactions.

In this chapter a study on Pt-Fe bimetallic catalysts is discussed. A series of Pt-Fe bimetallic catalysts were synthesized with varying Fe:Pt atomic ratios and compared to monometallic Pt and Fe catalysts for propane dehydrogenation. The structures of the catalysts were determined using *in situ* X-ray absorption spectroscopy and *in situ* X-ray diffraction. Electronic structure measurements were performed by *in situ* resonant inelastic X-ray scattering. Experimental results

were substantiated with density functional theory calculations which also provided insight into the potential effect of electronic changes on difference in catalytic properties.

5.3 Methods

5.3.1 Catalyst Synthesis

A series of silica supported Pt-Fe bimetallic catalysts were synthesized with different Fe:Pt atomic ratios and nominal Pt and Fe loading by sequential incipient wetness impregnation. The general synthesis procedure involved dissolving the required amount of $Fe(NO_3)_3 \cdot 9H_2O$ (Sigma Aldrich) in 1.5 mL of water. An equimolar amount of citric acid (Sigma Aldrich) was added to the $Fe(NO_3)_3$ solution and the mixture was stirred until no solids remained. Ammonium hydroxide (30% in water) was added to the solution until a pH of 12. If necessary, water was added to the basic solution to bring the total volume to the pore volume of the silica support. The Fe solution was added dropwise to the bare silica support (Davisil 636 silica gel, Sigma Aldrich, 480 m2/g surface area and 0.75 mL/g pore volume) with constant stirring. The obtained catalyst was dried in air first at room temperature for 0.5 hr and then at 125 ^oC overnight. The dried Fe/SiO_2 catalyst was then calcined at 550 ^oC for 3 hr in air. Following calcination, the necessary amount of $Pt(NH_3)_4(NO_3)_2$ (Sigma Aldrich) was dissolved in 1.5 mL of water and ammonium hydroxide solution was added until a pH of 12. Water was added to the solution to bring the total volume to that of the pore volume of the dried Fe/SiO2 catalyst. The Pt solution was added dropwise to the Fe/SiO_2 catalyst with constant stirring. The $Pt\text{-}Fe/SiO_2$ catalyst was dried at room temperature in air for 0.5 hr and then overnight in air at 125 ^oC. The dried $Pt\text{-}Fe/SiO_2$ catalysts were calcined at 225 ^oC for 3 hr. The calcined catalysts were reduced at 225 ^oC in 50% H_2/N_2 mixture at a flow of 200 cc/min for 0.5 hr and then 600 ^oC for 1 hr in the same atmosphere.

For comparison, monometallic Pt (2 wt. %) and Fe (10 wt. %) catalysts were synthesized via incipient wetness impregnation. For the Pt catalysts the required amount of $Pt(NH_3)_4(NO_3)_2$ was dissolved in 1.5 mL of water and aqueous ammonium hydroxide was added to the solution until a pH of 12 was reached. Water was then added to the basic solution to make the total volume equal to the pore volume of the silica support. The final solution was added dropwise to the SiO_2 support with constant stirring. Once all the liquid was added the catalyst was dried in air at room temperature for 0.5 hr and then overnight at 125 ^oC. The dried catalyst was calcined at 400 ^oC in

air for 3 hr and then reduced in a 50% H_2/N_2 mixture with a flow of 200 cc/min at 225 ^oC for 0.5 hr and then at 600 ^oC for 1 hr.

For the Fe catalyst the required amount of $Fe(NO_3)_3 \cdot 9H_2O$ was dissolved in 1.5 mL of water. Citric acid was added in an equimolar amount and the solution was stirred until all solids had dissolved. Ammonium hydroxide solution was added until a pH of 12 and then the solution was brought up to four times the pore volume of the bare silica support with water. One quarter of the solution was added to the silica with constant stirring. The obtained catalyst was dried at room temperature in air for 0.5 hr, overnight at 125 ^oC in air, and the dried catalyst was calcined at 550 ^oC for 3 hr. The impregnation and drying steps were then repeated until all the solution had been added to the silica. The calcined catalyst was then reduced at 750 ^oC for 3 hr in 50% H_2/N_2 at a flow of 200 cc/min.

5.3.2 *In situ* X-ray Absorption Spectroscopy (XAS)

XAS measurements were conducted on the bending magnet beamline of the Materials Research Collaborative Access Team (MR-CAT) at the Advanced Photon Source (APS), Argonne National Laboratory at the Pt L_{III} Edge (11.564 keV) and the Fe K edge (7.112 keV). Spectra were collected in step-scan transmission mode in about 15 minutes.

Catalysts were ground into fine powders and pressed into a stainless-steel sample holder to form self-supporting wafers. Sample holders were placed in quartz tube reactors with ports containing Kapton windows through which gases could be flowed. Samples were reduced in 100 cc/min flow of 3% H_2/He at 550 ^oC for 30 min. Prior to measurements the reaction cells were purged with He to remove adsorbed H_2. Trace oxidants in He were removed by passing the gas through a Matheson PUR-Gas Triple Purifier Cartridge. Samples were cooled to room temperature and scans were performed at room temperature in He. After scans of the reduced catalysts were collected the samples were treated in 100 ccm air at room temperature for 20 min and rescanned to obtain the oxidized spectra used for ΔXANES.

XAS data was fit using WINXAS 3.1 software. [11] At the Pt L_{III} edge, EXAFS coordination parameters were obtained by least-squares fit in R-space of the k^2-weighted Fourier transform data from 3.00 Å to 11.40 Å. First shell fits of the magnitude and imaginary parts were performed from 1.8 to 2.9 Å. Fits were performed by refinement of the coordination numbers (CN), bond distances (R), and energy shift (E_o). $\Delta\sigma^2$ values for Pt-Pt and Pt-Fe scattering were

determined from the Pt and Pt-Fe(4.4) samples, respectively, and the values were held constant for Pt-Fe(0.7) and Pt-Fe(2.9). Experimental phase and amplitude fitting functions for Pt-Pt scattering pairs were obtained from Pt foil (12 Pt-Pt bonds at 2.77 Å). Pt-Fe phase and amplitude fitting functions were obtained from FEFF calculations. [12, 13] S_o^2 (0.73) and σ^2 (0.004) were determined from a Pt foil. ΔEXAFS spectra were obtained by subtracting chi of the samples after oxidation from chi of the samples after reduction and were fit using the same procedure as the reduced samples. A Pt-O scattering path was included in the fits and experimental phase shift and amplitude fitting function were obtained from $Na_2Pt(OH)_6$ (6 Pt-O bonds at 2.05 Å). Pt L_{III} ΔXANES spectra used to estimate the Pt dispersion of the bimetallic catalysts were obtained by subtracting the normalized XANES of the samples after reduction from those of the samples after oxidation.

5.3.3 *In situ* X-ray Diffraction (XRD)

In situ XRD measurements were performed at the 11-ID-C beam line of the X-ray Science Division at the APS, Argonne National Lab. Diffraction patterns were collected in transmission mode with a PerkinElmer large area detector using X-rays with a wavelength of 0.117418 Å. Samples were ground into a fine powder, pressed into wafers, and loaded into a Linkam Thermal Stage through which gases could be flowed. Catalysts were reduced in 3% H_2/He at a flow of 100 cc/min at 550 ^oC for 10 min before spectra were collected. Diffraction patterns (the summation of 3 sets of 30 exposures of 5 seconds each) were collected at 550 ^oC in the H_2/He mixture. The cell was then cooled to 35 ^oC under the same atmosphere and patterns collected. The obtained 2-D diffraction patterns were integrated to 1-D intensity versus 2Θ plots using GSAS-2 software. [14] Materials Analysis Using Diffraction (MAUD) software was used to simulate theoretical diffraction patterns of potential Pt-Fe alloy phases which were used to determine the crystal structure of each catalyst. [15]

5.3.4 Catalyst Testing

Propane dehydrogenation reactions were performed using a vertical, quartz tube reactor (O.D. 0.5 in.) with gases supplied by mass flow controllers. The outlet stream was analyzed by online gas chromatography using an FID detector. The GC outlet was equipped with a back-pressure regulator and the system pressure was held constant at 5 psig. The catalyst loading was

varied to obtain different initial conversions and approximately 0.5 g of SiO_2 was used as a diluent to give a constant bed height of 1 in. The catalyst was supported on quartz wool and a stainless-steel thermocouple well was placed at the bottom center of the bed to monitor the reaction temperature. Prior to testing the reactor was purged with 100 cc/min N_2 for 5 min and the catalyst was reduced in 100 cc/min 5% H_2/N_2 as the temperature was raised to 550 ^oC where it was held for 20 min. Catalysts were tested under two sets of feed conditions: 2.5% propane with balance N_2, and 1.7% propane, 1.7% H_2 with balance N_2. Turnover rates (TOR) were calculated from the rate of propylene production per exposed Pt atom, determined by ΔXANES, from the tests with H_2 included in the feed.

5.3.5 *In situ* Resonant Inelastic X-ray Scattering (RIXS)

RIXS measurements were performed at the MR-CAT 10-ID beamline at the APS, Argonne National Lab. Approximately 50 mg of catalyst was ground into a powder and pressed into a self-supported wafer in a stainless-steel sample holder at a 45^o angle to the incident beam. The sample holder was placed in a custom resistively-heated reactor cell through which gases could be flowed. [16] Samples were reduced at 550 ^oC in 3% H_2/He at 100 cc/min for 20 min and then cooled to 200 ^oC in the same gas flow for measurements.

A spectrometer based on the Laue geometry was used for RIXS measurements and has been described previously. [9] Briefly, a spherically bent silicon crystal analyzer was used to select the $L\beta_5$ emission line of Pt. Fluorescence X-ray were detected using a Pilatus 100k pixel area detector. Soller slits between the analyzer and detector lowered the background signal by absorbing unreflected X-rays. The entire emission spectrum was collected at each incident energy by setting the analyzer position with respect to the sample. Both the analyzer and detector positions were fixed during measurements. Each pixel of the detector was assigned an energy value which was calibrated using the elastic scattering peak from the SiO_2 support. Energy masks were created for the entire detector area and used to minimize the elastic scattering peak in the 2D intensity vs energy plots.

5.3.6 Density Functional Theory Calculations (DFT)

All electronic structure calculations are performed with periodic density functional theory using the Vienna Ab-initio Simulation Package (VASP) [17] and the Perdew-Burke-Enrzerhof

(PBE) [18] exchange-correlation functional with projector augmented wave (PAW) pseudopotentials. [19] The Pt_pv pseudopotential is used to include interactions with the 5p electrons. Spin polarization is considered for all calculations due to the unpaired electrons in Fe. Bulk Pt, Pt_3Fe, PtFe, and $PtFe_3$ FCC unit cells were converged at a 600 eV cutoff energy and a force convergence criterion of 20 meV/A. A 15x15x15 Gamma-point centered grid in k-space was used to sample the Brillouin zone. Magnetic moments of Fe atoms in each alloy were varied to converge to the lowest energy electronic configuration. Bulk lattice constants were found to be a=3.96 Å for pure Pt, a=3.91 Å for Pt3Fe, a=2.73 Å and c=3.77 Å for PtFe. For PtFe3, an elongation of the c lattice vector was observed for the lowest energy spin state which retained a FCC lattice ordering. The PtFe3 lattice vectors were found to be a=3.82 Å and 3.59 Å.

Surfaces were cleaved for each intermetallic alloy based on the lowest surface free energy. For each alloy, a 5 layer slab was constructed with the bottom 2 layers constrained to their bulk lattice positions. A 450 eV cutoff energy was used to relax each surface with a vacuum of 13 A to separate slabs. Additionally, a dipole correction in the z direction was made to reduce spurious interactions between periodic images. For pure Pt, a 2x2 (111) surface was cut based on previous reports of its stability. The Pt3Fe alloy has an FCC structure, and a 2x2 (111) surface was used for it as well. The PtFe alloy forms a tetragonal BCC lattice, and thus the (011), (110), and (101) surface terminations were considered (Appendix C), and the (011) surface was found to have the lowest surface free energy. A 2x1 (011) surface was considered to match the surface coverage of the FCC metals. A 2x2 (111) surface was used for the PtFe3 surface based on its FCC lattice structure.

RIXS spectra were calculated using the scheme discussed in previous literature. [9, 20] Ground state electronic structure calculations were performed at a 600 eV cutoff using tetrahedral smearing with Blochl corrections. The electron band structure was projected onto hybridized atomic orbitals according to their Wigner-Seitz radius. RIXS scattering peaks were calculated from the Pt d-DOS as projected from the atomic basis set. To simulate the scattering contributions from surface and bulk Pt atoms in each alloy the Pt d-DOS was a weighted average of 60% surface and 40% bulk electronic states, similar to previous RIXS simulations. [9]

5.4 Results

5.4.1 Catalyst Synthesis

Bimetallic catalysts were synthesized with nominal Fe:Pt atomic ratios of 0.7, 2.9, and 4.4 and are designated by such. For example, the Pt-Fe catalysts with a nominal Fe:Pt ratio of 0.7 is Pt-Fe(0.7). To compare the propylene selectivity and dehydrogenation rate, monometallic Pt and Fe catalysts were also synthesized. The synthesized catalysts are summarized in Table 5.1.

Table 5.1: Catalyst compositions and Fe:Pt atomic ratios

Catalyst	Pt Loading (wt. %)	Fe Loading (wt. %)	Fe:Pt atomic ratio
Pt	2	0	---
Pt-Fe(0.7)	5	1	0.7
Pt-Fe(2.9)	3	2.5	2.9
Pt-Fe(4.4)	4	5	4.4
Fe	0	10	---

5.4.2 *In situ* XAS

XAS measurements were performed at the Pt L_{III} (11.564 keV and Fe K (7.112 keV) edges to determine the average local coordination environments of Pt and Fe in the mono and bimetallic catalysts. Prior to measurements catalysts were reduced at 550 ^{o}C and spectra were collected at room temperature in He. The Pt L_{III} edge XANES of the bimetallic and monometallic Pt catalysts are shown in Figure 5.2.

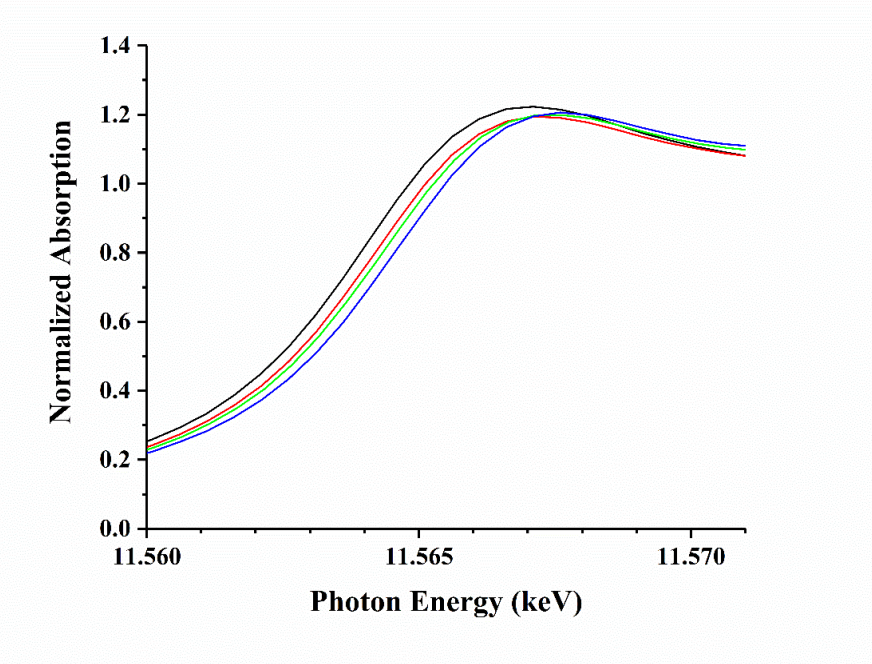

Figure 5.2: Pt L_{III} edge XANES of Pt (black), Pt-Fe(0.7) (red), Pt-Fe(2.9) (green), and Pt-Fe(4.4) (blue)

The L_{III} edge energy of the Pt catalyst (11.5640 keV, Table 5.2) is the same as the Pt foil and the slight decrease in the white line intensity is typical of small nanoparticles. [21-24] Compared to the monometallic Pt catalyst Pt-Fe(0.7), Pt-Fe(2.9), and Pt-Fe(4.4) show small increases in edge energies to 11.5642, 11.5645, 11.5646 keV, respectively (Table 5.2) with increasing loadings of Fe. The L_{III} edge XANES spectra of the bimetallic catalysts also change in shape and have a lower white line intensity than the monometallic Pt nanoparticles. The changes in energy and shape of the L_{III} edge XANES spectra of the Pt-Fe catalysts are consistent with the formation of bimetallic nanoparticles. Since the L-edge XANES probe the empty 5d states, the changes in edge energy and white line intensity indicates differences in the valance electronic structure of Pt with different Fe loadings. The Pt L_{III} edge EXAFS of the catalysts after reduction at 550 ^{o}C are shown in Figure 5.3.

Table 5.2: Pt L_{III} edge XANES and EXAFS fitting parameters after reduction at 550 °C

Catalyst	Pt L_{III} Energy (keV)	Scattering Pair	CN	R (Å)	$\Delta\sigma^2$ (x10^3)	E_o (eV)
Pt	11.5640	Pt-Pt	8.8	2.75	2.0	-0.2
Pt-Fe(0.7)	11.5642	Pt-Pt	6.1	2.73	2.0	-1.1
		Pt-Fe	2.2	2.64	5.0	-3.2
Pt-Fe(2.9)	11.5644	Pt-Pt	5.0	2.74	2.0	-1.7
		Pt-Fe	4.6	2.64	5.0	-2.0
Pt-Fe(4.4)	11.5646	Pt-Fe	8.6	2.66	5.0	-0.5

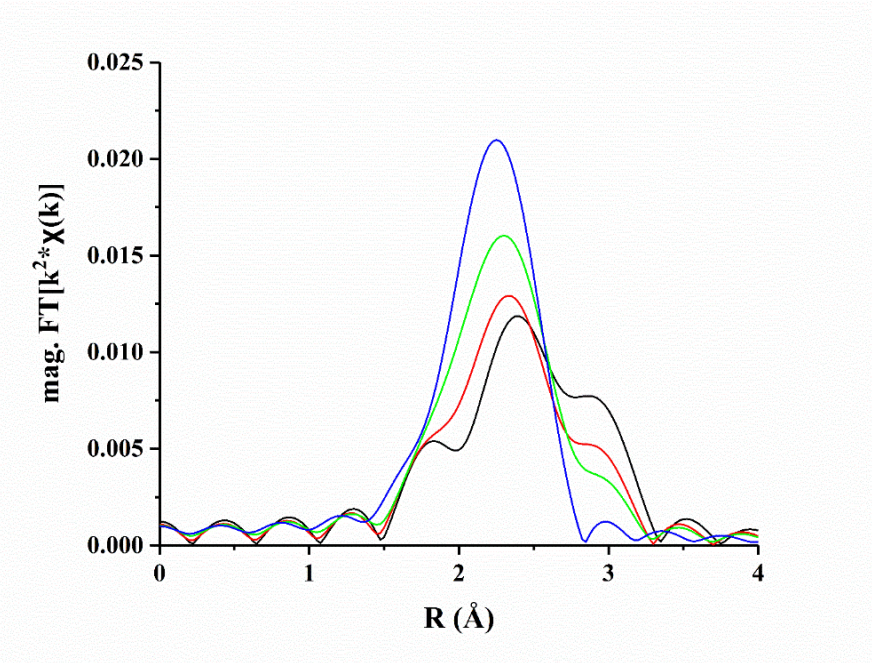

Figure 5.3: Isolated first-shell magnitude of the Fourier transform of the k^2-weighted Pt L_{III} edge EXAFS of Pt (black), Pt-Fe(0.7) (red), Pt-Fe(2.9) (green), and Pt-Fe(4.4) (blue). ($\Delta k = 3.00 - 11.40$ $Å^{-1}$)

The coordination numbers (CN) and bond distances (R) of Pt were determined from fitting of the magnitude and imaginary parts of the Fourier transform of the k^2-weighted first shell EXAFS spectra and the results are in Table 5.2. The EXAFS of the Pt catalyst shows three prominent peaks at 1.94, 2.39, and 2.86 Å (phase uncorrected distances) characteristic of Pt-Pt scattering. The Pt-Pt CN was determined to be 8.8 at a distance of 2.75 Å, values typical of small nanoparticles. [21, 25] The spectrum of Pt-Fe(0.7) shows three peaks similar to monometallic Pt; however, the second and third peaks are shifted to 2.35 and 2.84 Å (phase uncorrected distances), the first peak has

become a shoulder on the leading edge of the second, and there is a change in peak ratios. The changes in the spectrum of Pt-Fe(0.7) are consistent with the presence of non-Pt neighbors and a good fit was obtained by including contributions from Pt-Pt and Pt-Fe scattering. The Pt-Fe CN is 2.2 at a distance of 2.64 Å and the Pt-Pt CN is 6.1 at a distance of 2.73 Å, shorter than the Pt-Pt distance in monometallic Pt nanoparticles. The EXAFS of Pt-Fe(2.9) show an asymmetric peak at 2.29 Å with a shoulder at 2.84 Å (phase uncorrected distances), consistent with Pt having Pt and non-Pt neighbors like Pt-Fe(0.7). The Pt-Pt CN is 5.0, lower than Pt-Fe(0.7). However, the bond distance is 2.74 Å, similar to Pt-Fe(0.7). The Pt-Fe CN of Pt-Fe(2.9) is 4.6, larger than Pt-Fe(0.7), and at an equivalent distance of 2.64 Å. The spectrum of Pt-Fe(4.4) shows a single peak at 2.26 Å (phase uncorrected distance) which is indicative of Pt having only non-Pt neighbors and a good fit is obtained by only including a contribution from Pt-Fe scattering. The Pt-Fe CN of Pt-Fe(4.4) is 8.6 at a distance of 2.66 Å.

To estimate the metallic fraction of Fe in each catalyst, Fe K edge XANES measurements were performed. XANES spectra of the bimetallic and monometallic Fe catalysts are shown in Figure 5.4.

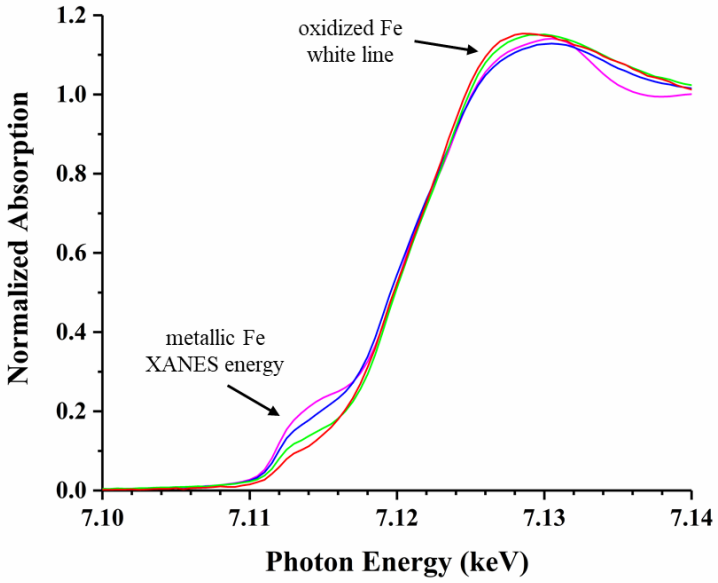

Figure 5.4: Fe K edge XANES of Pt-Fe(0.7) (red), Pt-Fe(2.9) (green), Pt-Fe(4.4) (blue), and Fe (magenta)

The shape of the Fe XANES spectrum of each catalyst at 7.112 keV is consistent with a mixture of Fe^{2+} and Fe^{0}. Linear combination XANES fits were performed to estimate the fraction of metallic iron in each sample. However, fitting the spectra with Fe foil and FeO led to unsatisfactory fits. Fe is known to form single site Fe^{2+} species on SiO_2. [26] The isolated Fe species have four Fe-O bonds rather than six, as in bulk FeO, which results in a different XANES shape. Linear combination fitting of the XANES spectra with Fe foil and isolated Fe^{2+} produced better fits, allowing for the estimation of the fraction of oxidation states in each sample, and the results are shown in Table 5.3.

Table 5.3: Fe K Edge XANES fits of bimetallic Pt-Fe and monometallic Fe catalysts (* fractions of Fe^{0} and Fe^{2+} determine from fractional coordination number of Fe-Fe scattering)

Catalyst	Fe K Edge Energy (keV)	XANES Fit	
		Fraction Fe^{0}	Fraction Fe^{2+}
Pt-Fe(0.7)	7.1195	0.29	0.71
Pt-Fe(2.9)	7.1195	0.32	0.68
Pt-Fe(4.4)	7.1195	0.46	0.54
Fe*	7.1120	0.68	0.32
Fe Foil	7.1120	---	---

Increasing the bulk Fe:Pt ratio led to a higher fraction of metallic Fe. In Pt-Fe(0.7) 29% of the Fe is metallic and the amount increased slightly to 32% in Pt-Fe(2.9). When the Fe:Pt ratio was increased to 4.4, 46% of the Fe was reduced to the metallic state. A good fit of the monometallic Fe catalyst was not obtained with either the FeO or isolated Fe^{2+} reference. The high Fe loading of this catalyst (10 wt. %) likely led to poor dispersion of the catalyst precursor on the silica support and the formation of several Fe-oxide species. Therefore, a reliable XANES fit could not be obtained. To gain insight into the local coordination environment of Fe in the bimetallic and monometallic catalysts K edge EXAFS measurements were performed and the spectra are shown in Figure 5.5.

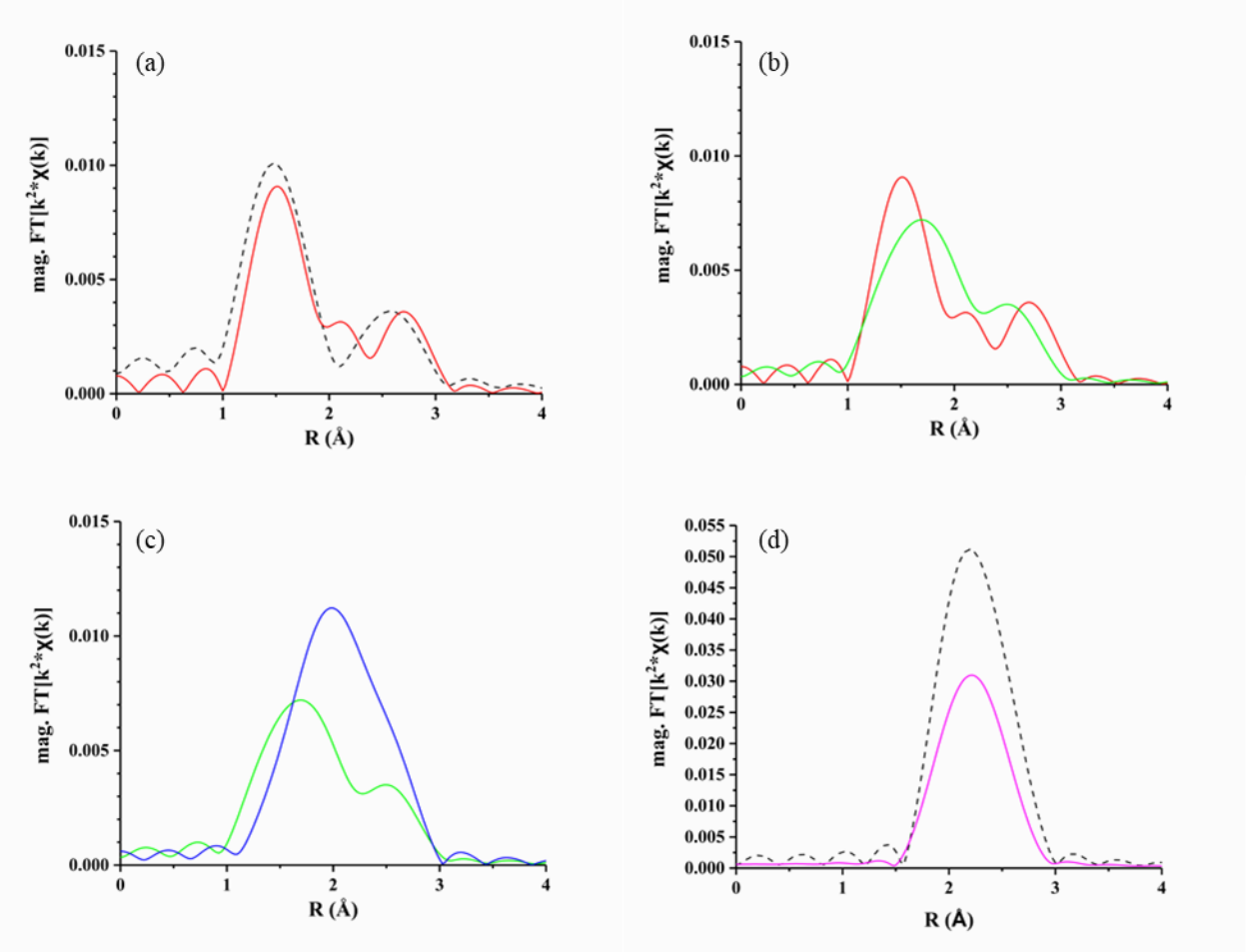

Figure 5.5: Fe K edge EXAFS of (a) Fe^{II} Single Site (dashed black) and Pt-Fe(0.7) (red), (b) Pt-Fe(0.7) (red) and Pt-Fe(2.9) (green), (c) Pt-Fe(2.9) (green) and Pt-Fe(4.4) (blue), and (d) Fe (magenta) and Fe foil (dashed black)

Figure 5.5a shows the magnitude of the Fourier transform of the k^2-weighted EXAFS of the first and second-shell scattering of isolated Fe^{2+} and the bimetallic catalysts. Due to the large number of overlapping peaks from different types of neighboring atoms, meaningful fits of the bimetallic catalysts could not be obtained, however, qualitative information can still be obtained. The spectrum of the single site catalysts shows two features at 1.48 and 2.58 Å (phase uncorrected distance) which correspond to first-shell Fe-O and second-shell Fe-O-Si scattering, respectively. Pt-Fe(0.7) shows a Fe-O scattering peak with reduced intensity compared to the single site catalyst, consistent with a fraction of Fe being in the metallic state. Also, a new peak has emerged at 2.11 Å and the peak at 2.58 Å has shifted to higher R (2.71 Å). The changes seen between 2.0 and 3.0 Å are consistent with the presence of metal-metal scattering and the Pt L_{III} edge EXAFS which

show Pt has Fe neighbors. Pt-Fe(2.9) shows further reduction in the Fe-O scattering peak compared to Pt-Fe(0.7) and increased metal-metal scattering (i.e. increased intensity between R = 2.0 and 3.0 Å). The spectrum of Pt-Fe(4.4) shows a asymmetric peak at 1.99 Å (phase uncorrected distance) consistent with a large fraction of Fe in the sample having metal neighbors. Although a fraction of the Fe remains as an oxide in Pt-Fe(4.4), the metal-metal scattering dominates the spectrum. The Fe K edge EXAFS of the bimetallic catalysts are consistent with the Fe XANES and Pt EXAFS which showed increasing amounts of metallic Fe and Pt-Fe neighbors with increasing nominal Fe:Pt ratios.

The magnitude of the Fourier transform of the k^2-weighted EXAFS of the isolated first-shell of Fe foil and the monometallic catalyst are shown in Figure 5b. The foil spectrum shows one asymmetric peak with the maximum at 2.19 Å (phase uncorrected distance). The asymmetry arises from overlapping peaks from the first and second coordination shells of bcc Fe (8 Fe at 2.48 Å and 6 Fe at 2.87 Å). The monometallic catalyst shows a similar asymmetric peak to the foil. However, the intensity of the peak is approximately 60% that of the foil. This is due to a fraction of the Fe being in the reduced state and present as large particles as seen by XRD and discussed later. As with Pt-Fe(4.4), the metal-metal scattering dominates the spectrum even though the XANES show a fraction of the Fe remains oxidized. Since only Fe-Fe scattering is visible the spectrum was fit to determine the fractional Fe-Fe coordination number and estimate the fraction of Fe in the metallic state. Fe was found to have 4.7 nearest neighbors at a distance of 2.44 Å which corresponds to approximately 58% (i.e. 4.7/8 = 0.58) of the Fe being present in the metallic state. XAS results at the Pt L_{III} and Fe K edges are consistent with the formation of bimetallic nanoparticles in the Pt-Fe catalysts. However, XAS only provides local structural information so to determine whether the bimetallic particles have a specific structure, *in situ* X-ray diffraction measurements were performed.

5.4.3 *In situ* XRD

In situ synchrotron XRD measurements were performed to determine the crystal structure of the nanoparticles in the synthesized monometallic and bimetallic catalysts. Diffraction patterns were collected at 550 ^oC in 3% H_2/He and then after cooling to 35 ^oC in the same atmosphere. The patterns collected at 35 ^oC were identical to those collected at 550 ^oC except for thermally induced lattice expansion indicating the structure of the nanoparticles does not change upon cooling.

Therefore, the patterns collected at 35°C were used to identify the crystal structure of each catalysts by comparing the experimental data to simulated patterns of known Pt-Fe alloys. To isolate the diffraction patterns of the nanoparticles the scattering from the silica support, the empty cell, and the gases in the X-ray path were subtracted from the full spectrum of each catalyst. Figure 5.6 shows the diffraction patterns of the isolated nanoparticle and the simulated patterns of the identified phases.

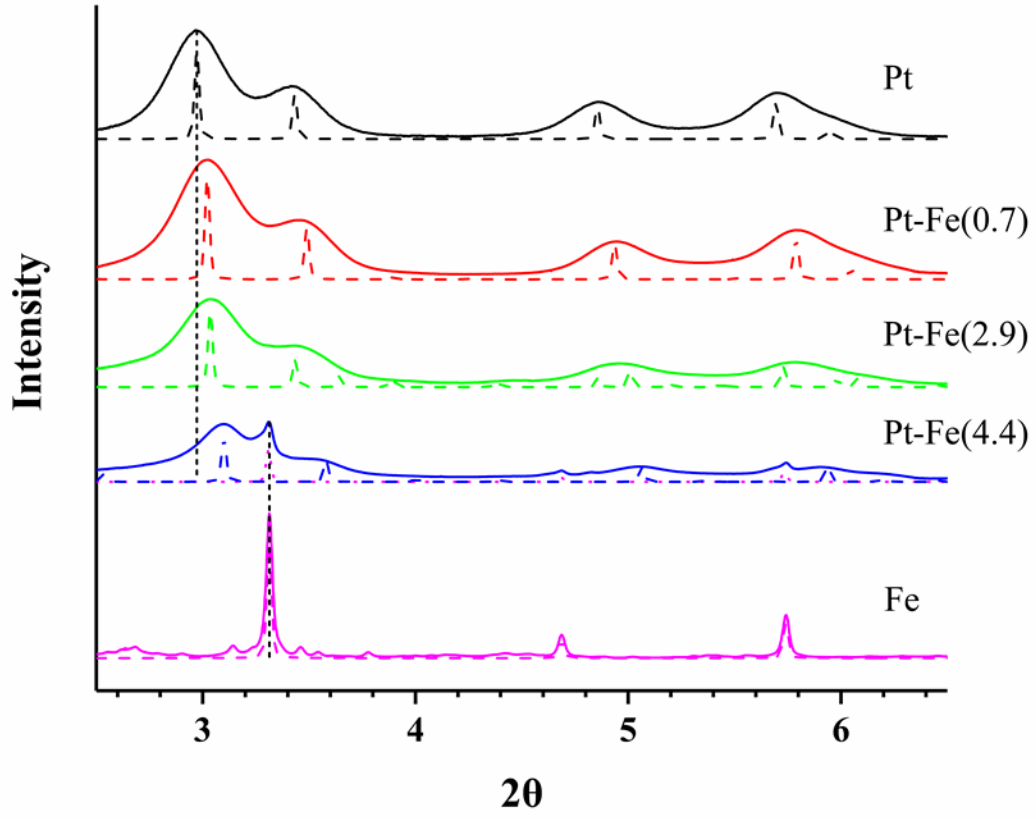

Figure 5.6: Background subtracted XRD patterns at 35 °C of the catalysts after reduction at 550 °C (Pt – black, Pt-Fe(0.7)– red, Pt-Fe(2.9) – green, Pt-Fe(4.4) – blue, and Fe – magenta) and simulated patterns of identified phases (Pt – dashed black, Pt_3Fe – dashed red, PtFe – dashed green, $PtFe_3$ – dashed blue, and α-Fe – dashed magenta).

The diffraction patterns of the Pt and three Pt-Fe catalysts show broad peaks indicative of small nanoparticles. However, there are sharp peaks in the pattern of Pt-Fe(4.4) which indicates the presence of a second phase with large crystal domains. Minimal peak broadening is observed

for the Fe catalyst consistent with the presence of large crystalline domains. The Scherrer equation was used to estimate average crystal sizes from the position and broadening of the most intense diffraction peak of each sample and the results are in Table 5.4.

Table 5.4: Crystal sizes, identified phases, and lattice parameters determined from XRD of the mono and bimetallic catalysts at 35 °C in He after reduction at 550 °C

Catalyst	Crystal Size (nm)	Crystal Phase	Lattice Constant (Å)	Bond Distance (Å)
Pt	2.1	Pt	3.92	Pt-Pt: 2.77
Pt-Fe(0.7)	1.8	Pt_3Fe	3.86	Pt-Pt/Fe: 2.73
Pt-Fe(2.9)	1.9	PtFe	a: 2.77 c: 3.67	Pt-Fe: 2.68 Pt-Pt: 2.77
Pt-Fe(4.4)	2.2	$PtFe_3$ + α-Fe	$PtFe_3$: 3.76 α-Fe: 2.87	Pt-Fe: 2.66 Fe-Fe: 2.49
Fe	48	α-Fe	2.87	2.49

The average crystal size of the Pt catalyst determined from XRD is 2.1 nm. The crystal sizes of Pt-Fe(0.7) (1.8 nm), Pt-Fe(2.9) (1.9 nm), and Pt-Fe(4.4) (2.2 nm) are similar to the monometallic Pt catalysts. Due to peak overlap the size of the second phase in Pt-Fe(4.4) was not determined from the Scherrer equation. However, the sharpness of the peaks suggests the phase is present as large crystalline domains. The average particle size in the Fe catalyst determined from the Scherrer equation is 48 nm. The similar particle sizes and peak broadening of the Pt and Pt-Fe catalysts suggests that the decrease in peak intensity seen with increasing Fe:Pt ratio is due to an increase in the amount of Fe present in the detected crystal structures. The isolated diffraction patterns of each catalyst were compared to simulations of known intermetallic phases to determine the structure of the nanoparticles present in each sample. Figure 5.7 shows the crystal structures of the phases identified in the bimetallic catalysts as well as monometallic Pt and Fe.

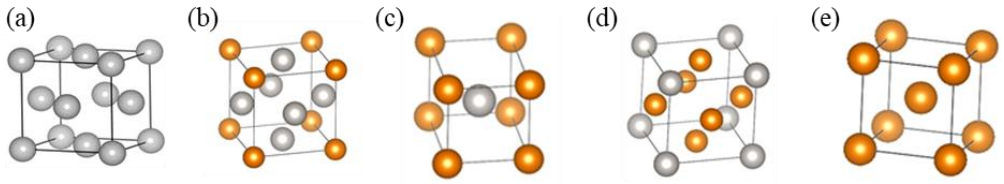

Figure 5.7: Unit cells of the crystal structures present in the mono and bimetallic catalysts determined from XRD: (a) Pt, (b) Pt_3Fe, (c) PtFe, (d) $PtFe_3$, and (e) α-Fe (Pt – silver, Fe – orange) [27-30]

The diffraction pattern of the monometallic Pt catalyst is characteristic of FCC Pt with peaks at 2.973° and 3.415° corresponding to the (111) and (200) reflections respectively. The small 2θ angles are due to the high energy (105 keV) of the synchrotron X-rays. The lattice constant and Pt-Pt bond distance calculated from Bragg's law are 3.92 and 2.77 Å, respectively (Table 5.4). Pt-Fe(0.7) has a similar diffraction pattern to the monometallic Pt catalyst, however all the peaks are shifted to higher 2θ indicating a decrease in the lattice constant. The diffraction pattern matches that of the Pt_3Fe alloy with a Cu_3Au structure with the most intense peaks at 3.021° and 3.449° corresponding to the (111) and (200) reflections. The calculated lattice constant is 3.86 Å corresponding to an average Pt-M bond distance of 2.73 Å. The diffraction pattern of Pt-Fe(2.9) is similar to Pt-Fe(0.7), however the peak positions of the four most intense peaks are shifted. The first and third peaks are shifted to higher angle (3.040° and 4.961°) while the second and fourth peaks are shifted to lower angle (3.432° and 5.786°) compared to Pt-Fe(0.7). The pattern of Pt-Fe(2.9) matches that of the PtFe alloy with a AuCu structure with the peaks at 3.040° and 3.432° corresponding to the (101) and (110) reflections. The shift to higher angle of the first and third peaks and to lower angle of the second and fourth peaks is due to PtFe having a tetragonal unit cell rather than cubic like the Pt_3Fe phase. The lattice constants *a* and *c* determined from Bragg's law are 2.77 and 3.67 Å, respectively, which corresponds to a Pt-Fe bond distance of 2.68 Å. The broad peaks in the diffraction pattern of Pt-Fe(4.4) are shifted towards lower angles compared to those of Pt-Fe(2.9) indicating a decrease in the lattice constant. The broad peaks in the pattern result from the $PtFe_3$ alloy phase with a $AuCu_3$ structure with the peaks at 3.099° and 3.527° corresponding to the (111) and (200) reflections. The lattice constant and Pt-Fe bond distance calculated from Bragg's law are 3.76 and 2.66 Å, respectively. The diffraction pattern of Pt-Fe(4.4) shows sharp peaks at 3.311°, 4.687°, and 5.742° in addition to the broad peaks from the alloyed nanoparticles. The sharp peaks arise from the presence of monometallic α-Fe with most intense

peak at 3.311° corresponding to the (110) reflection. The calculated lattice constant of the monometallic Fe phase is 2.87 Å, equivalent to that reported for bulk α-Fe. The most prominent peaks in the diffraction pattern of the monometallic Fe catalyst correspond to α-Fe, with the peak at 3.312° corresponding to the (110) reflection, and having a lattice constant of 2.87 Å. The other peaks in the diffraction pattern appear to be from different species of Fe-oxide. However, comparison of the experimental spectrum to simulations of FeO, Fe_3O_4, and Fe_2O_3 did not provide a satisfactory match to a single phase. This suggests that the remaining oxidized Fe is present as a mixture of species which is consistent with the Fe K edge XANES results. *In situ* XRD results reveal that Pt and Fe form ordered intermetallic alloys in bimetallic nanoparticles and that the exact structure depends on the Fe:Pt atomic ratio.

5.4.4 Catalyst Testing

To study the effect of crystal structure on reactivity the catalysts were tested for propane dehydrogenation at 550 °C. Figure 5.8 shows the effect of increasing conversion on propylene selectivity for the catalysts tested using a reaction feed of 2.5% propane in nitrogen.

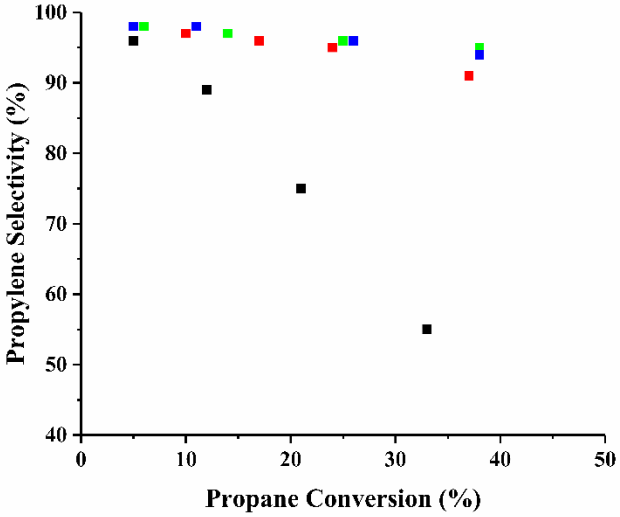

Figure 5.8: Initial propylene selectivity as a function of propane conversion of Pt (black), Pt-Fe(0.7) (red), Pt-Fe(2.9) (green), and Pt-Fe(4.4) (blue). (Reaction feed 2.5% C_3H_8, balance N_2)

The propylene selectivity of the Pt catalyst dropped from 90% to 55% as the propane conversion was increased from 10% to 30%. The decrease in selectivity can be attributed to the increased hydrogen concentration resulting from higher propane conversions facilitating hydrogenolysis. Under the testing conditions the Fe catalyst showed no propane conversion. At 10% conversion Pt-Fe(0.7), Pt-Fe(2.9), and Pt-Fe(4.4) were 97, 98, and 98% selective for propylene. However, at 40% the three alloy catalysts were 91, 95, and 94% selective, much higher than monometallic Pt. The large difference in selectivity between the Pt and Pt-Fe catalysts at high conversion indicates that the alloys will preferentially perform dehydrogenation rather than hydrogenolysis even in the presence of hydrogen. To better study the effect of H_2 on propylene selectivity the catalysts were tested for propane dehydrogenation with a feed containing equal molar amounts of H_2 and C_3H_8 (1.7% H_2, 1.7% C_3H_8, balance N_2). Figure 5.9 shows the effect of H_2 on the initial propylene selectivity at different propane conversions.

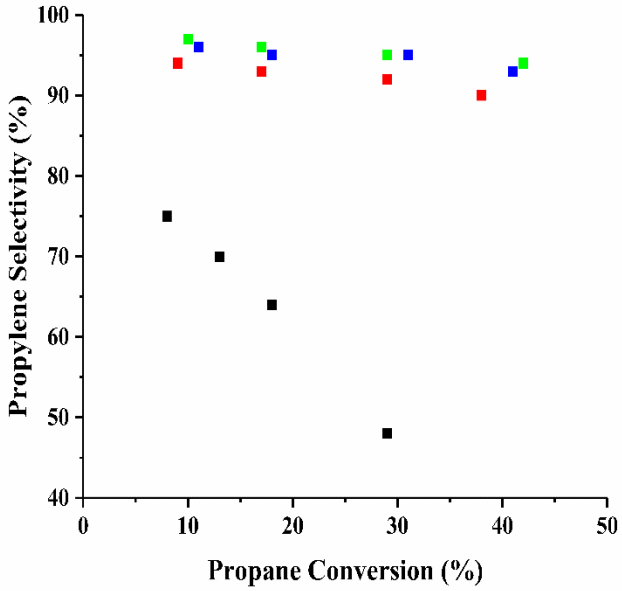

Figure 5.9: Initial propylene selectivity as a function of propane conversion of Pt (black), Pt-Fe(0.7) (red), Pt-Fe(2.9) (green), and Pt-Fe(4.4) (blue). (Reaction feed 1.7% C_3H_8, 1.7% H_2, balance N_2)

When H_2 was included in the reaction feed Pt catalyst showed a drop in propylene selectivity from 75% to 48% as the propane conversion was increased from 10% to 30%. When

H_2 was added to the reaction feed the Fe catalyst still showed no propane conversion. At 10% conversion with H_2 in the feed Pt-Fe(0.7) (94%), Pt-Fe(2.9) (96%), and Pt-Fe(4.4) (97%) maintained high selectivity for propylene. Even at 40% the three alloy catalysts were 90%, 93%, and 94% selective, only a slight decrease compared to 10% conversion. Propane dehydrogenation results show that even in the presence of hydrogen the alloy catalysts preferentially perform dehydrogenation. Since the monometallic Fe catalyst showed no activity at 550 ^oC it is believed that Pt is the active site for propane dehydrogenation in the alloy catalysts. Propylene production rates per gram of Pt were measured at 10% conversion with H_2 in the feed for the Pt and alloy catalysts and the results are in Table 5.5.

Table 5.5: Propylene selectivity at 10% conversion and propane dehydrogenation rates

Catalyst	Propylene Selectivity at 10% Conversion		Propylene Production Rate with H_2 (mol/g Pt-s)
	Without H_2	With H_2	
Pt	90%	75%	0.40
Pt-Fe(0.7)	97%	94%	0.71
Pt-Fe(2.9)	98%	96%	0.70
Pt-Fe(4.4)	98%	97%	0.45

The propylene production rate of the monometallic catalyst was 0.40 mol propylene/g Pt-s. The rates of Pt-Fe(0.7), Pt-Fe(2.9), and Pt-Fe(4.4) are 0.71, 0.70, and 0.45 mol/g Pt-s, similar to that of the monometallic catalyst. The L_{III} edge XANES show differences in the electronic structure of the valance states of Pt in each alloy phase. Therefore, to determine how the crystal structure effects the reactivity of Pt, rates must be normalized by the number of active sites to obtain turnover rates.

5.4.5 Pt L_{III} Edge ΔXANES

To quantify the fraction of surface Pt present in the alloy catalysts ΔXANES measurements were performed at the Pt L_{III} edge. Traditionally CO chemisorption measurements are used to determine the fraction of exposed Pt atoms in supported nanoparticle catalysts. However, Fe is known to chemisorb CO so the measured uptake on the alloy catalysts could be a convolution of adsorption of both metals. [31-35] Pt surface areas can also be measured by O_2-H_2 titration. [36]

In this method the exposure of reduced Pt particles to air results in oxidation of the surface layer to PtO. Upon exposure to H_2 the PtO layer is reduced to the metallic state and chemisorbs H_2. Modified O_2-H_2 titration methods have been reported for Pt-Fe catalysts, but assumptions are made about the quantities of gases consumed by metallic and oxidized Fe. [79-38] Therefore, an element specific technique which allows for the quantification of PtO is desirable.

Oxidation of metallic Pt increases the edge energy and white line intensity of the Pt L_{III} edge XANES (Figure C.2). The composition of a binary mixture can be determined from a linear combination fit of the XANES spectrum, but without references for the PtO shell and the Pt core reliable fits of the oxidized nanoparticles cannot be obtained. However, the changes can be isolated by taking the difference of the XANES spectra of the catalyst in the oxidized and reduced states. This approach has been used to determine the surfaces coverages on Pt of various adsorbed species during water-gas shift [39] and electro-chemical reactions [40]. The intensity of the difference spectrum is proportional to the amount of PtO formed upon oxidation, with increasing intensity corresponding to higher fraction of Pt^{2+}, and since only the surface of the particles is oxidized the fraction of PtO is equivalent to the Pt dispersion. Using Pt nanoparticles of different sizes, the correlation between dispersion and ΔXANES intensity can be determined (Figure C.3). Assuming only surface Pt is oxidized in the alloy nanoparticles the determined correlation can be used to determine the dispersion of the bimetallic catalysts, allowing for the determination of TORs. Figure 5.10 shows the ΔXANES spectra of the three alloy catalysts.

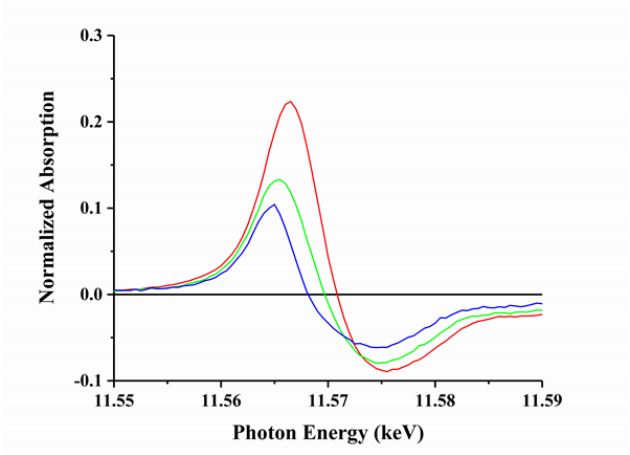

Figure 5.10: Pt L_{III} edge ΔXANES spectra of Pt-Fe(0.7) (red), Pt-Fe(2.9) (green), and Pt-Fe(4.4) (blue)

The reduction in ΔXANES intensity with increasing Fe content of the alloy indicates a decrease in Pt dispersion as the phase becomes more Fe rich. The ΔXANES intensities of Pt-Fe(0.7), Pt-Fe(2.9), and Pt-Fe(4.4) are 0.224, 0.133, and 0.104 (Table 5.6). These values correspond to dispersion values of 34%, 20%, and 16% for Pt-Fe(0.7), Pt-Fe(2.9), and Pt-Fe(4.4), respectively. From the measured dispersions TORs can be calculated and the results are given in Table 5.6.

Table 5.6: ΔXANES intensities, Pt dispersions, and TOR of Pt and the three alloy catalysts.

Catalyst	ΔXANES Intensity	Pt Dispersion	Apparent TOR (s^{-1})
Pt	---	28%	0.21
Pt-Fe(0.7)	0.224	34%	0.41
Pt-Fe(2.9)	0.133	20%	0.69
Pt-Fe(4.4)	0.104	16%	0.55

All three alloys have higher TOR than monometallic Pt. The TOR also varied with the crystal structure of the alloy. The formation of Pt_3Fe in Pt-Fe(0.7) led to an increase in TOR to 0.41 s^{-1} from 0.21 s^{-1} in monometallic Pt. Changing the crystal structure to PtFe in Pt-Fe(2.9) further increased the TOR to 0.69 s^{-1}.The addition of more Fe in Pt-Fe(4.4) and the formation of $PtFe_3$ led to a decrease in the TOR (0.55 s^{-1}) compared to Pt-Fe(2.9). However, the TOR of the $PtFe_3$ phase was higher than that of Pt_3Fe. The changes in TOR with alloy phase are indicative of electronic changes to Pt and in agreement with the L edge XANES results.

5.4.6 Pt L_{III} Edge RIXS

The observed enhancements in propane dehydrogenation rates of the alloys compared to Pt are believed to arise from the changes to the 5d states seen in the L edge XANES. To further investigate the changes to the valance states of Pt upon alloying *in situ* resonant inelastic x-ray scattering measurements were performed. Measurements of the L_{III} absorption edge and the $L\beta_5$ emission line give the energies of the unfilled and filled valance states of Pt, respectively, which are responsible for chemical reactivity. RIXS measurements were performed on the Pt and alloy catalysts after reduction at 550 ^oC and the results are in Figure 5.11.

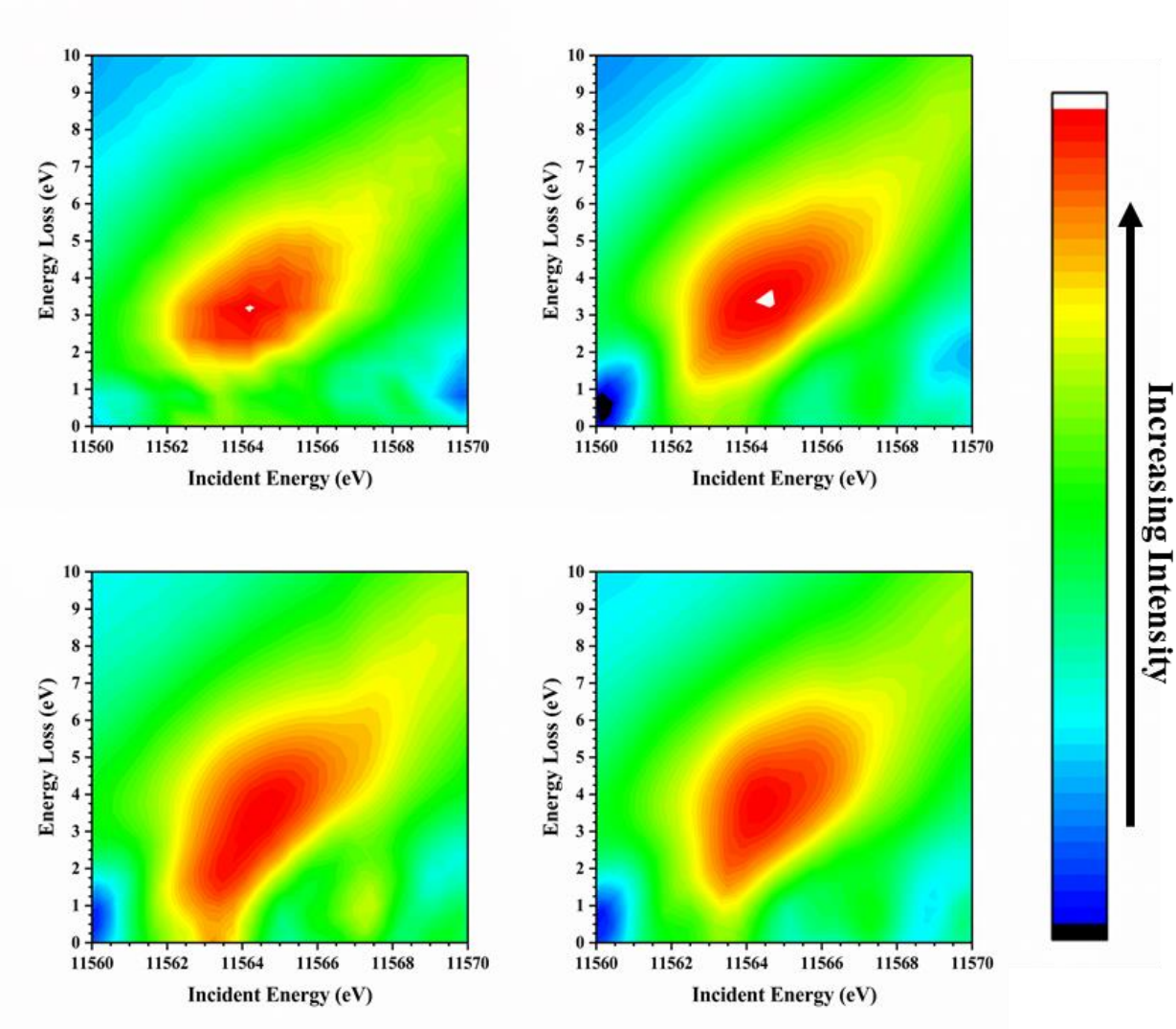

Figure 5.11: L_{III} RIXS planes of Pt (top left), Pt-Fe(0.7) (top right), Pt-Fe(2.9) (bottom left), and Pt-Fe(4.4) (bottom right)

The 2-D RIXS maps show the incident photon energy (x-axis) and energy loss (y-axis) versus the intensity of emitted photons. The position of the maximum intensity along the incident energy axis corresponds to the average energy of the unfilled valance states of Pt. The energy loss axis gives the energy difference between the incident and emitted photons, which equals the energy difference between the unfilled and filled valance states, and the location of the maximum intensity can be used to determine the average energy of the filled 5d states. The incident energy and energy loss values corresponding to the peak maximum in each catalyst are given in Table 5.7.

Table 5.7: Position of most intense feature in RIXS planes of Pt and Pt-Fe alloy catalysts.

Catalyst	Incident Energy (eV)	Energy Loss (eV)
Pt	11564.2	3.1
Pt-Fe(0.7)	11564.4	3.4
Pt-Fe(2.9)	11564.5	3.6
Pt-Fe(4.4)	11564.6	3.8

The maximum RIXS intensity of the Pt catalyst occurs at an incident energy of 11564.2 eV and an energy loss of 3.1 eV. When the Pt_3Fe phase is formed in Pt-Fe(0.7) the maximum RIXS intensity shifts to higher incident energy, 11564.4 eV, and higher energy loss, 3.4 eV. Further increases in the incident energy and energy loss to 11564.5 and 3.6 eV, respectively, are observed when the PtFe phase is formed in Pt-Fe(2.9). The $PtFe_3$ structure formed in Pt-Fe(4.4) shows the maximum incident energy, 11564.6 eV, and energy loss, 3.8 eV, of the four catalysts. RIXS measurements show that the valance electronic states of Pt are dependent upon the composition of the alloy. As the Fe content of the alloy increases there is a continual upward shift of the unfilled 5d states. This is accompanied by an increase in the energy loss due to a decrease in the energy of the filled states. While the RIXS can provide evidence of shifts of the Pt electronic states upon alloy formation, DFT calculations can corroborate the experimental results and provide additional insight into the electronic structure of alloyed platinum.

5.4.7 RIXS modeling and catalyst electronic structure

RIXS planes calculated from ground state periodic DFT capture the broad characteristics of the experimental spectra (Appendix C), however we are primarily interested in the relative high intensity peak position due to the similarities between each alloy. To extract high intensity peak positions from calculated spectra, a Lorentzian function was fitted to obtain the maxima under experimentally relevant conditions. The electron density of states as calculated correspond to 0 K, and a Lorentzian broadening of the experimental scattering signal is expected.

Table 5.8: Calculated high intensity RIXS peaks

Catalyst	Incident Energy (eV)[1]	Energy Loss (eV)
Pt	0.7	3.3
Pt-Fe(0.7)	0.9	3.4
Pt-Fe(2.9)	1.2	4.2
Pt-Fe(4.4)	1.4	5.0

[1]Incident energy is relative to the Fermi energy

Calculated incident and energy loss peaks correlate closely with experimental spectra for Pt and Pt_3Fe. The two higher Fe compositional alloys follow the same trends as experimental spectra, however, the magnitude of change relative to Pt is larger for both incident energy and energy loss than seen experimentally. The Pt density of states (DOS) used to model each spectra is shown in Figure 5.12. The DOS shows a shift in the occupied and unoccupied Pt *d*-electrons upon alloying with Fe. As the relative Fe abundance in the alloy increases, there is a upwards shift in the mean energy levels of the unoccupied electronic states with a corresponding downward shift in the mean energy levels of the occupied electronic states.

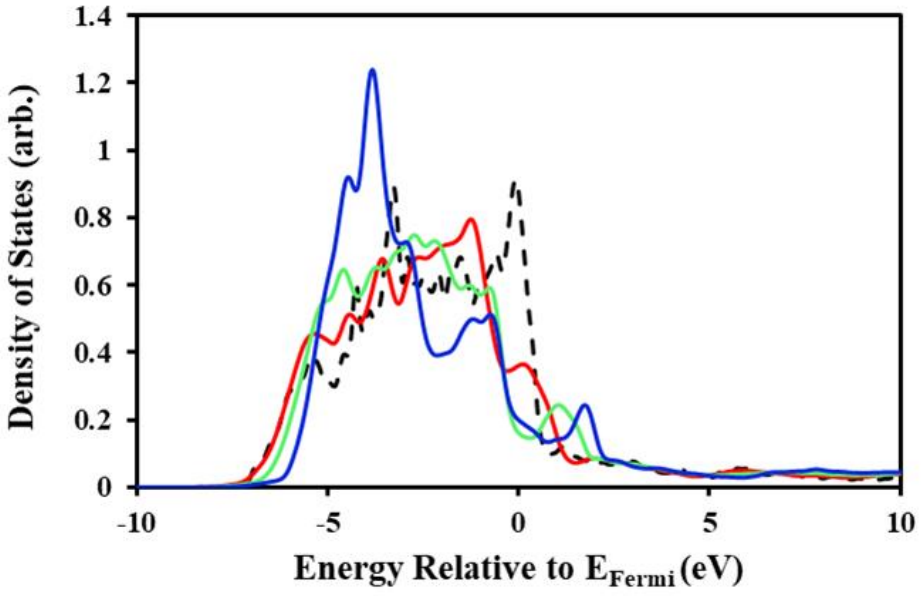

Figure 5.12: Projected density of states for Pt *d* electrons in Pt and the three Pt-Fe intermetallic compound phases. Pt – dashed black, Pt_3Fe – solid red, PtFe – solid green, $PtFe_3$ – solid blue

Binding energies of CO was used as a probe of the relative heats of adsorption of each alloy. A comparison of binding energies is provided in Table 5.9. CO adsorption onto the alloys is weaker than pure platinum and decreases as the abundance of Fe increases. We note, however, that the change in CO binding is relatively small for each alloy composition. For a detailed description of the adsorption configurations considered, see Appendix C.

Table 5.9: Calculated CO binding energies on each metal surface

Catalyst surface	CO binding energy [eV]
Pt(111)	-1.78
Pt_3Fe(111)	-1.58
PtFe(011)	-1.54
$PtFe_3$(111)	-1.48

5.5 Discussion

The addition of Fe to the Pt catalyst led to the formation of all three Pt-Fe alloys shown the in the bulk phase diagram. With increasing Fe loading, the intermetallic alloy becomes increasingly Fe-rich. The catalyst with a bulk Fe:Pt ratio of 0.7 formed the Pt_3Fe phase with a Cu_3Au structure. The Pt_3Fe phase has the same structure as the Pt_3Sn and Pt_3In alloy catalysts which have been reported to be selective for light alkane dehydrogenation. [2-6] Increasing the Fe:Pt atomic ratio to 2.9 led to the formation of the PtFe alloy with a AuCu structure. PtFe has a tetragonal unit cell and is equivalent in structure to the PdZn and PtZn alloys that has been reported to be selective for propane dehydrogenation. [7-9] Further increase in the Fe:Pt ratio to 4.4 led to the formation of small nanoparticles with the $PtFe_3$ phase with a $AuCu_3$ structure and large unalloyed α-Fe. Pt catalysts with In and Sn have been reported to form promoter rich phases with CaF_2 structures, which have been reported to be highly selective alkane dehydrogenation. Although the Pt-In and Pt-Sn alloys have different bulk structures, the local coordination environment of Pt is similar to the $PtFe_3$ phase (i.e. Pt only having promoter metal nearest neighbors). [2, 6, 41]

Since catalysis is a surface phenomenon determination of the surface structure of the bimetallic nanoparticles is crucial for understanding changes in reactivity. Segregation of metals

to the surface layers in bimetallic systems have been reported from both experimental [42-45] and theoretical studies [46-49] and can be induced by either adsorbates or high temperature annealing. To investigate the surface structure of the IMC nanoparticles Pt L_{III} edge ΔEXAFS spectra of the bimetallic catalysts were examined. By taking the difference of the EXAFS of the samples after reduction and oxidation the local structure of surface Pt atoms in the bimetallic particles can be determined. Fitting of the ΔEXAFS spectra gives Pt-Pt:Pt-Fe coordination number ratios consistent with those for the reduced samples (see Appendix C) suggesting the surface structures of the IMC nanoparticles are the same as the bulk. To determine whether any structural changes occur at high temperature the diffraction patterns of the bimetallic catalysts at 600 ^{o}C in 3% H_2/He were compared to those collected at 35 ^{o}C in the same gas environment. Although XRD is a bulk characterization technique, surface structural changes of small nanoparticles can be observed via synchrotron XRD. [50] Therefore, for the small nanoparticles (~2.5 nm) in the IMC catalysts where ~40% of the atoms are on the surface any changes due to segregation should be observed in the diffraction pattern. Upon comparison it can been seen that the patterns collected at 35 and 600 ^{o}C are identical, aside from thermally induced lattice expansion, indicating no major changes to the structure of the IMC nanoparticles (see Appendix C). Results from ΔEXAFS and high temperature XRD support the reactive surfaces of the IMC nanoparticles being identical in structure to the bulk and stable at high temperatures in a reducing H_2 atmosphere, similar conditions to propane dehydrogenation.

Although Pt and Fe are both active for alkane dehydrogenation and hydrogenolysis the intermetallic alloy catalysts exhibit behavior different from either metal. When tested for propane dehydrogenation at 550 ^{o}C with a feed containing 2.5% C_3H_8 in N_2 all three IMC catalysts were greater than 97% selective towards propylene at 10% conversion, higher than Pt which was 90% selective. Under these conditions Fe showed no propane conversion. As the propane conversion was increased the alloy catalysts maintained high propylene selectivity (>90%) while that of Pt decreased to 55%. Addition of H_2 to the reaction feed magnified the differences between the Pt-Fe and monometallic catalysts. The three Pt-Fe catalysts maintained propylene selectivities above 90% as the conversion was increased from 10 to 40%. A similar trend to having no H_2 in the reaction feed was observed for the Pt catalyst with the propylene selectivity decreasing from 75 to 48% as the conversion was increased from 10 to 30%. These results show that the IMC catalysts

preferentially activate C-H bonds, even in the presence of H_2. This is in contrast to Pt which activates both C-H and C-C bonds and Fe which displayed no catalytic activity, at least at 550 ^oC.

While the Fe catalyst showed no propane conversion at 550 ^oC, 3 nm Fe nanoparticles have been reported to be active for dehydrogenation at 650 ^oC. However, the reported catalysts were only 14% selective for propylene and rapidly deactivated. [26] Due to the reported activity of Fe, the monometallic Fe catalyst was tested for propane dehydrogenation at 600 ^oC with a feed of 1.7% C_3H_8 and 1.7% H_2 balanced in N_2. After increasing the temperature to 600 from 550 ^oC the Fe catalyst showed very low propane conversions. While this could be due to a small fraction of metallic Fe being exposed, resulting from the large particle size, when the propane consumption rate was normalized per mole of surface atoms it was found to be approximately two orders of magnitude lower than the Pt containing catalysts. At the elevated temperature the catalyst was found to almost exclusively produce coke, in agreement with the reported behavior of the smaller nanoparticles. The large differences in activity and selectivity of Fe and Pt support the later behaving as the active site for propane dehydrogenation at 550 ^oC. After identification of the active site, normalization of rates by the number of exposed Pt atoms revealed that the IMC catalysts also have higher apparent TOR than Pt in addition to being more selective.

Pt/Fe_2O_3-Al_2O_3 catalysts have been reported to be more selective and active for isobutane dehydrogenation than Pt/Al_2O_3.The increased selectivity and activity were proposed to arise from geometric and electronic effects, respectively. It was believed that the partial coverage of Pt by reduced FeO_x species decreased the hydrogenolysis activity of the Pt/Fe_2O_3-Al_2O_3 compared to Pt/Al_2O_3. The increased activity was attributed to the donation of electrons to Pt from Fe due to the formation of bimetallic particles leading to enhanced olefin desorption. [10]

The increased olefin selectivities observed for the IMC catalysts are consistent with the previously reported catalysts, however, no evidence of surface Fe oxide layers were observed in this work. Under the high temperature and reducing reaction environment of propane dehydrogenation the presence of oxide layers on the metallic Pt-Fe surface seems unlikely. The increased propylene selectivity compared to the monometallic catalysts is believed to arise from the geometric changes to Pt upon the formation of the intermetallic compound structures rather than the coverage of active sites by an oxide layer. IMC catalysts containing either Pt or Pd and a post-transition metal have been reported to be highly selective for alkane dehydrogenation. [6-9, 51] The increased olefin selectivity has been attributed to the elimination of large active-metal

ensembles by incorporation of the noncatalytic promoter metals into the active surface. Segregation of the active atoms reduces C-C bond cleavage which is thought to require ensemble active sites. The local coordination geometries of Pt in Pt_3Fe, PtFe, and $PtFe_3$ are equivalent to those in the highly selective post-transition metal IMC catalysts. Although Pt and Fe both perform dehydrogenation and hydrogenolysis, Fe catalyzes the reactions at much lower rates than Pt. Due to this large difference in the activity of the two metals Fe behaves as an inert diluent, similar to the non-catalytic post-transition elements, resulting in the small Pt ensembles in the IMC structures being highly selective for dehydrogenation. These results support the proposal that geometric, rather than electronic, changes to active sites upon alloy formation are the dominant effect leading to higher olefin selectivities in LAD reactions.

While geometric effects are believed to be the dominant factor dictating increased selectivity, alloying also changes the electronic properties of metals, as seen by differences in the apparent TOR. The observed changes with alloy composition indicates changes to the Pt 5d states which are responsible for the activation of reactants and bonding with intermediates. The Pt L_{III} edge XANES show changes to the unfilled valance states, however, to better understand the electronic effects of alloying a complete description of all 5d-states is necessary. *In situ* RIXS measurements of the Pt L_{III} edge were conducted to gain further insight into the changes to the unfilled as well as the filled valance states. The results show there is an upward shift in the average energy of the unfilled 5d states of Pt, consistent with the L_{III} edge XANES. This is accompanied by a concomitant downward shift in the average energy of the filled valance states. As the Fe content of the phase is increased (i.e. Pt-Pt bonds are lost and Pt-Fe bonds are formed), larger changes in the valance states are observed. Upon formation of Pt_3Fe there is a small shift in the valance states, then a slightly larger shift in PtFe, and finally the largest change in $PtFe_3$. The DFT RIXS planes calculated from the projected DOS of Pt show a similar trend to the experimental results. Inspection of the DOS shows as the Fe content is increased there is a reduction in the number of filled and unfilled states near the Fermi edge as well as increases in the number of lower and higher energy states. Integration of the Pt *d*-DOS shows no large change in the number of Pt d-electrons (Appendix C). It is believed that this change in the average energy of the 5d-state, rather than the typically proposed transfer of electrons, is the dominant electronic effect on Pt of alloying and are responsible for the changes in apparent TOR.

A PtZn 1:1 intermetallic compound catalyst with the same AuCu structure type as PtFe has been reported to be highly selective for ethane dehydrogenation. [9] *In situ* RIXS measurements revealed upward and downward shifts of approximately ~1 eV of the unfilled and filled 5d states of Pt upon the formation of the PtZn alloy, much larger than those seen in the 1:1 PtFe phase. Also, of note is that changing the promoter metal from Fe to Zn has a much larger effect on the valance states than changing the stoichiometry of the alloy phase. These large differences in the electronic structure of selective catalysts further supports the proposal of geometric changes being the dominant factor in increasing dehydrogenation selectivity. Interestingly, although metallic Fe has an unfilled d-shell the directionality of the shifts in the valance states measured by RIXS are the same as those observed for Zn which has a full d-shell in the metallic state. Similar changes have also been reported for bimetallic Pt-Sn catalysts, however, the exact structure was not determined. [52] The results of the current study in combination with those reported for the Pt-Zn and Pt-Sn catalysts suggest that the valance states of catalytic metals can be selectively tuned by alloying and that the effect of changing the promoter is large while that of changing stoichiometry is subtler.

The changes in the energy of the valance states measured by RIXS would lead to less energetic overlap between the 5d states of Pt and the orbitals of adsorbates which would result in weaker chemical bonds. It has been reported that CO, a common probe molecule, adsorbs weaker on bimetallic Pt-Fe nanoparticles than monometallic Pt. [53-55] The Blyholder model suggests that the dominant factor dictating the chemisorption of CO to metal surfaces is the back donation of electrons from the valance d-states to the π^* orbitals of CO. [56] It is hypothesized that lowering the energy of the filled 5d states of Pt would reduce back donation, resulting in weaker heats of adsorption. The heats of adsorption of CO on Pt and the three Pt-Fe alloy surfaces were calculated from DFT to test this prediction. The results show decreasing Pt-C bond strengths with increasing Fe content of the alloy, as would be expected from the RIXS results. Similar results have been reported for ethylene adsorption on Pt-Zn catalysts where it was found that the binding energy decreased with increasing Zn content of the alloy. [57] This weakening of metal-adsorbate bonds likely effects surfaces coverages and reaction barriers resulting in differences in apparent TOR. Although the changes seen between Pt and the three Pt-Fe IMC catalysts reported here are small, these effects could potentially play a larger role in other catalytic reactions of interest.

5.6 Conclusions

Nanoparticles of three different intermetallic compound phases were formed in bimetallic Pt-Fe catalysts: as the nominal Fe:Pt atomic ratio was increased first the Pt_3Fe phase was formed, then the PtFe phase, and lastly the $PtFe_3$ phase. Characterization results suggest that the surface structures of the IMC nanoparticles are identical to the bulk. All three catalysts where IMC phases were formed were found to be more selective for propane dehydrogenation than a monometallic Pt catalyst. Under the same testing conditions, a monometallic Fe catalyst showed negligible activity compared to the Pt containing catalysts. Geometric changes to the surface of the nanoparticles are thought to be the dominant factor leading to increased olefin selectivity. Due to the large difference in activity between Pt and Fe, the latter behaves as an inert diluent, and the formation of the IMC surfaces eliminates large ensemble of active Pt atoms which suppresses C-C bond cleavage. In addition to increased propylene selectivities the IMC catalysts showed higher TOR, which also varied with phase, indicative of changes to the valance electronic structure of Pt due to alloying. *In situ* RIXS measurement and DFT calculations reveal that when Pt is alloyed with Fe there are upward and downward shifts in average energies of the unfilled and filled 5d states, respectively, and that as the IMC phase becomes more Fe rich the magnitude of the shifts increases. It is believed that these changes in energy, rather than the commonly proposed transfer of electron density, are responsible for the observed changes in the catalytic properties of metals upon alloying. Weakening of metal – adsorbate bonds arising from these energy changes are proposed to lead to the increases in apparent TOR. From the electronic structure characterizations reported here it appears possible to tune the catalytic properties of metals by changing the alloy stoichiometry in addition to the promoter metal, as is commonly done.

5.7 Acknowledgement

This chapter is based upon work supported in part by the National Science Foundation under Cooperative Agreement No. EEC-1647722. Any opinions, findings and conclusions or recommendations expressed in this material are those of the author(s) and do not necessarily reflect the views of the National Science Foundation. Use of the Advanced Photon Source is supported by the U.S. Department of Energy, Office of Science, and Office of Basic Energy Sciences, under Contract DE-AC02-06CH11357. MRCAT operations are supported by the Department of Energy

and the MRCAT member institutions. We also acknowledge the use of the 11-ID-C beamline, part of the X-ray Science Division, at the Advanced Photon Source.

5.8 References

1. H. Okamoto, Journal of Phase Equilibria Diffusion, 2004, 25, 394
2. B. K. Vu, M. B. Song, I. Y. Ahn, Y. Suh, D. J. Suh, W. Kim, H. Koh, Y. G. Choi, E. W. Shin, Catalysis Today, 2011, 164, 214-220
3. L. Deng, T. Shishido, K. Teramura, T. Tanaka, Catalysis Today, 2014, 232, 33-39
4. R. Srinivasan, R. Sharma, S. Su, B. Davis, Catalysis Today, 1994, 21, 83-99
5. L. Deng, H. Miura, T. Shishido, S. Hosokawa, K. Teramura, T. Tanaka, ChemCatChem, 2014, 6, 2680-2691
6. E. C. Wegener, Z. Wu, H. Tseng, J. R. Gallagher, Y. Ren, R. E. Diaz, F. H. Ribeiro, J. T. Miller, Catalysis Today 2018, 299, 146-153
7. D. J. Childers, N. M. Schweitzer, S. Mehdi Kamali Shahari, R. M. Rioux, J. T. Miller, R. J. Meyer, Journal of Catalysis, 2014, 318, 75-84
8. J. R. Gallagher, D. J. Childers, H. Zhao, R. E. Winans, R. J. Meyer, J. T. Miller, Physical Chemistry Chemical Physics, 2015, 17, 28144-28153
9. C. J. Cybulskis, B. C. Bukowski, H. Tseng, J. R. Gallagher, Z. Wu, E. C. Wegener, A. J. Kropf, B. Ravel, F. H. Ribeiro, J. Greeley, J. T. Miller, ACS Catalysis, 2017, 7, 4173-4181
10. S. Kobayashi, S. Kaneko, M. Ohshima, H. Kurokawa, H. Miura, Applied Catalysis A: General, 2012, 417-418, 306-312
11. T. Ressler, J. Synchrotron Radiat. 1998, 5, 118-122
12. J. J. Rehr, R. C. Albers, S. I. Zabinsky, Phys. Rev. Lett. 1992, 69, 3397-3400
13. J. J. Rehr, R. C. Albers, Phys. Rev. B 1990, 41, 8139-8149
14. B. H. Toby, R. B. Von Dreele,. J Appl Crystallogr. 2013, 46, 544–549
15. L. Lutterotti, S. Matthies, H. Wenk, IUCr Newsletter of the CPD, 1999, 21, 14–15
16. T. B. Bolin, T. Wu, N. Schweitzer, R. Lobo-Lapidus, A. J. Kropf, H. Wang, Y. Hu, J. T. Miller, S. M. Heald, Catal. Today 2013, 205, 141-147
17. a: G. Kresse, J. Furthmüller, Computational materials science 1996, 6, 15-50; b: G. Kresse, J. Furthmüller, Physical review B 1996, 54, 11169; c: G. Kresse, J. Hafner, Physical Review B 1993, 47, 558; d: G. Kresse, J. Hafner, Physical Review B 1994, 49, 14251
18. J. P. Perdew, K. Burke, M. Ernzerhof, Physical review letters 1996, 77, 3865
19. a: P. E. Blöchl, Physical review B 1994, 50, 17953; b: G. Kresse, D. Joubert, Physical Review B 1999, 59, 1758

20. P. Glatzel, J. Singh, K. O. Kvashnina, J. van Bokhoven, J. Am. Chem. Soc., 2010, 132, 2555-2557
21. J. T. Miller, A. J. Kropf, Y. Zha, J. R. Regalbuto, L. Delannoy, C. Louis, E. Bus, J. A. van Bokhoven, Journal of Catalysis, 2006, 240, 222-234
22. M. G. Mason, Physical Review B, 1983, 27, 748-762
23. L. F. Mattheiss, R. E. Dietz, Physical Review B, 1980, 22, 1663-1676
24. P. K. Jain, Structural Chemistry, 2005, 16, 421-426
25. Y. Lei, J. Jelic, L. C. Nitsche, R. Meyer, J. Miller, Top. Catal., 2011, 54, 334-348
26. B. Hu, N. M. Schweitzer, G. Zhang, S.J. Kraft, D. J. Childers, M. P. Lanci, J. T. Miller, A S. Hock, ACS Catal., 2015, 5, 3494-3503
27. G. Bredig, R. Allolio, Zeitschrift fuer Physikalische Chemie (Leipzig), 1927, 126, 41-71
28. J. Crangle, J.A. Shaw, Philisophical Magazine, Seri 8 (1956-), 1962, 7, 207-212
29. J. Crangle, J.A. Shaw, Philisophical Magazine, Seri 8 (1956-), 1983, 38, 1-22
30. K.H.J. Buschow, P.G. van Engen, R. Jongebreur, Journal of Magnetism and Magnetic Materials, 1983, 38, 1-22
31. D.W. Moon, D.J. Dwyer, S.L. Bernasek, Surface Science, 1985, 163, 215-229
32. K. J. Yoon, P.L. Walker Jr, L. N. Mulay, M. A. Vannice, Ind. Eng. Chem. Prod. Res. Dev., 1983, 22, 519-526
33. M. Boudart, A. Delbouille, J. A. Dumesic, S. Khammouma, H. Topsoe, Journal of Catalysis, 1975, 37 486-502
34. H-J. Jung, M. A. Vannice, LN. Mulay, R.M. Stanfield, W.N. Delgass, Journal of Catalysis, 1982, 76, 208-224
35. J Benziger, R.J. Madix, Surface Science, 1980, 94, 119-153
36. J. E. Benson, M. Boudart, Journal of Catalysis, 1965, 4, 704-710
37. Rachmady, M. A. Vannice, Journal of Catalysis, 2002, 209, 87-98
38. C.H. Bartholomew, M. Boudart, Journal of Catalysis, 1973, 29, 278-291
39. N Guo, B.R. Fingland, W. D. Williams, V.F. Kispersky, J. Jelic, W.N. Delgass, F. H Ribeiro, R. J. Meyer, J.T. Miller, Phys. Chem. Chem. Phys., 2010, 12, 5678-5693
40. M. Teliska, W.E. O'Grady, D.E. Ramaker, J Phys Chem B, 2005, 109, 8076-8084
41. J. Llorca, N. Homs, J. L. G. Fierro, J. Sales, P. Ramirez de la Piscina, Journal of Catalysis, 1997, 166, 44-52

42. Y Xu, A. V.Ruban, M. Mavrikakis, J. Am Chem. Soc., 2004, 126, 4717-4725
43. J. Greeley, M. Mavrikakis, Nature Materials, 2004, 3, 810-815
44. C.A. Menning, J. G. Chen, J. Chem. Phys., 2009, 130, 174709
45. A.V. Ruban, H.L. Skriver, JK. Norskov, Physical Review B, 1999, 59, 15990-16000
46. M.C.Y. Chen, L. Chen, F. Nan, J. F. Britten, C. Bock, G.A. Botton, Nanoscale, 2012, 4, 7273-7279
47. S. Prabhudev, M. Bugnet, G. Zhu, C. Bock, G.A. Botton, ChemCatChem, 2015, 7, 3655-3664
48. V. R. Stamenkovic, B. S. Mun, M. Arenz, K. J.J. Mayrhofer, C. A. Lucas, G. Wang, P. R. Ross, N. M. Markovic, Nature Materials, 2007, 6, 241-247
49. Z. Liu, G. S. Jackson, B. W. Eichorn, Energy Enviro. Sci., 2011, 4, 1900-1903
50. J. R. Gallagher, T. Li, H. Zhao, J. Liu, Y. Lei, X. Zhang, Y. Ren, J. W. Elam, R. J. Meyer, R. E. Winans, J. T. Miller, Catalysis Science and Technology, 2014, 4, 3053-3063
51. Z. Wu, E. C. Wegener, H. Tseng, J. R. Gallagher, J. W. Harris, R. E. Diaz, Y. Ren, F. H. Ribeiro, J. T. Miller, Catalysis Science and Technology, 2016, 6, 6965-6976
52. J. Singh, R.C. Nelson, B. C. Vicente, S. L. Scott, J.S. van Bokhoven, Phys. Chem. Chem. Phys., 2010, 12, 5668-5677
53. M. Watanabe, H. Uchida, K. Ohkubo, H. Igarahi, Applied Catalysis B. Environmental, 2003, 46, 595-600
54. A. Siani, O.S. Alexeev, B. Captian, G. Lafaye, P. Marecot, R. D. Adams, M. D. Amiridis, Journal of Catalysis, 2008, 255, 162-179
55. A. Siani, O.S. Alexeev, G. Lafaye, M.D. Amirids, Journal of Catalysis, 2009, 266, 26-38
56. G. Blyholder, The Journal of Physical Chemistry, 1964, 68, 2772-2777
57. J. Silvestre-Albero, M. A. Sanchez-Castillo, R. He, A. Sepulveda-Escribano, F Rodriguez-Reinoso, J.A. Dumesic, Catalysis Letters, 2001, 74, 17-25

CHAPTER 6. SUMMARY

The works discussed in this dissertation support the proposal that geometric rather than electronic changes to catalytic metals upon alloying are the dominant factor leading to higher selectivity for light alkane dehydrogenation. The synthesis of intermetallic compounds results in active sites with well-defined and uniform geometries. By forming structures with small ensembles of, or completely isolated, active atoms selective alkane dehydrogenation catalysts can be made. Although post-transition metals are most commonly used as promoters for dehydrogenation reactions the proposal of geometric control of selectivity can be applied to other elements, as evidenced by the results on Pt-Fe catalysts in Chapter 5. From the results discussed in Chapter 2 about the Pd-In IMCs it seems that structures which require minimal atomic rearrangement from the crystal structure of the catalytic metal are preferentially formed. With this knowledge it is possible to choose potential catalytic metal-promoter element combinations for light alkane dehydrogenation catalysts from the information contained in bulk phase diagrams.

The above principles can be used when choosing possible promoters, however, other factors also influence whether the selected bimetallic system has the potential for use in an industrial process. One such consideration is the over-reduction of the promoter metal as observed in Chapters 2 and 5. In the Pd-In system over-reduction of In caused the partial coverage of the active surface by an inactive species which resulted in less efficient catalysts on a mass basis. As seen in the Pt-Fe catalysts, over-reduction of the promoter led to the formation of a second phase. Although no adverse effects were seen in this case, if two catalytic metals of comparable activity were used the presence of the second phase could result in lower selectivity. These results suggest that an ideal promoter would be a non-catalytic element which is difficult to fully reduce.

Forming intermetallic compounds was found to change the average energy of the valance states of Pt. Although this was found to have minimal effect on dehydrogenation selectivity, small changes in turnover rates were observed. In Chapters 2, 3, and 4 the intermetallic compound catalysts were found to have higher apparent activation energies than their monometallic analogues. In Chapter 5, Pt-Fe IMCs were found to have weaker metal-adsorbate bonds than Pt which likely results in differences in surface coverages during reaction. Both changes in reaction barriers and coverages can cause changes in rates. While the electronic structure measurements and calculations reported here were only performed on Pt, recent L edge XANES results from our

group on Pd-containing IMC catalysts are consistent with the changes observed for the materials discussed in the work. These new results suggests that IMC formation has the potential to be used as a route to selectivity tune the electronic structure of different catalytic metals and is not unique to Pt. Studying IMC materials as catalysts in systems where the rates of competing reactions are dependent upon the electronic structure presents an exciting new research direction and provides an opportunity to further couple experiments and theory. From well-designed collaborative studies a more detailed understanding of the effects of alloying and electronic structure changes on the catalytic properties of metals can be gained and could significantly assist in the rational design of improved materials.

APPENDIX A. CHAPTER 2 SUPPORTING INFORMATION

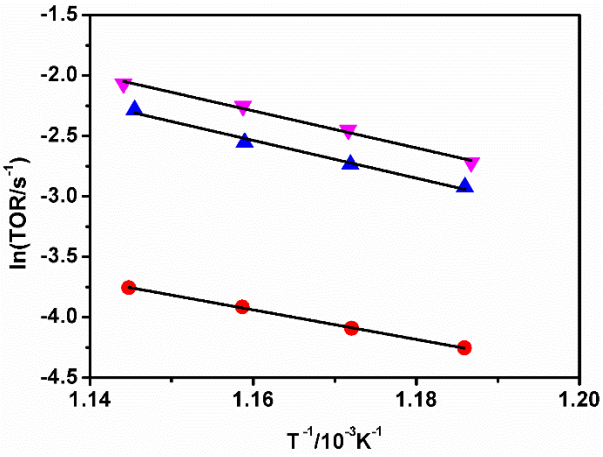

Figure A.1: Arrhenius plot for ethane dehydrogenation over Pd-In 0.2 (red), Pd-In 0.8 (blue) and Pd-In 2.0 (magenta) catalysts. Activation energy measurements were conducted between 570 and 600 ^{o}C under 5 % C_2H_6, 2 % H_2, 0.5 % C_2H_4, 43.2 % He, and balance N_2 at 1 atm with a total flow rate of 150 cm^3/min. The conversion in all tests are below 10 % and far from equilibrium as confirmed by approach to equilibrium index β. The TORs have been corrected with the approach to equilibrium index β.

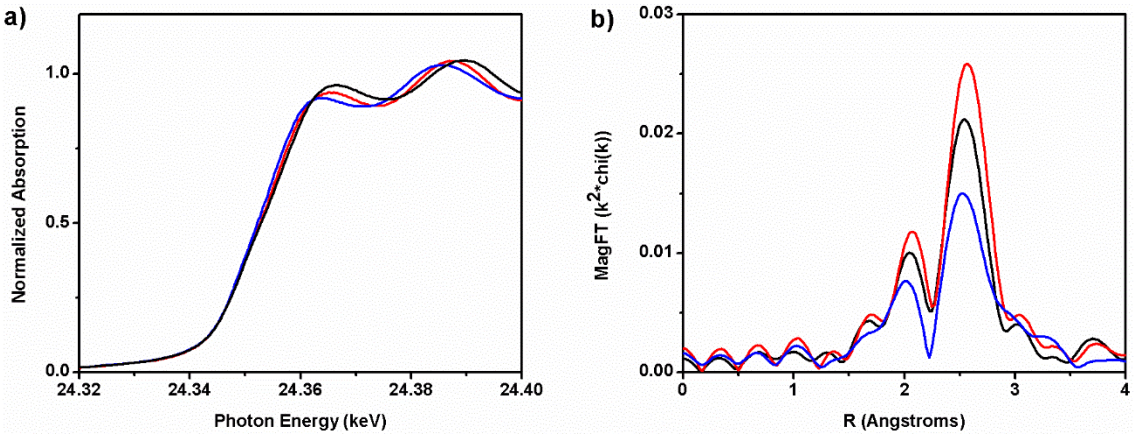

Figure A.2: a) XANES and b) magnitude of the Fourier Transform of the EXAFS at Pd edge of Pd (black), Pd-In 0.2 (red) and Pd-In 0.8 (blue) catalysts. The catalysts were reduced at 600 °C in a 4 % H_2/He mixture at 50 cm^3/min. After reduction, the samples were purged with He at 100 cm^3/min and cooled to room temperature before the XAS spectra were obtained.

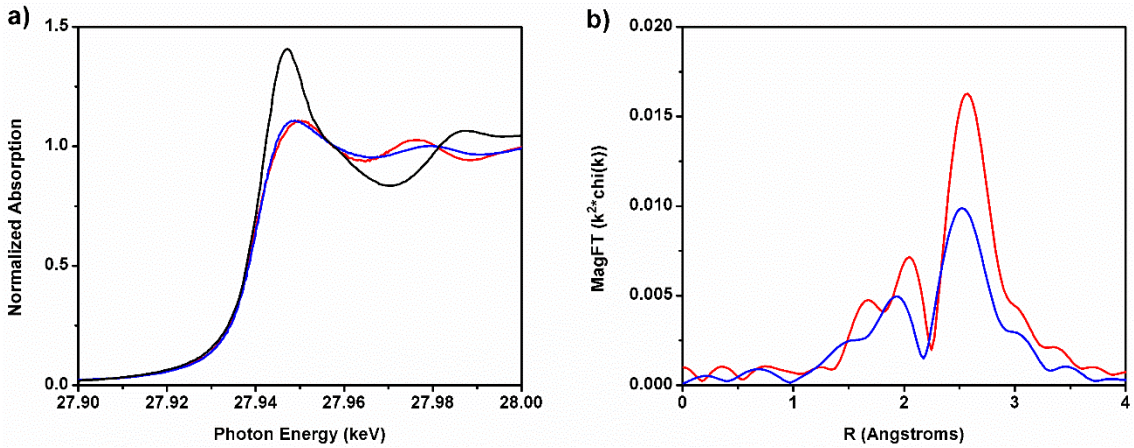

Figure A.3: a) XANES at the In edge of Pd-In 0.2 (red) and Pd-In 0.8 (blue) catalysts compared with Indium oxide (black) and b) magnitude of the Fourier Transform of the EXAFS at the In edge of Pd-In 0.2 (red) and Pd-In 0.8 (blue) catalysts. The catalysts were reduced at 600 °C in a 4 % H_2/He mixture at 50 cm^3/min. After reduction, the samples were purged with He at 100 cm^3/min and cooled to room temperature before the XAS spectra were obtained.

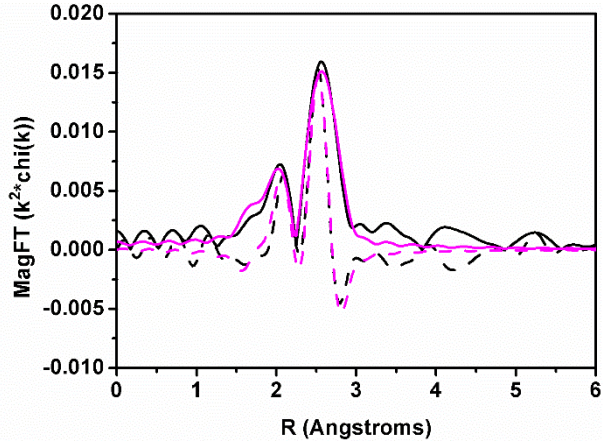

Figure A.4: Fitting results of the R-space EXAFS spectrum at Pd edge of pre-reduced Pd-In 2.0 as an example for Pd-In catalysts. The solid black line represents the FT magnitude, the dashed black line the imaginary part of the FT while the magenta solid and dashed lines are the fits of the magnitude and the imaginary part respectively. (3.0 $Å^{-1}$ < k < 12.0 $Å^{-1}$, 1.6 Å < R < 2.9 Å).

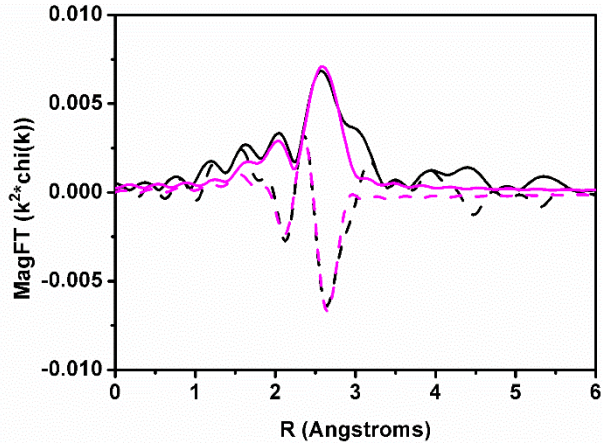

Figure A.5: Fitting results of the R-space EXAFS spectrum at In edge of pre-reduced Pd-In 2.0 as an example for Pd-In catalysts. The solid black line represents the FT magnitude, the dashed black line the imaginary part of the FT while the magenta solid and dashed lines are the fits of the magnitude and the imaginary part respectively. (3.0 $Å^{-1}$ < k < 12.0 $Å^{-1}$, 1.8 Å < R < 2.8 Å).

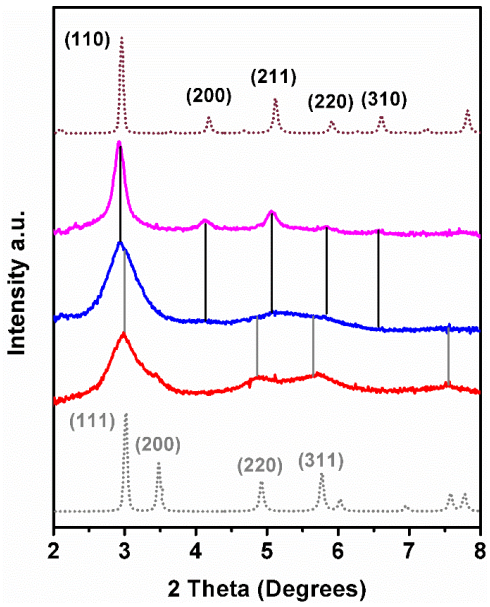

Figure A.6: Background subtracted *in situ* XRD pattern of Pd-In-0.2 (red), Pd-In-0.8 (blue), and Pd-In-2.0 catalyst (magenta, 1/2 the original peak intensity) compared with the simulated XRD pattern (with major peaks indexed) of bulk FCC Pd (grey, dotted), and bulk PdIn intermetallic compound phase (black, dotted) at 600 °C after the catalysts were reduced under 50 cm^3/min 3 % H_2/Ar flow at 600 °C for 20 min. The grey vertical line marks the diffraction features in the samples from FCC Pd phase, while the black vertical line marks those from PdIn IMC phase. Except for peak displacement caused by thermal induced lattice expansion, the patterns show the same features as those taken at RT, indicating unchanged crystal structure of the catalysts in the two different temperature.

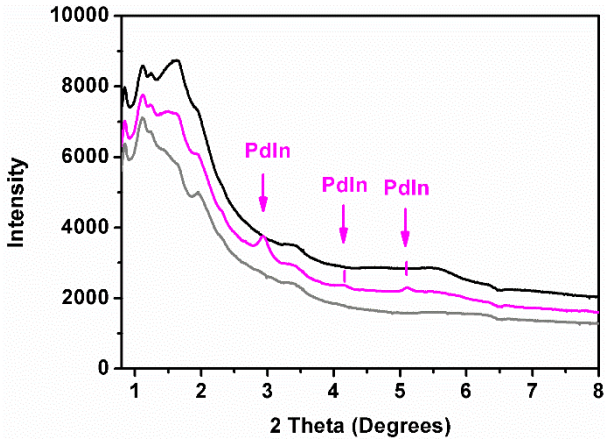

Figure A.7: XRD pattern raw data of Pd-In 2.0/SiO_2 catalysts (magenta) compared with empty cell (grey) and the cell loaded with only SiO_2 (black). The data was recorded *in situ* at RT in 3 % H_2/Ar flow after the samples were reduced under 50 cm^3/min 3 % H_2/Ar flow at 600 °C for 20 min. The data of Pd-In 2.0/SiO_2 and SiO_2 are slightly shifted up in vertical axis for better visualization.

APPENDIX B. CHAPTER 4 SUPPORTING INFORMATION

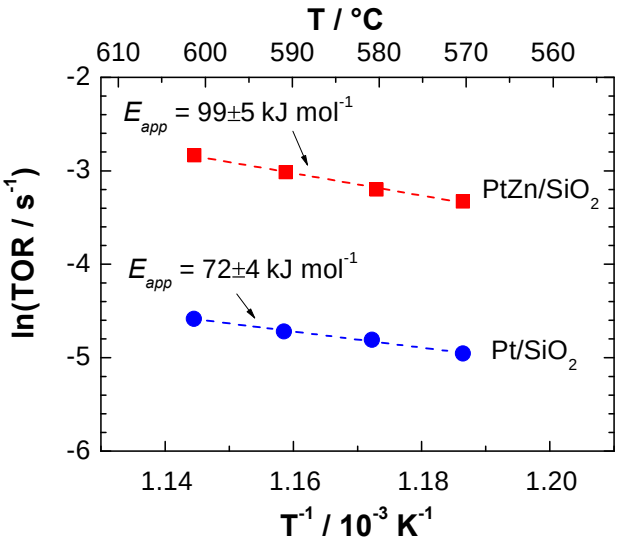

Figure B.1: Arrhenius plots for Pt/SiO_2 and $PtZn/SiO_2$. TOR for EDH were measured between 570 °C and 600 °C with 2.5% C_2H_6, 1% H_2, 0.5% C_2H_4 at 150 ml min^{-1} total flow and normalized per surface Pt by H_2 chemisorption.

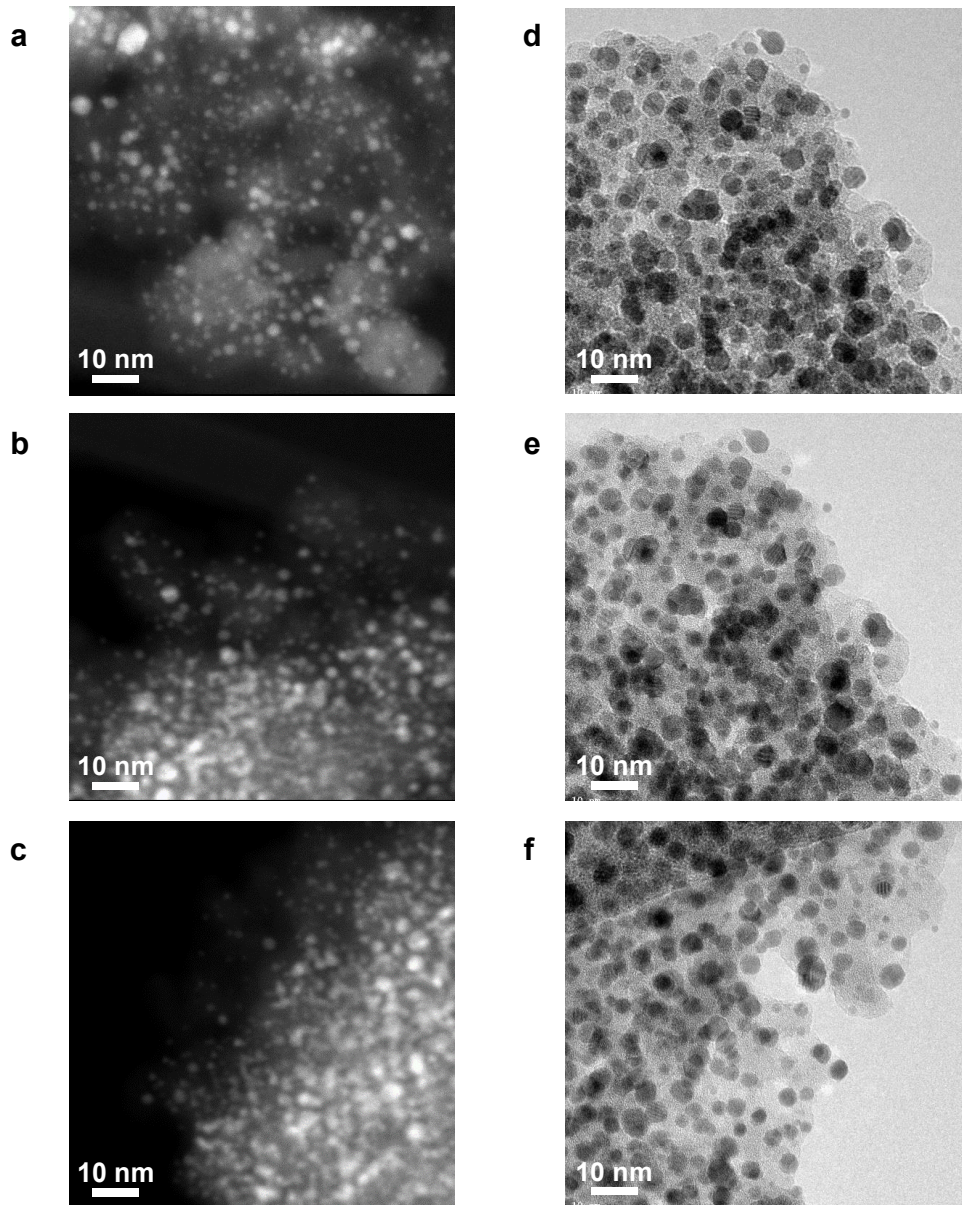

Figure B.2: Pt nanoparticles on amorphous SiO_2. (a – c) HAADF-STEM images of 9.70 wt.% Pt/SiO_2 after EDH at 600 °C. (d – f) TEM images of 9.70 wt.% Pt/SiO_2 after EDH at 600 °C.

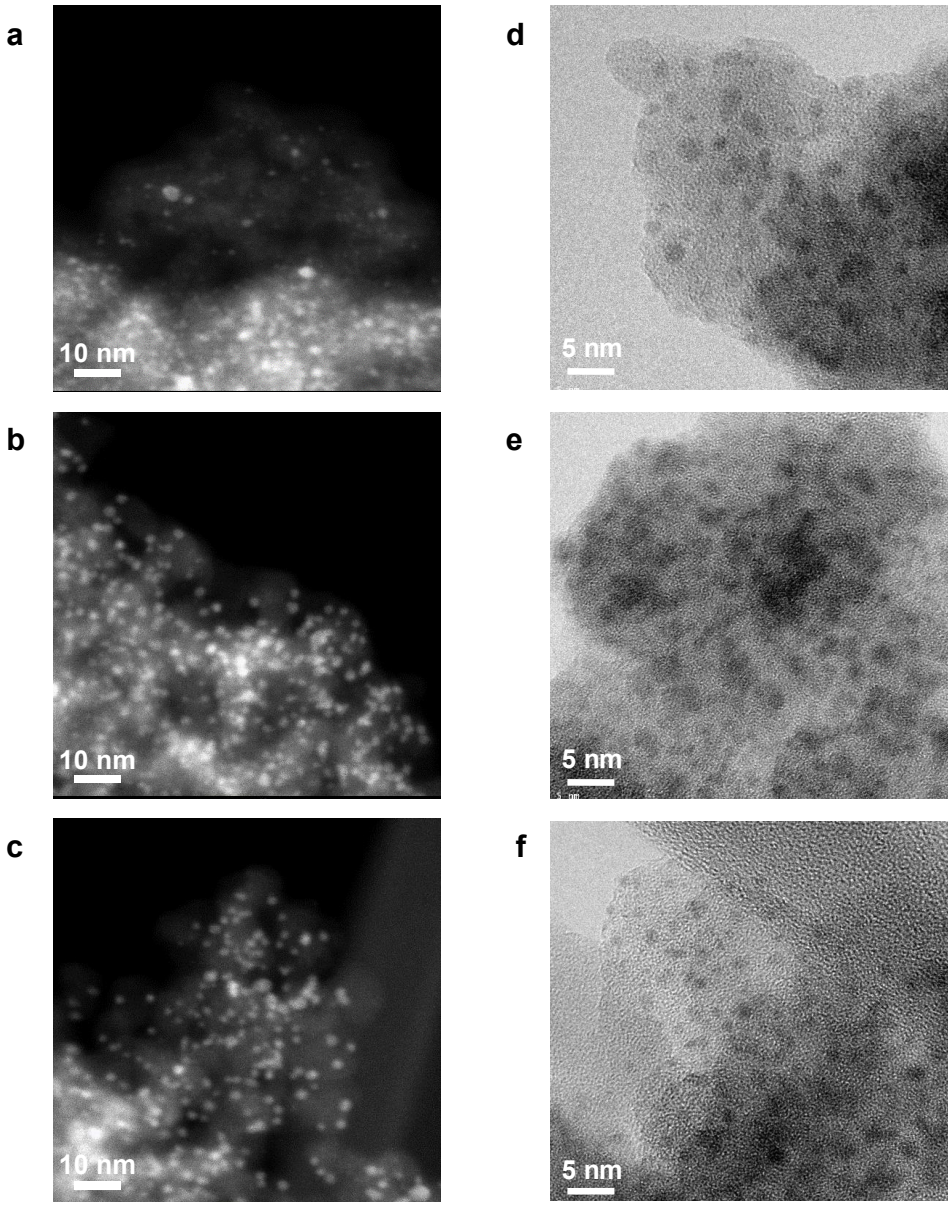

Figure B.3: PtZn nanoparticles on amorphous SiO_2. (a – c) HAADF-STEM images of 9.53 wt.% Pt – 9.28 wt.% Zn/SiO_2 after EDH at 600 °C. (d – f) TEM images of 9.53 wt.% Pt – 9.28 wt.% Zn/SiO_2 after EDH at 600 °C.

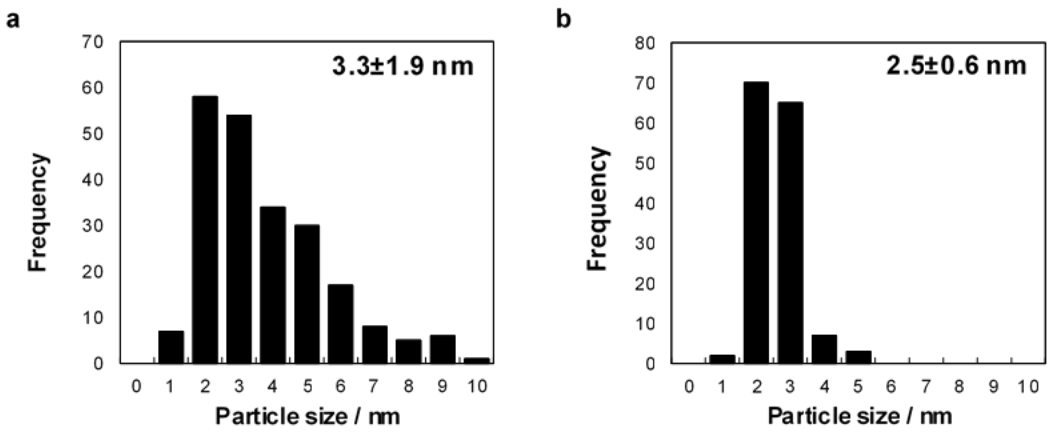

Figure B.4: Metal cluster size distributions. (a) Determined for 9.70 wt.% Pt/SiO_2 by HAADF-STEM and TEM. (b) Determined for 9.53 wt.% Pt – 9.28 wt.% Zn/SiO_2 by HAADF-STEM and TEM. Cluster size distributions were determined by counting between 150 – 225 particles per sample.

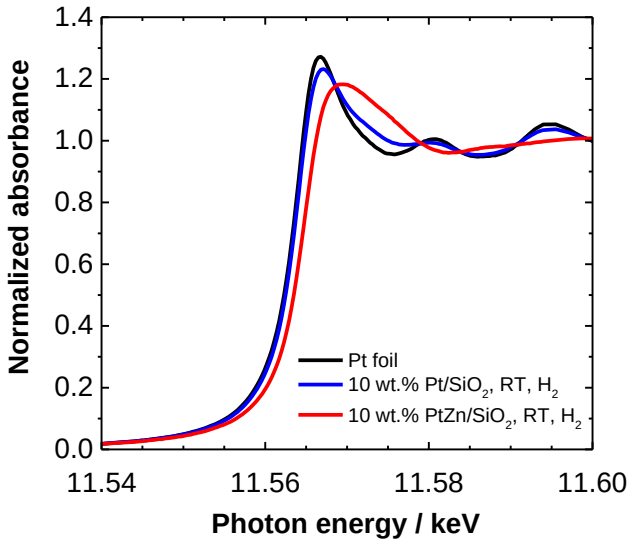

Figure B.5: Pt L_3 XANES spectra. Shown from 11.54 to 11.60 keV for Pt foil, 9.70 wt.% Pt/SiO_2, and 9.53 wt.% Pt – 9.28 wt.% Zn/SiO_2 and obtained in H_2 at room temperature after H_2 reduction at 600 °C.

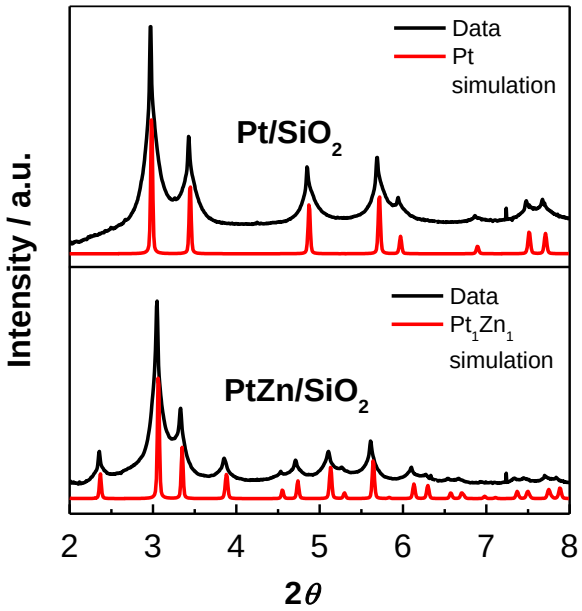

Figure B.6: *In situ* XRD patterns at 600 °C in hydrogen. Obtained for 9.70 wt.% Pt/SiO_2 and 9.53 wt.% Pt – 9.28 wt.% Zn/SiO_2 in 3% H_2, balance Ar (50 ml min^{-1} total flow) and compared to simulated patterns for Pt and Pt_1Zn_1, respectively.

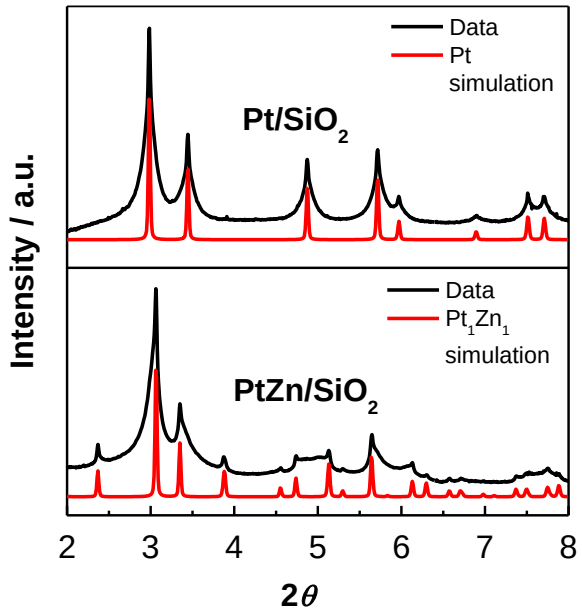

Figure B.7: *In situ* XRD patterns at room temperature in air. Obtained for 9.70 wt.% Pt/SiO_2 and 9.53 wt.% Pt – 9.28 wt.% Zn/SiO_2 and compared to simulated patterns for Pt and Pt_1Zn_1, respectively.

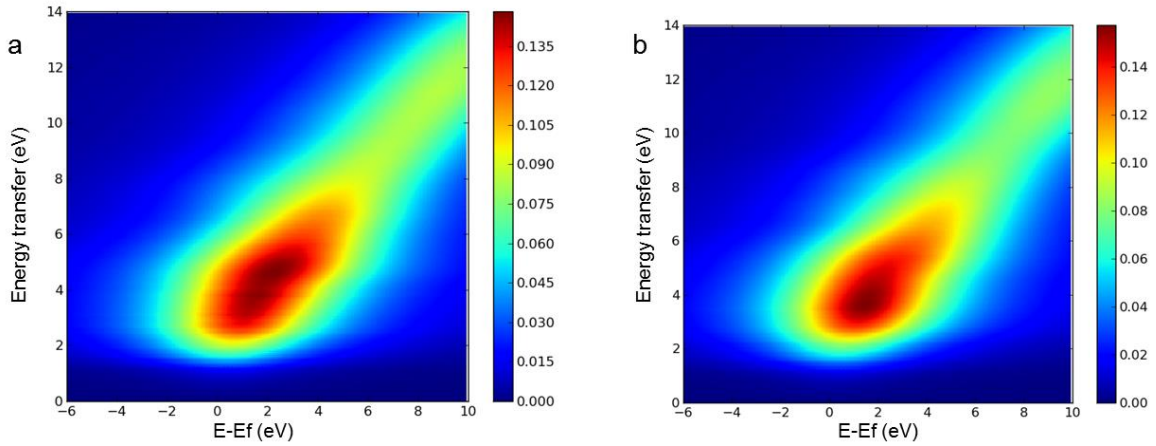

Figure B.8: RIXS energy maps for the: (a) $Pt_1Zn_1(110)$ surface termination, and (b) $Pt_1Zn_1(101)$ surface termination.

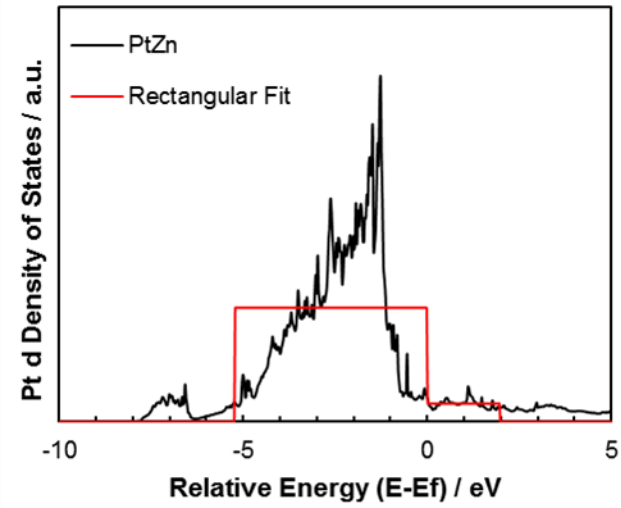

Figure B.9: PtZn *d*-DOS and rectangular fitting for the simplified RIXS analysis. The center of each rectangle is the band center of the occupied and unoccupied states. The width of each rectangle is twice the band center. The height of the rectangle is fixed by the constraint that the total number of electrons in the band is constant.

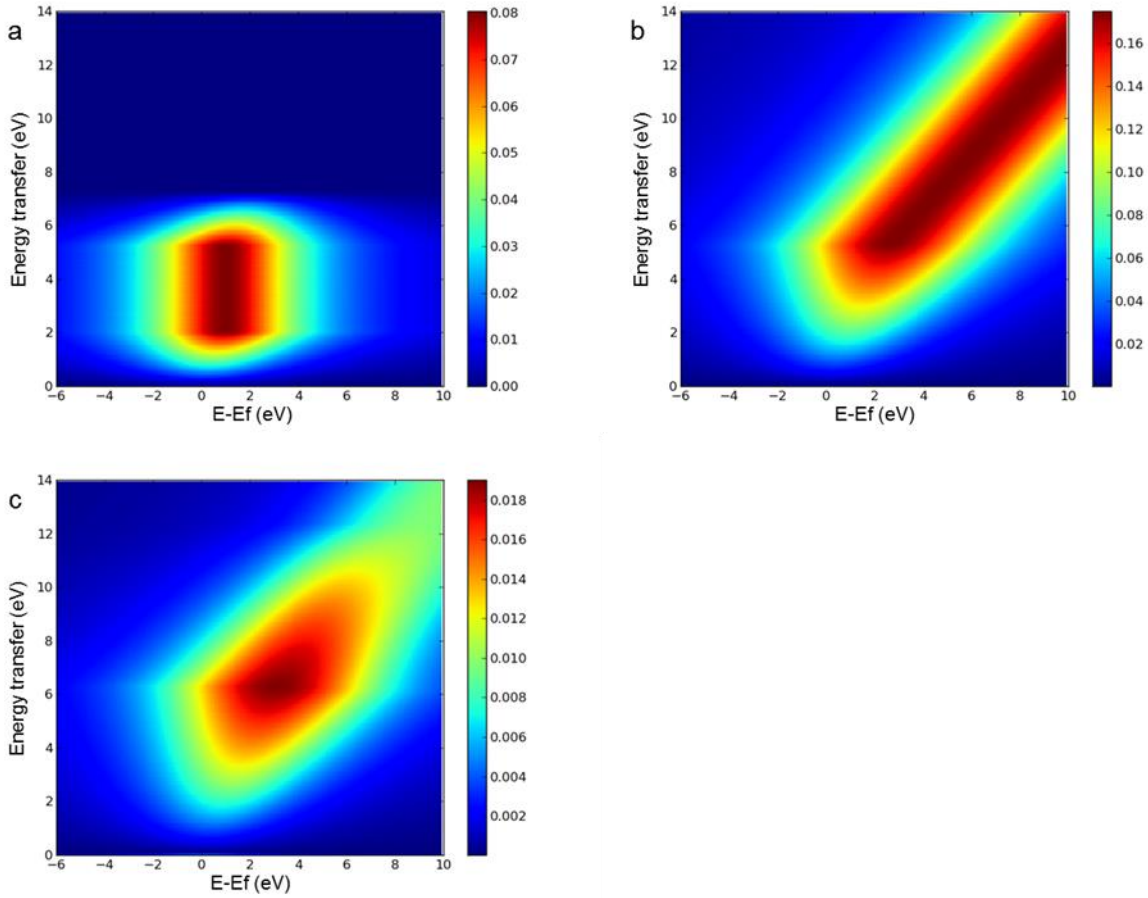

Figure B.10: Simulated PtZn RIXS spectra for simplified rectangular DOS analysis. The small-width of unoccupied states in (a) shows a localized peak with no tail. The long, uniform width of unoccupied states in (b) shows a hypothetical long tail distribution with constant high intensity along the tail. In (c)**,** an additional rectangle of lesser height is appended to the unoccupied DOS, leading to the formation of a tail of decaying intensity.

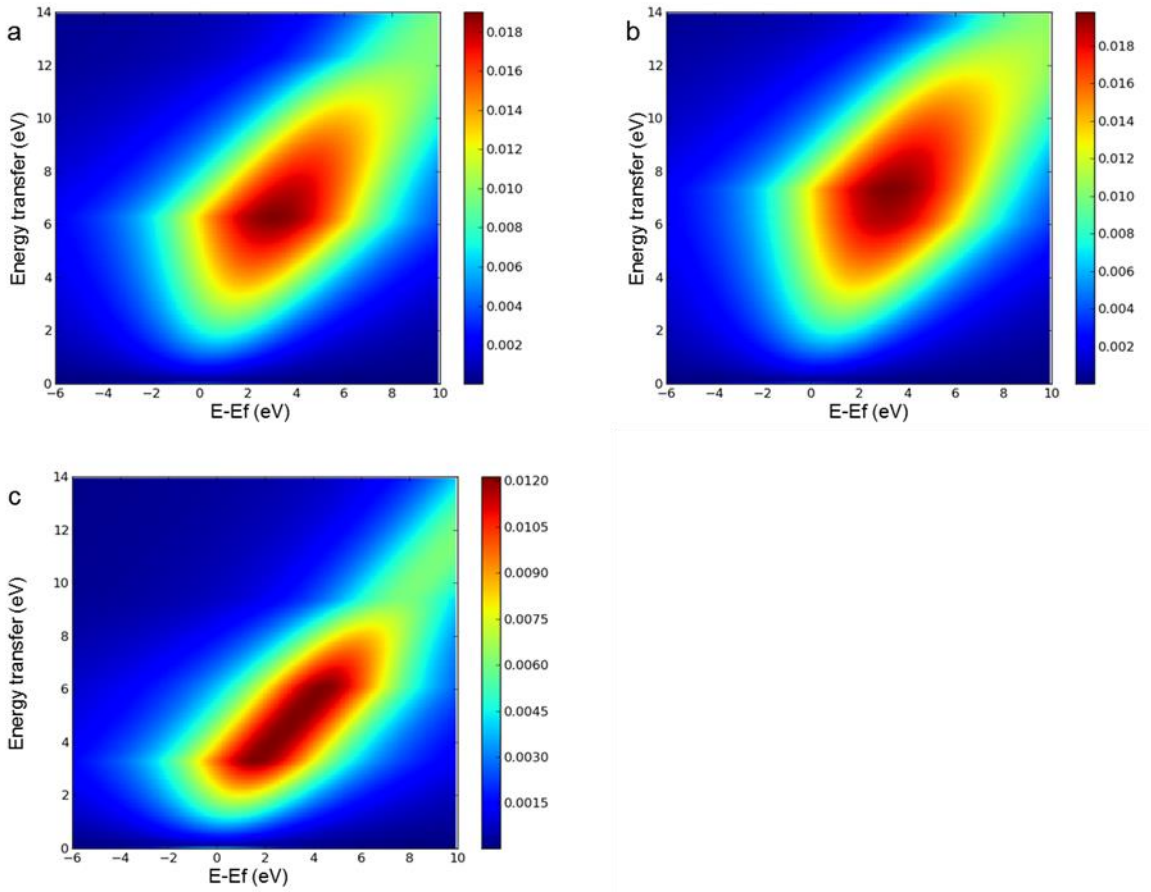

Figure B.11: Adjusted PtZn RIXS spectra for the simplified rectangular DOS analysis. In (a), the unoccupied DOS is split into a second rectangular identical to Fig. B. 10(c). In (b), the width of the band is adjusted to be 2 eV longer than (a) by adding additional states at the edge below the Fermi energy (E_f). In (c), the width of the band is decreased such that the DOS is 2 eV narrower than (a) by removing states at the edge below E_f.

Table B.1: Hydrogen uptake on Pt/SiO_2 and $PtZn/SiO_2$ catalysts

Catalyst	H_2 uptake / (μmol H_2) (g_{cat}^{-1})
9.70 wt.% Pt/SiO_2	67.1
9.53 wt.% Pt – 9.28 wt.% Zn/SiO_2	107.8

Measured at 35 °C after reduction in H_2 at 600 °C on fresh 9.70 wt.% Pt/SiO_2 and 9.53 wt.% Pt – 9.28 wt.% Zn/SiO_2.

Table B.2: Pt L_3 EXAFS fittings for first scattering shell

Sample	$N_{Pt\text{-}Pt}$	$R_{Pt\text{-}Pt}$ / Å	$N_{Pt\text{-}Zn}$	$R_{Pt\text{-}Zn}$ / Å	$\Delta\sigma^2$	d_P /nm [a]
Pt foil	12	2.77±0.01	N/A	N/A	0.0001	N/A
Pt/SiO_2	8.9±0.9	2.76±0.01	N/A	N/A	0.001	4.2±1.1
$PtZn/SiO_2$	3.6±0.3	2.81±0.02	7.1±0.6	2.63±0.01	0.005	N/A

Obtained on 9.70 wt.% Pt/SiO_2 and 9.53 wt.% Pt – 9.28 wt.% Zn/SiO_2 samples measured in H_2 at room temperature after H_2 reduction at 600 °C. [a] Pt metal cluster size for 9.70 wt.% Pt/SiO_2 estimated by using correlation developed by Miller et al. [33]

Table B.3: Pt and Pt_1Zn_1 unit cell parameters

Condition	9.70 wt.% Pt/SiO_2		9.53 wt.% Pt – 9.28 wt.% Zn/SiO_2		
	Pt		Pt_1Zn_1		
	$a = b = c$ / Å	$R_{Pt\text{-}Pt}$ / Å	$a = b$ / Å	c / Å	$R_{Pt\text{-}Zn}$ / Å
RT in 3% H_2, balance Ar	3.93±0.01	2.78±0.01	2.84±0.01	3.51±0.01	2.66±0.01

Determined from the diffraction peaks below 6° within the *in situ* XRD patterns for 9.70 wt.% Pt/SiO_2 and 9.53 wt.% Pt – 9.28 wt.% Zn/SiO_2 samples.

Kinetic Measurements

In the limit of low conversion ($X < 0.1$), the temperature and concentrations of reactants are assumed to be constant throughout the length of the catalyst bed, thereby allowing the plug flow reactor (PFR) to be treated as a differential reactor and modeled as a continuous stirred-tank reactor (CSTR). To satisfy these criteria and eliminate complications due to product inhibition, C_2H_4 was added to the reactor feed in an amount that only results in a differential change (< 10%) across the catalyst bed due to the chemical reaction. Thus, the reaction rate is approximately constant throughout the reactor and can be modeled as:

$$r = \frac{q([C_2H_6]_0 - [C_2H_6])}{W}$$

where r is the observed rate of reaction ((mole C_2H_6) $(g_{cat})^{-1}$ s^{-1}); q is the volumetric flow rate (ml min^{-1}); $[C_2H_6]_0$ is the initial concentration of ethane ((mole C_2H_6) ml^{-1}); $[C_2H_6]$ is the concentration of ethane ((mole C_2H_6) ml^{-1}); and W is the catalyst mass (g).

Since EDH is an equilibrium-limited reaction, the forward reaction rate is related to the observed reaction rate, r, by [60]:

$$r_f = \frac{r}{(1-\eta)}$$

$$k_f = A\exp\left(\frac{-E_{app}}{RT}\right)$$

$$\eta = \frac{[C_2H_4][H_2]}{K_{eq}[C_2H_6]}$$

where r_f is the forward rate ((mole C_2H_6) $(g_{cat})^{-1}$ s^{-1}); k_f is the forward rate constant; η is the approach to equilibrium; A is the pre-exponential factor; E_{app} is the apparent activation energy (kJ $mole^{-1}$); R is the universal gas constant (kJ $mole^{-1}$ K^{-1}); and T is the reaction temperature (K).

The conversion is ethane, *X*, is determined by dividing the rate of ethane consumption by the inlet flow rate of ethane:

$$X = \frac{r}{q[C_2H_6]_0}$$

The ethylene selectivity, $S_{C_2H_4}$, is given by:

$$S_{C_2H_4} = \frac{\nu_{C_2H_4} r_{C_2H_4}}{\sum_{i=1}^{N} (\nu_i r_i)}$$

where $\nu_{C_2H_4}$ is the stoichiometric coefficient of ethylene; $r_{C_2H_4}$ is the rate of ethylene formation ((mole C_2H_4) $(g_{cat})^{-1}$ s^{-1}); and v_i and r_i are the stoichiometric coefficient and rate of formation of species *i*, respectively.

DFT Calculations

PtZn surface terminations

For the tetragonal PtZn unit cell, the (110) and (101) terminations are more closely packed than the (111) termination. The (110) and (101) terminations have different surface lattice distances, and both were considered in Figure 4.13. The RIXS planes were similar for both surface terminations although the high intensity peak was slightly broader for the (110) surface.

Theoretical RIXS distributions

To provide additional insight into the relationship between the *d*-band DOS and the shape of the RIXS planes, a simplified DOS model was developed. The occupied and unoccupied electronic states were approximated as rectangular distributions subject to the following constraints applied independently to the occupied and unoccupied states: (i) the DOS must be non-zero at the Fermi energy (E_f) to maintain metallic character of the band, (ii) the band centers of the occupied and unoccupied states of the rectangular DOS must reflect the corresponding *d*-band centers of the true DOS, and (iii) the integral of the complete rectangular and true *d*-band DOSs must be equivalent

to accurately reflect the total number of electrons in the band. As each rectangle was individually fitted by this procedure, the band filling of Pt was also preserved. A schematic representation is shown in Fig. B.9 for the PtZn alloy.

By varying the width of the unoccupied DOS and maintaining a constant height, the RIXS tail became more prominent, but at a constant intensity. The unoccupied DOS were decomposed further into two rectangles, where the second rectangle had a lower height. This lower height approximated a DOS distribution where the density of unoccupied states decreased at higher energies relative to E_f. The high intensity peak remained throughout this distribution; however, it decreased similarly to the experimental spectra at increasing energies. We note that the *d*-DOS in a DFT calculation can only be carried out to a finite number of states, and high energies are less accurate to the true band structure where additional scattering processes become more likely. Thus, the longer and higher intensity tails in the experimental spectra were likely due to a combination of higher energy *d* states and potentially scattering across other unoccupied orbitals above the *d* states. The structure of the high intensity peak also changed, although it appeared to be less sensitive to the continuum of unoccupied states.

To probe the influence of the width of the occupied states on simulated RIXS spectra, the width of the occupied states for the rectangular DOS developed in Fig. B.10(c) was increased by manually adjusting the lower bound of the rectangle at constant height. While this adjustment changed the number of electrons in the band, it allowed for a simplified analysis which showed that the location of the energy transfer peak (*y*-axis in Fig. B.10) was modulated by the occupied state energies. Decreasing the width of the rectangle shifted the energy transfer to a lower value, while increasing the width shifted the energy transfer to a higher value. Thus, the energy separation at which bond formation is favorable is modulated by the occupied states, while the tails of the distribution appear to be more strongly correlated to the density of unoccupied states (Fig. B.11).

APPENDIX C. CHAPTER 5 SUPPORTING INFORMATION

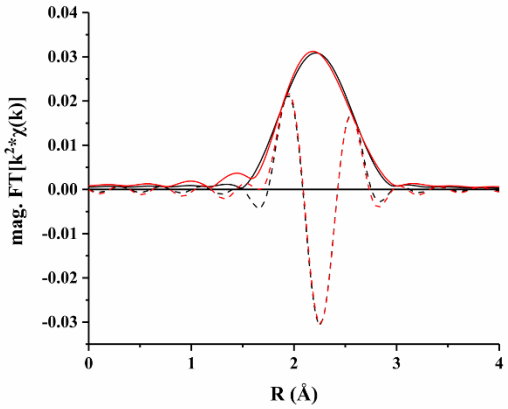

Figure C.1: The magnitude (solid) and imaginary part (dashed) of the Fourier transformed k^2-weighted EXAFS of the monometallic Fe catalyst. (Black – experimental data and Red – fit)

The Fe K edge EXAFS spectrum of the Fe catalyst was fit using two Fe-Fe scattering paths. Due to the bcc structure of Fe the scattering from the nearest and second-nearest neighbors results in overlapping peaks, making single-scatter fits unreliable. A-Fe having a bcc structure (8 Fe-Fe bonds at 2.48 Å and 6 Fe-Fe bonds at 2.87 Å) was used as a model for FEFF calculations. S_o^2 and σ^2 values (Table C.1) were determined from an Fe foil. From XRD it was seen that the metallic phase was large α-Fe. Therefore, the ratios of the coordination numbers and bond distances of the two paths were held constant during fits while the absolute values were varied. The σ^2 values of the two paths were fixed at the bulk values. Once the fractional coordination numbers were obtained the amount of metallic Fe was estimated by dividing the fitted value and the actual value from the bulk.

Table C.1: EXAFS fitting parameters of Fe foil and the monometallic Fe catalyst

Sample	S_o^2	Scattering Path	CN	R (Å)	σ^2 (x10^3)	E_o (eV)
Fe Foil	0.62	$(Fe\text{-}Fe)_{short}$	8	2.45	4.0	3.4
		$(Fe\text{-}Fe)_{long}$	4	2.84	2.5	3.8
Fe		$(Fe\text{-}Fe)_{short}$	4.7	2.44	4.0	2.0
		$(Fe\text{-}Fe)_{long}$	3.5	2.84	2.5	1.2

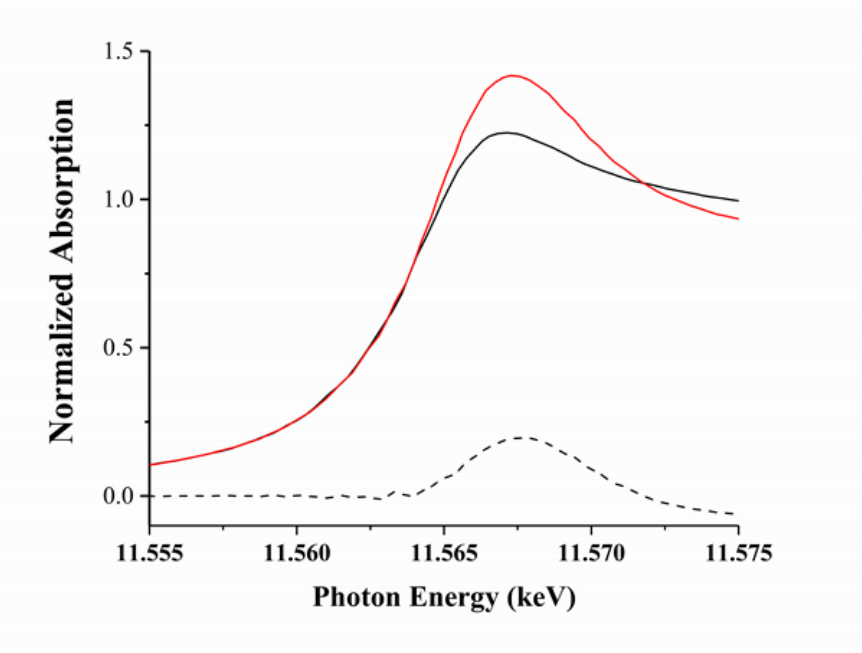

Figure C.2: Pt L_{III} XANES of Pt nanoparticles after reduction (black) and surface oxidation (red) and ΔXANES (dashed black).

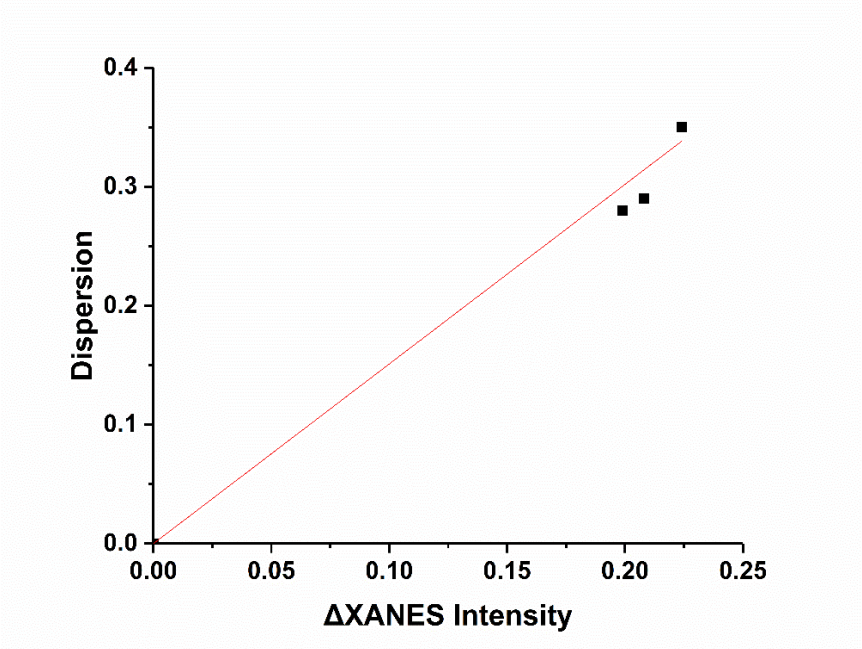

Figure C.3: Dispersion versus ΔXANES intensity of Pt nanoparticles of different sizes

Table C.2: Monometallic Pt catalysts used for calibration of Dispersion versus ΔXANES Intensity Correlation

Catalyst[1]	Synthesis Method[2]	Calcination Temperature	H_2 Reduction Temperature	Dispersion	
				CO Chemisorption	EXAFS
Pt #1	IMP	225 °C	550 °C	36 %	34 %
Pt #2	SEA	300 °C	600 °C	29 %	31 %
Pt #3	IMP	400 °C	550 °C	---	28 %

[1] All catalyst are nominal 2 wt % Pt on SiO_2 support and $Pt(NH_3)_4(NO_3)_2$ was used as the metal precursor for each catalyst.
[2] IMP – Incipient Wetness Impregnation, SEA – Strong Electrostatic Adsorption

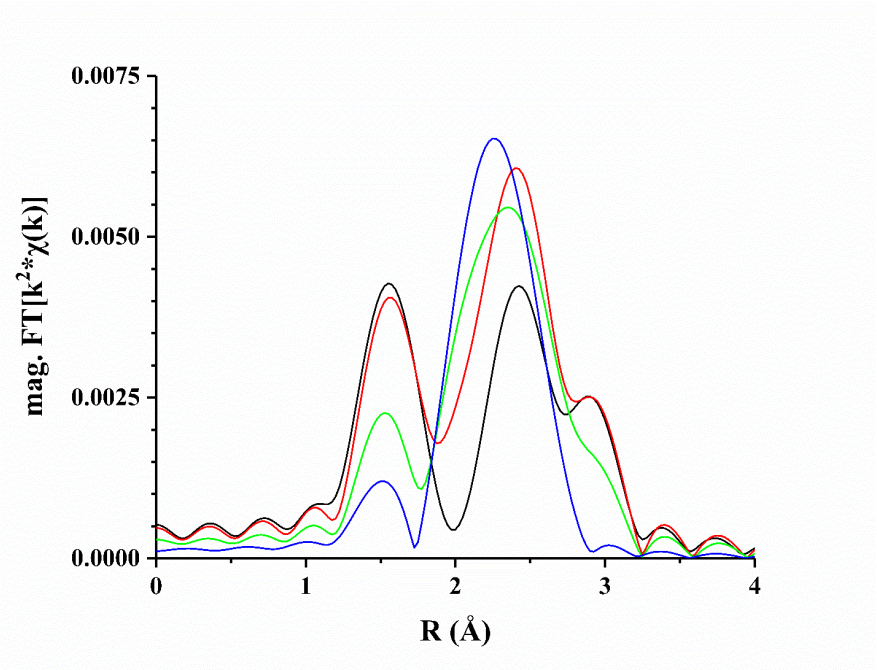

Figure C.4: Magnitude of the Fourier transform of the k^2-weighted ΔEXAFS spectra of Pt (black), Pt-Fe(0.7) (red), Pt-Fe(2.9) (green), and Pt-Fe(4.4). The peak at ~1.5 Å (phase uncorrected distance) is due to Pt - oxygen scattering. The peaks from ~2 – 3 Å (phase uncorrected distances) are due to Pt – metal scattering.

Table C.3: Fitting parameters of L_{III} Edge ΔEXAFS spectra of Pt and Pt-Fe catalysts

Catalyst	Scattering Path	CN	R (Å)	$\Delta\sigma^2$ (x10^3)	E_o (eV)
Pt	Pt-O	1.1	2.05	2	-0.9
	Pt-Pt	2.6	2.74	2	0.7
Pt-Fe(0.7)	Pt-O	1.0	2.07	2	-0.7
	Pt-Pt	2.5	2.76	2	0.4
	Pt-Fe	1.1	2.69	5	0.2
Pt-Fe(2.9)	Pt-O	0.5	2.05	2	-4.4
	Pt-Pt	1.9	2.78	2	-1.7
	Pt-Fe	1.8	2.66	5	1.7
Pt-Fe(4.4)*	Pt-Fe	2.7	2.68	5	1.1

* Due to the low intensity of the peak in Pt-Fe(4.4) a reliable fit of the Pt-O scattering path could not be obtained.

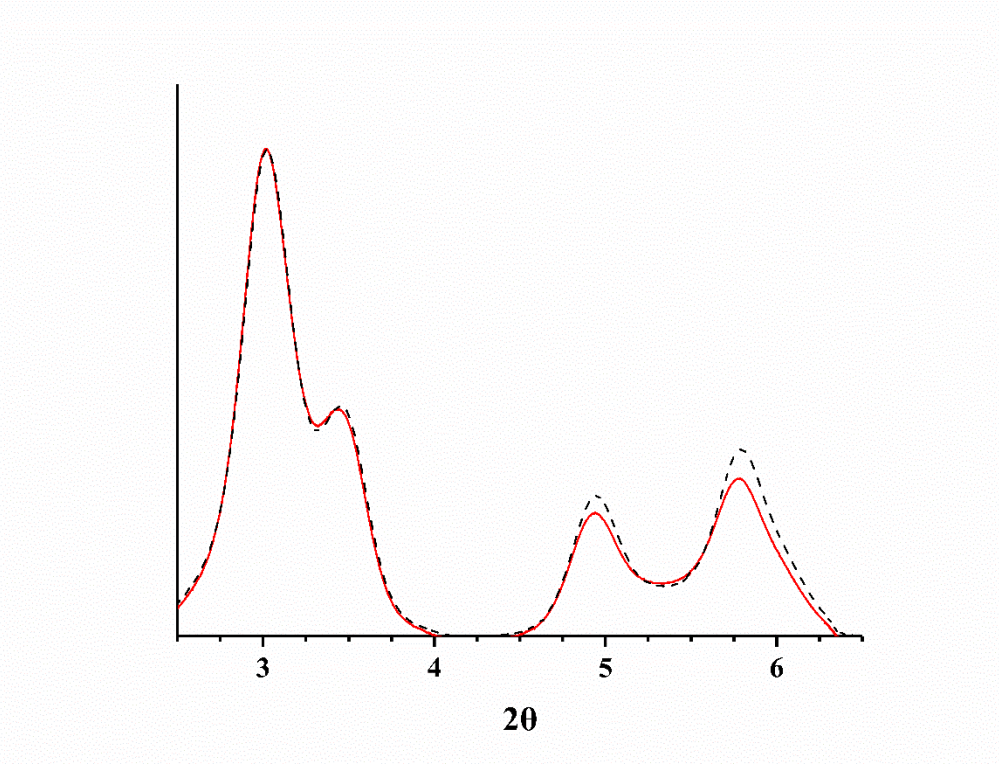

Figure C.5: Background subtracted XRD pattern of Pt-Fe(0.7) after reduction at 550 ºC. The patterns were collected at 550 ºC (solid red) and 35 ºC (dashed black).

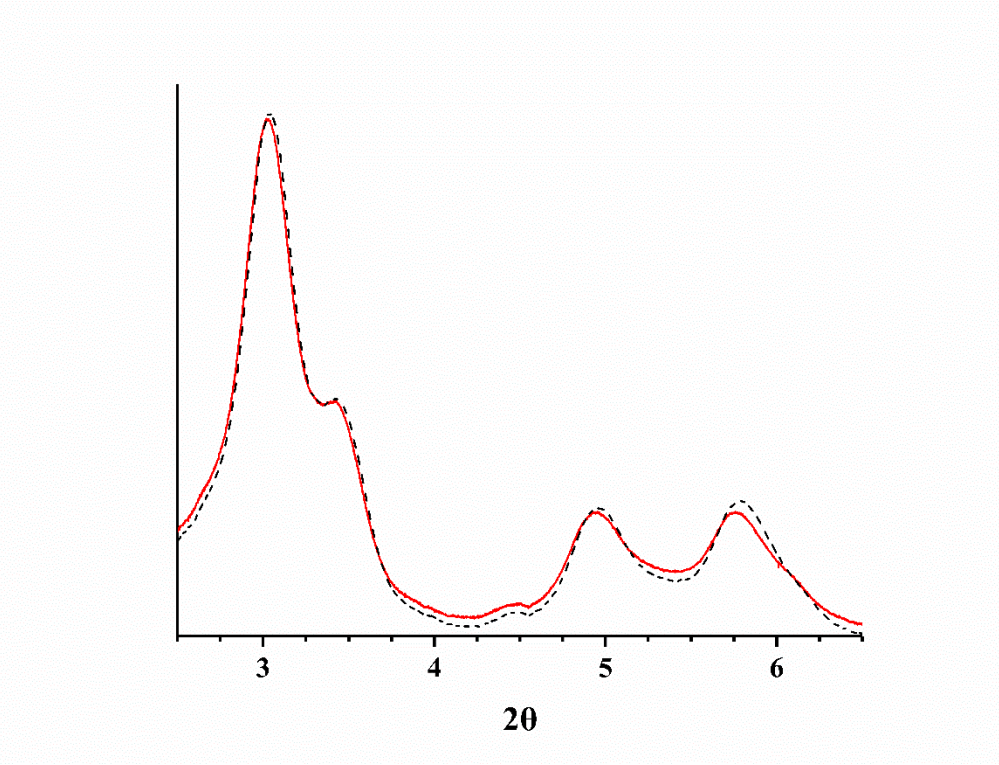

Figure C.6: Background subtracted XRD pattern of Pt-Fe(2.9) after reduction at 550 ºC. The patterns were collected at 550 ºC (solid red) and 35 ºC (dashed black).

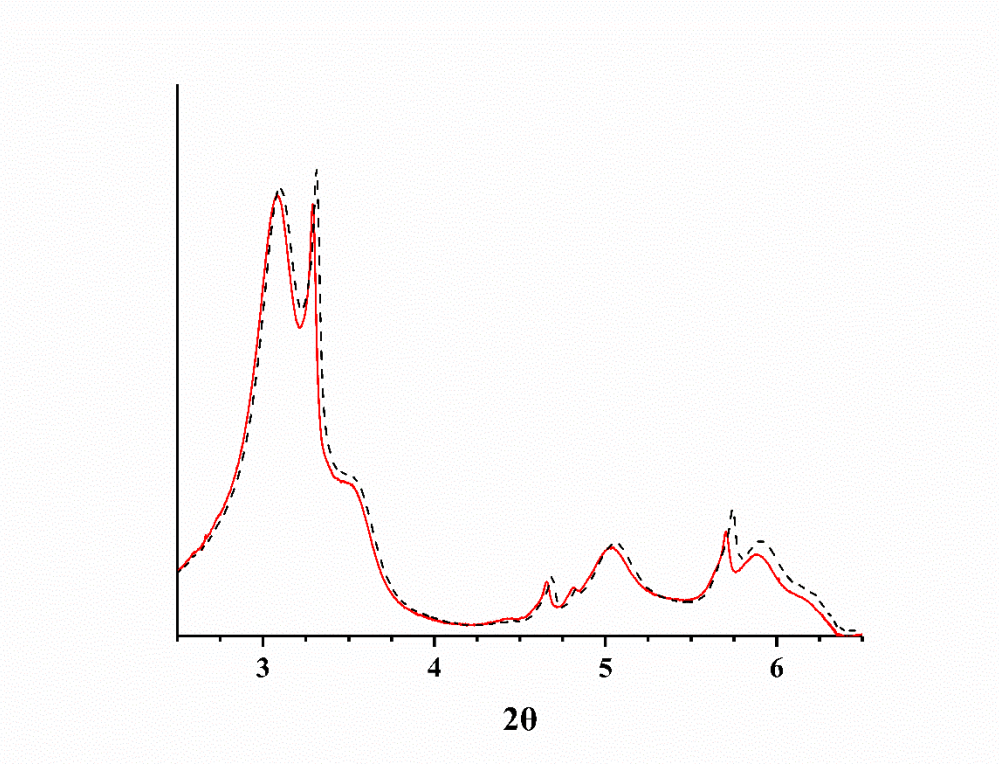

Figure C.7: Background subtracted XRD pattern of Pt-Fe(4.4) after reduction at 550 ºC. The patterns were collected at 550 ºC (solid red) and 35 ºC (dashed black).

Table C.4: Surface free energies of PtFe terminations

Sample	Slab area (m^2)	Surface free energy (J/m^2)[1]
PtFe(110)	2.91E-19	2.12
PtFe(101)	2.54E-19	1.81
PtFe(011)	2.54E-19	1.76

[1]symmetric slab construction without constraints

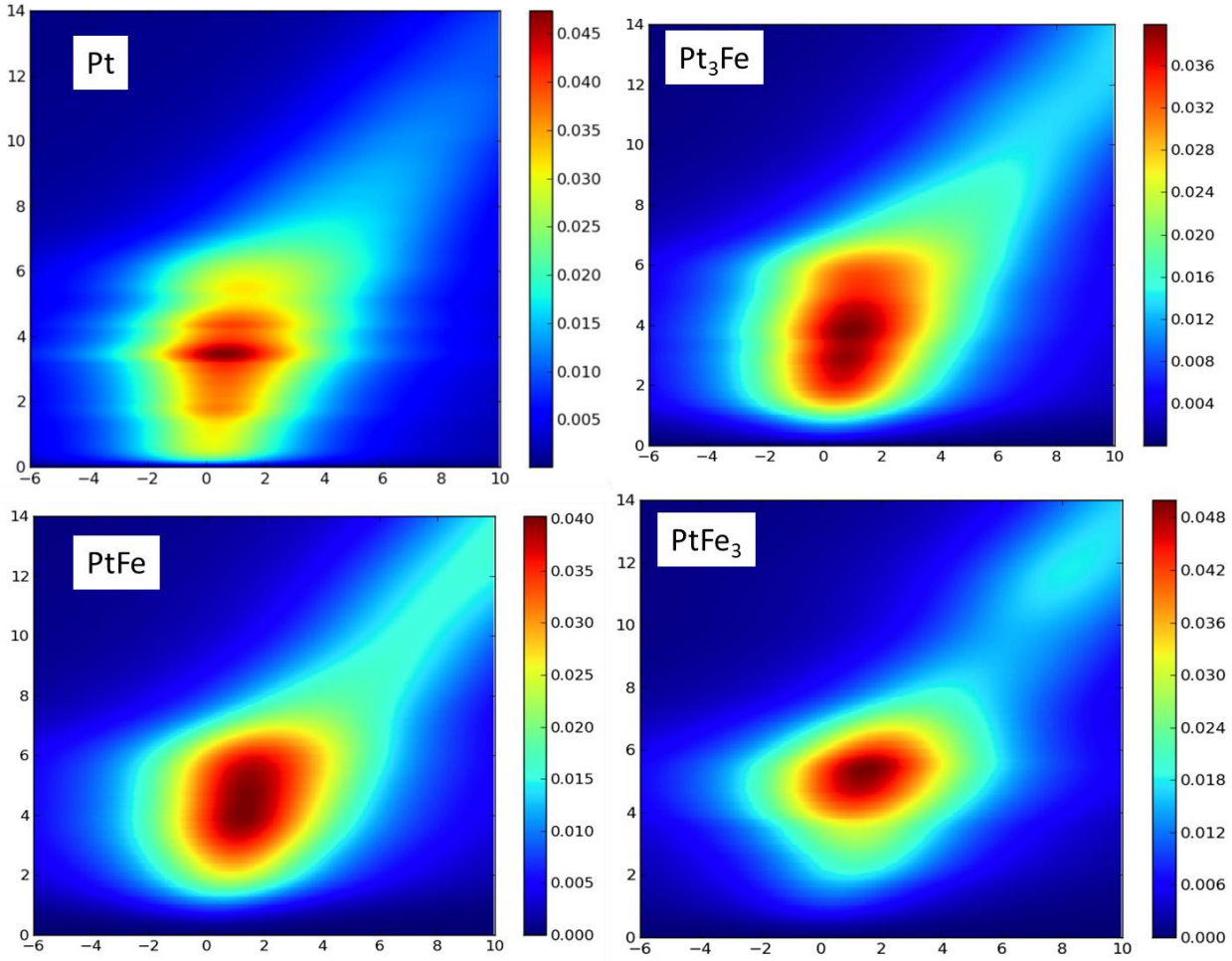

Figure C.8: DFT calculated RIXS maps of Pt (top left), Pt_3Fe (top right), PtFe (bottom left), and $PtFe_3$ (bottom right). The x-axis of each plot is the incident energy with respect to the Fermi edge of Pt in eV. The y-axis of each plot is the energy loss in eV

Table C.5: DFT calculated CO binding configurations

Sample	Adsorption site	Binding energy [eV]
Pt_3Fe	Fe top	-1.25
	Fe-Pt bridge	unstable
	Pt-Pt bridge	-1.51
	fcc	unstable
	hcp	-1.46
	Pt top	-1.58
PtFe	Pt top	-1.54
	Pt-Pt bridge	-1.49
	Pt-Fe bridge	-1.31
	Fe-Fe bridge	unstable
$PtFe_3$	Fe top	-1.69
	Fe-Fe bridge	-1.65
	Fe-Pt bridge	-1.58
	fcc	unstable
	hcp	-1.67
	Pt top	-1.48[1]

[1]Note strong binding on Fe atoms in the $PtFe_3$ alloy. Adsorption onto Fe sites resulted in a lower magnetic moment than adsorption to a Pt top site, indicating adsorption to Fe site activity may be related to spurious magnetic interactions at 0K. We report the Pt top site binding energy in the main text as it represents an adsorption site choice similar to that for other PtFe alloys and PtZn alloys reported, in addition to its magnetic moment being similar to that of other PtFe alloys.

Table C.6: Integrated d-electron counts of Pt and the three Pt-Fe IMC Structures

Sample	% difference in integrated *d* electron density[1]
Pt	0.00
Pt_3Fe	0.91
PtFe	0.93
$PtFe_3$	0.51

[1]Calculated relative to pure Pt integrated electron DOS

VITA

Evan C. Wegener received his B.S. from Michigan State University in 2014 with a major in chemical engineering and a minor in economics. During his undergraduate studies he performed research under the guidance of Professor Dennis Miller which focused on the conversion of biomass feedstocks to value added chemicals. In August of 2014 he began his graduate work at Purdue University and joined the research group of Professor Jeffrey T. Miller. His thesis work focused on the reactivity of bimetallic alkane dehydrogenation catalysts and the characterization of their geometric and electronic properties using synchrotron X-ray techniques. Upon graduation in May 2018 Evan will be joining the Chemical Sciences and Engineering Division at Argonne National Laboratory as a postdoctoral researcher.

PUBLICATIONS

Jung, D.; Saleh, L.M.A.; Berkson, Z.J.; El-Kady, M.F.; Hwang, J.Y.; Mohamed, N.; Wixtrom, A.I.; Titarenko, E.; Shao, Y.; McCarthy, K.; Guo, J.; Martini, I.B.; Kraemer, S.; Wegener, E.C.; Saint-Cricq, P.; Ruehle, B.; Langeslay, R.R.; Delferro, M.; Brosmer, J.L.; Hendon, C.H.; Gallagher-Jones, M.; Rodriguez, J.; Chapman, K.W.; Miller, J.T.; Duan, X.; Kaner, R.B.; Zink, J.I.; Chmelka, B.F.; Spokoyny, A.M.; "A molecular cross-linking approach for hybrid metal oxides," Nature Materials 2018, DOI: 10.1038/s41563-018-0021-9

Liu, K.; Zhang, C.; Yuandong, S.; Zhang, G.; Shen, X.; Zou, Feng; Zhang, H.; Wu, Z.; Wegener, E.C.; Taubert, C.; Miller, J.T.; Peng, Z.; Zhu, Y.; "High-Performance Transition Metal Phosphide Alloy Catalyst for Oxygen Evolution Reaction," ACS Nano 2018, 12, 158-167

Wegener, E.C.; Wu, Z.; Tseng, H.; Gallagher, J.R.; Ren, Y.; Diaz, R.E.; Ribeiro, F.H.; Miller, J.T.; "Structure and reactivity of Pt-In intermetallic alloy nanoparticles: highly selective catalysts for ethane dehydrogenation," Catalysis Today 2018, 299, 146-153

Murria, P.; Miskin, C.K.; Boyne, R; Cain, L.T.; Yerabolu, R.; Zhang, R.; Wegener, E.C.; Miller, J.T.; Kenttamaa, H.I.; Agrawal, R.; "Speciation of CuCl and $CuCl_2$ Thiol-Amine Solutions and Characterization of Resulting Films: Implications for Semiconductor Device Fabrication," Inorg. Chem. 2017, 56, 14396-14407

Cybulskis, V.J.; Bukowski, B.C.; Tseng, H.; Gallagher, J.R.; Wu, Z.; Wegener, E.C.; Kropf, A.J.; Ravel, B.; Ribeiro, F.H.; Greeley, J.; Miller, J.T.; "Zinc Promotion of Platinum for Catalytic Light Alkane Dehydrogenation: Insights into Geometric and Electronic Effects," ACS Catal. 2017, 7, 4173-4181

Adolph, C.M.; Werth, J.; Selvaraj, R.; Wegener, E.C.; Uyeda, C.; "Dehydrogenative Transformations of Imines Using a Heterogeneous Photocatalyst," J. Org. Chem. 2017, 82, 5959-5965

Mouat, A.R.; Lohr, T.L.; Wegener, E.C.; Miller, J.T.; Delferro, M.; Stair, P.C.; Marks, T.J.; "Reactivity of a Carbon-Supported Single-Site Molybdenum Dioxo Catalyst for Biodiesel Synthesis," ACS Catal. 2016, 6, 6762-6769

Wu, Z.; Wegener, E.C.; Tseng, H.; Gallagher, J.R.; Harris, J.W.; Diaz, R.E.; Ren, Y.; Ribeiro, F.H.; Miller, J.T.; “Pd-In intermetallic alloy nanoparticles: highly selective ethane dehydrogenation catalysts,” Catal. Sci. Technol. 2016, 6, 6965-6976